RECONFIGURABLE PASSIVE RF CIRCUITS LEVERAGING INTEGRATED FLUIDIC STRUCTURES

A Dissertation
SUBMITTED TO THE FACULTY OF
UNIVERSITY OF MINNESOTA
BY

Casey Edward Murray

IN PARTIAL FULFILLMENT OF THE REQUIREMENTS
FOR THE DEGREE OF
DOCTOR OF PHILOSOPHY

Advisor: Rhonda R. Franklin

January 2015

Acknowledgements

I would like to first thank Professor Franklin for her countless hours of mentoring throughout my graduate studies. Her guidance in systematic problem solving, meticulous record keeping, and data presentation has and will continue to have a large impact on my engineering career. I would also like to thank Prof. Gopinath, Prof. Sainati, and Prof. Stadler for their time serving as my committee members.

I would also like to thank MPACT group members: Dr. Young Seek Cho, Dr. Hosaeng Kim, Jordan Alstad, and Glenston Miranda for their support during my graduate studies. These individuals helped in my training to use laboratory equipment and were always there to hold thoughtful discussions.

Lastly, I would like to thank my family for their encouragement. My parents, Beth and Norm Murray, have been there to support and motivate me throughout my entire educational career. My wife, Clare Murray, and son, Finnegan Murray, continually provided the love and support I needed throughout this journey.

This dissertation is dedicated to my wife and son,
Clare and Finnegan Murray

Abstract

The demand for wireless capability in our everyday life is continually increasing. This demand is creating the need for multi-band systems and systems that can be changed to adapt to their environment. Many research groups are looking into ways to meet these needs. One area in particular, is incorporation of fluidics in RF design to change the circuit's characteristics by leveraging conductive, magnetic, or dielectric properties of the fluid. The work presented in this dissertation focuses on leveraging the dielectric properties of fluids and how fluids may be integrated into fundamental RF structures providing control over their characteristics. Ultimately providing design concepts that could be refined for particular applications.

Fluids are integrated into four fundamental structures in this work: 1) transmission line (Section 2), 2) directional coupler (Section 3), 3) annular slot antenna (Section 4), and 4) band-pass filter (Section 5). The transmission line work in this dissertation focuses on the use of the dielectric properties of fluids to create a tunable delay line. The directional coupler work demonstrates how fluids can be used to vary coupling and isolation in a microstrip structure. Fluids are next integrated into antenna structures demonstrating the possible tuning range. Lastly, a fluidic channel is integrated into a microstrip ring band-pass filter demonstrating the change in pass-band characteristics.

Table of Contents

List of Tables

List of Figures

1 Introduction

Interest in the use of microfluidics with RF circuitry has increased recently due to its potential to change circuit characteristics by leveraging conductive, magnetic, or dielectric properties of the fluid. The work presented in this dissertation focuses on leveraging the dielectric properties of fluids. This area of research is still being understood by the RF community and thus the following questions still need to be understood:

- What RF structures could benefit from this type of technology?
- What is the theory behind integrating fluidic structures into RF structures?
- What are some basic design guidelines for incorporating fluids into RF structures?
- Once incorporated into the structure what is the achievable range of critical characteristic(s) control?
- What are the opportunities for improvement in the current state of the technology?

To address these questions some basic RF designs with fluid channels are investigated: 1) transmission line (Section 2), 2) directional coupler (Section 3), 3) annular slot antenna (Section 4), and 4) band-pass filter (Section 5). One example of these elements integrated together is shown in Figure 1.

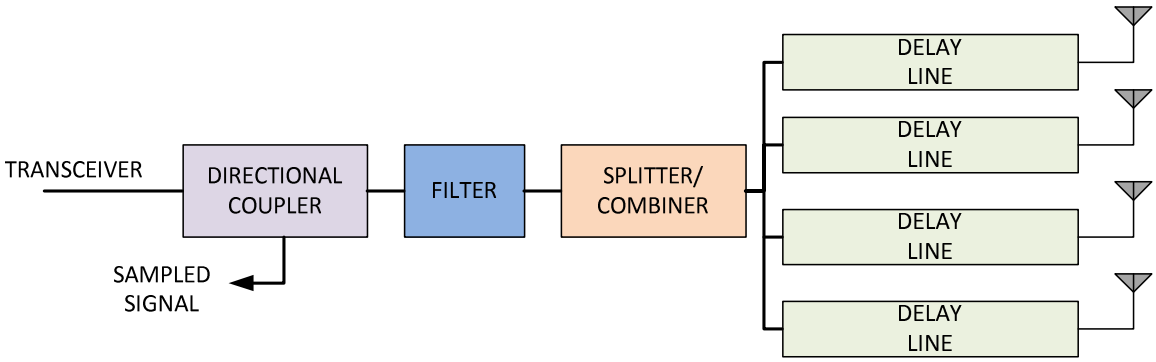

Figure 1 Example RF front-end. A directional coupler, filter, delay line, and antenna design are covered in this dissertation.

The aim of this dissertation is to aid in the advancement of the RF communities' knowledge base addressing the questions above. In this work the main fluids used are acetone and DI water. They were selected due to their ease of accessibility and that their permittivity values help demonstrate a meaningful range of dielectric values.

1.1 Thesis Overview

Section 2 details a multi-section CPW line with a fluidic channel integrated in the middle section. The tested fluids alter the effective permittivity of that section and thus change the propagation velocity. One application for this type of structure would be a controllable delay line.

The second structure, Section 3, designed is a microstrip forward wave directional coupler. The fluidic channel is attached onto the surface of the substrate in the gap between the coupled lines. The fluid is used to change the odd mode characteristics of the structure. Directivity improvement and coupling range are investigated.

Section 4 investigates the use a fluids to tune an annular slot antenna. This chapter is divided into two studies. The first is a general feasibility study illustrating the potential tuning range of the first and second resonances. The second portion of Section 4 provides a methodical design approach to achieving independent control of the first and second resonances.

Section 5 details a degenerate mode bandpass microstrip ring filter. The electrical length of a stub on the annular ring along the axis of the symmetry is varied using fluids. The amount of realizable separation of the even and odd mode frequencies is described.

Lastly in Section 6, the dissertation is summarized and recommendations of future work is detailed.

2 Coplanar Waveguide Delay Line on Borosilicate Glass

The use of fluid properties in RF circuits is gaining more interest because of the potential to create adaptive structures. A wide range of permittivity values can be realized using fluids, allowing the designer freedom to control the effective permittivity of the structure. An RF delay line structure benefits from this type of technology. One fundamental application of delay lines are in feeding networks for phased array antennas (Figure 1).

A solid state feed example using a tapered dielectric overlay on a multi-port power divider structure is presented in [1]. The dielectric overlay starts at the same location on all the divided microstrip lines then tapers on the output edge; creating a progressive phase shift across the output ports. The dielectric overlay allows the structure to be smaller in the planar dimension because to create this same phase shift using only the transmission lines would require long transmission lines. This example has the disadvantage of being in a fixed state. Fluids could be used to provide the system with more configuration options. However, the RF community first needs to understand how fluid structures could be integrated into transmission lines structures and what the achievable phase shift is.

In theoretical paper [2], fluidic channels are integrated into the substrate underneath a microstrip topology. Simulation results show that a difference can be observed in the propagation delay between air filled as compared to acetone filled fluidic channels. The theoretical predicated delay difference is 1.4 ps/mm.

Phase delay potential in coplanar waveguide (CPW) structures using periodic fluidic channel/reservoir placement is investigated in [3-4]. Through simulation, [3] compares the phase delay of fluidic reservoirs directly underneath the signal line in a conductor backed CPW to the phase delay when the reservoirs are in one or both of the signal-ground gaps of the CPW. The maximum phase delay was realized when the fluidic reservoirs in the substrate where placed in both signal-ground gaps of a CPW. Rather than integrating the periodic fluidic reservoirs into the substrate, the design in [4] integrates a periodic fluidic channel structure onto a CPW surface. The channels are perpendicular to the signal line; thus the signal will travel through the fluidic housing material in between each of the channels.

The research detailed in this chapter investigates the achievable phase delay when fluidic channels are run parallel to the CPW signal line rather than perpendicular (Figure 2) [5]. Additionally, rather than embedding a channel in the substrate, etching channels into the surface of signal-ground spacing is characterized. CPW was selected since all the conductors reside on the same surface of the wafer. As a planar architecture, the housing required to contain the fluid can be mounted on the top surface of the substrate. A popular material used in microfluidic applications is a polymer called polydimethylsiloxane (PDMS). In this work, the design and effects of the dielectric housing is investigated to understand the effects the housing material, shape and size may play on the effective dielectric seen by the CPW line, and hence the propagation delay. Simulation and measurement data is presented for air or de-ionized water (DI) fluids in the polymer housing shape related to cavity width and height. Also, two different

substrate material (glass and duroid) designs are described, showing the flexibility to transport and scale the basic principles presented in different substrate environments.

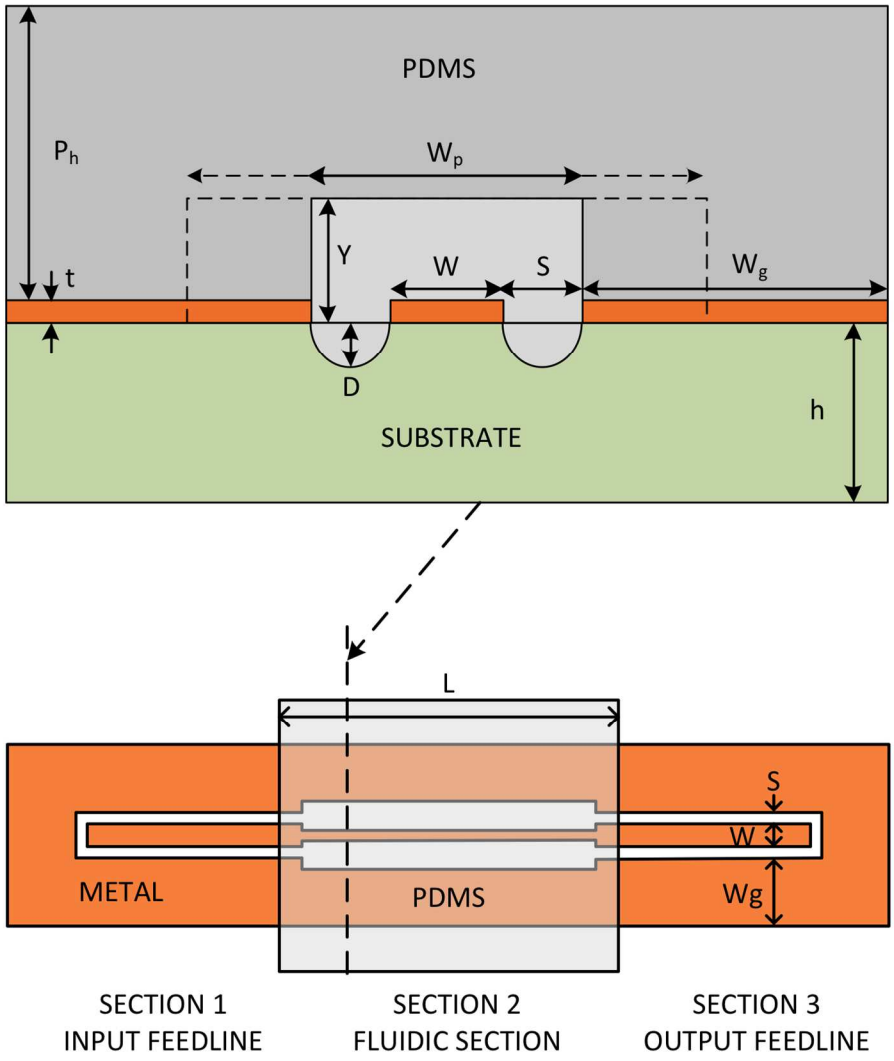

Figure 2 Coplanar waveguide with fluidic housing. Top image is cross-section of fluidic region.

2.1 Development

The effective permittivity in a design impacts signal velocity and impedance. Propagation velocity is inversely proportional to the square root of the effective permittivity as shown in Eq. 2.1.

$$v_p = \frac{c}{\sqrt{\varepsilon_{eff}}} \tag{2.1}$$

By controlling the effective permittivity of the CPW, the propagation velocity can be altered, which determines the phase.

Characteristic impedance is also altered when the effective permittivity is changed. In a low loss structure, characteristic impedance is inversely proportional to the square root of the capacitance per unit length (Eq. 2.2).

$$Z_o = \sqrt{\frac{L'}{C'}} \tag{2.2}$$

Thus, as effective permittivity is increased, the characteristic impedance of the CPW will decrease. To maintain an acceptable return loss value when high permittivity fluids are inserted into the polymer housing, the characteristic impedance is designed to be slightly higher than 50 ohms when air is present in the housing, since it will reduce once the high permittivity fluid is inserted. Designing for this requires some knowledge of the range of fluid permittivity that may be introduced into the fluidic channel.

2.2 Design

The designs investigated have the same basic architecture as shown in Figure 2 and consist of three CPW sections: input feedline, fluidic section, and output feedline. The input and output feedlines are 50 Ω transmission lines providing a place to probe the structure. The fluidic section will vary in impedance depending on the fluid present in the channels and cavity. The fluid is contained in the PDMS housing, forming a cavity over a portion of the CPW line and channel region shown in Figure 2 (fluidic section).

In CPW the electric field resides predominately in the gap (S) spacing. To develop an understanding of the realizable range of effective permittivity values using different fluids, cavity width (W_P), cavity height, and channel depth parameters are simulated using Q3D [6]. The impact of these parameters on characteristic impedance and effective permittivity are summarized in Table 1. The base substrate is glass (ε_r=4.6) and the channel/cavity is filled with either DI water (ε_r=81) or air (ε_r=1).

Table 1 Simulated effective permittivity and characteristic impedance summary of design parameter combinations.

Design #	Cavity Height (µm)	Cavity Width (µm)	Channel Depth (µm)	ε_{eff} with air	Z_o (Ω) with air	ε_{eff} with DI water	Z_o (Ω) with DI water
1	32	752	32	3.1	82.0	12.1	41.3
2	32	752	0	3.2	80.0	9.9	45.5
3	32	8000	32	3.1	82.4	13.2	39.6
4	32	8000	0	3.2	80.4	10.5	44.3
5	150	752	32	2.7	87.1	19.1	32.7
6	150	752	0	2.9	84.7	18.5	33.4
7	150	8000	32	2.7	88.0	27.9	27.2
8	150	8000	0	2.8	85.5	26.6	28.0

Two cavity width dimensions are investigated. The first width, W_p= 752 μm, is equal to 2S+W (design 1, 2, 5, and 6). The second width is chosen to be much wider (W_p=8000 μm) to allow more of the electric field to interact with the fluid housed in the cavity (design 3, 4, 7 and 8). In addition to the two cavity width dimensions investigated, two cavity heights (Y=32 μm and Y=150 μm) are also simulated. Lastly, a channel depth (D) of 32 μm is compared to a CPW design with no channel to determine how significant its contribution is to phase delay and to determine if the fabrication process could be simplified. In Table 1, odd number designs have channels of 32 μm and even number designs have no channels.

Figure 3 shows the change in characteristic impedance for increasing the channel width from W_p= 752 μm to W_p=8000 μm. A positive value indicates the characteristic impedance increased while a negative value indicates a decrease in characteristic impedance. The change in characteristic impedance when air is present in the cavity and channels is minimal, less than 1 ohm. When DI water is used, the change in characteristic impedance due to increasing the channel width is increased the most (5.5 ohms) when the cavity height is 150 μm.

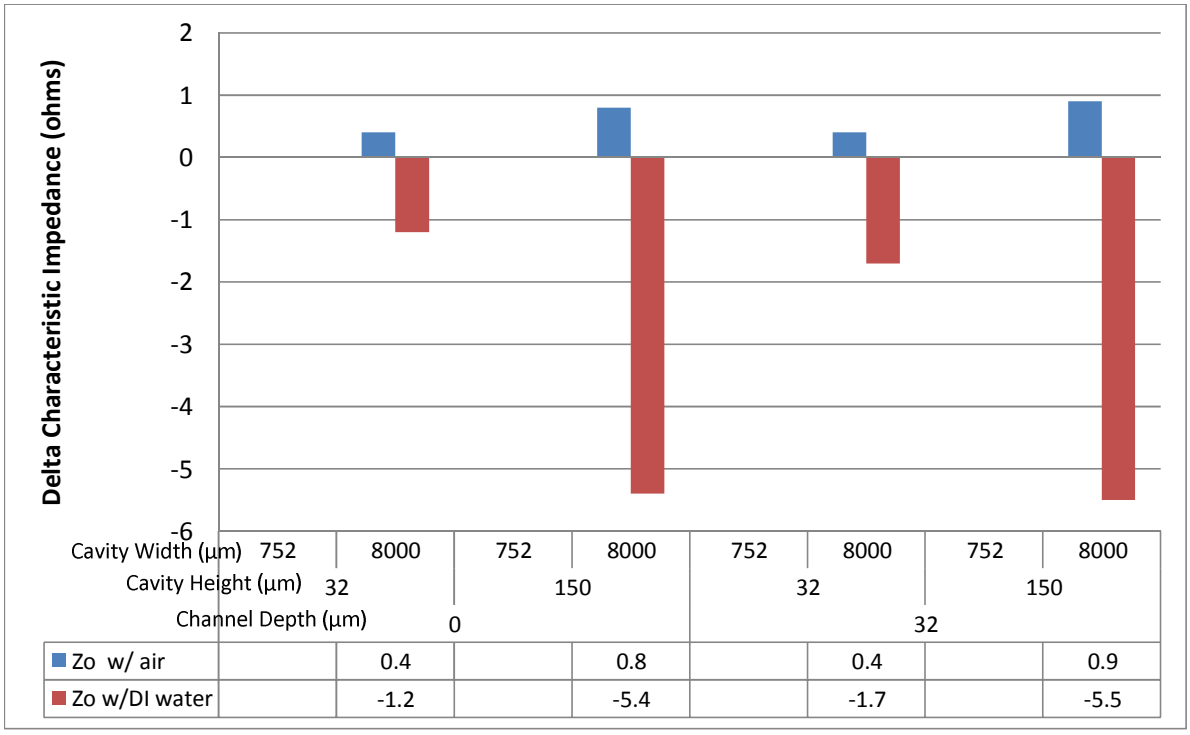

Figure 3 Change in characteristic impedance when cavity width is increased from 752 µm to 8000 µm. Cavity is filled with either air or DI water.

The next parameter simulated was the cavity height (Y). Based on the simulation results, a significant increase in the characteristic impedance range for the cavity/channels filled with air to the cavity/channels filled with DI water could be realized using Y=150 µm rather than Y=32 µm.

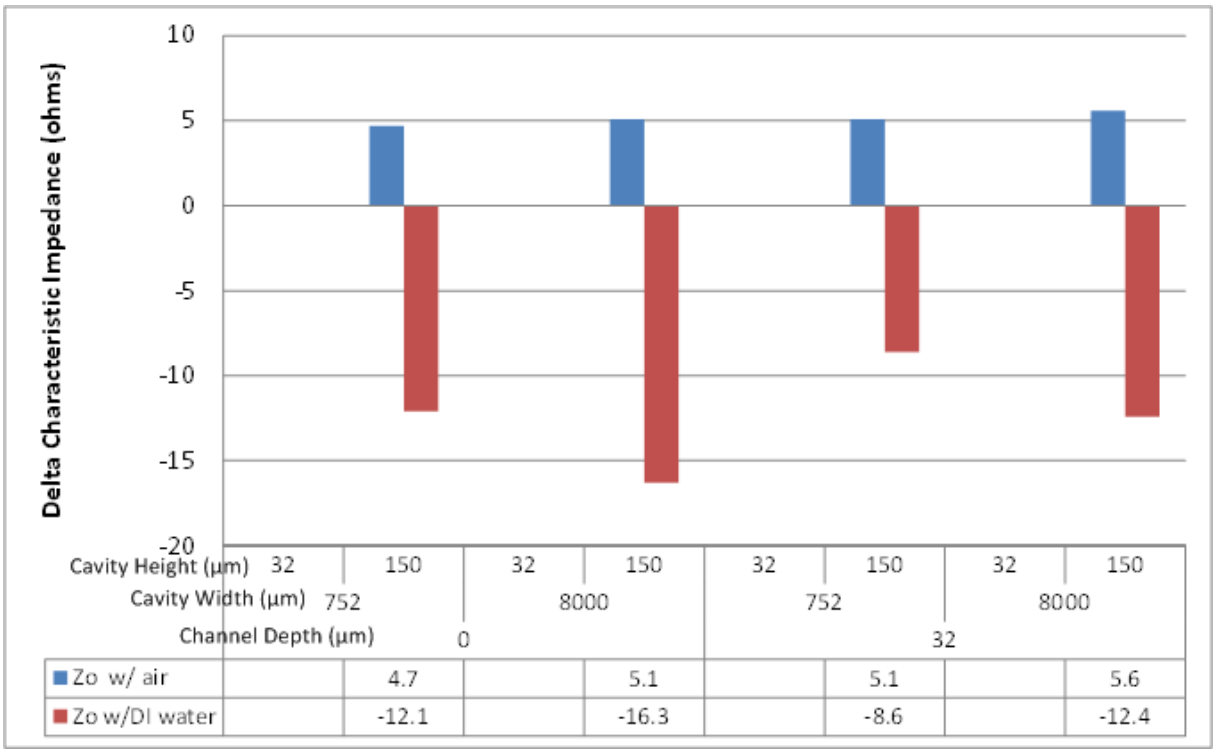

Figure 4 Change in characteristic impedance when cavity height is changed from 32 µm to 150 µm. Cavity is filled with either air or DI water.

The third parameter investigated through simulation was channel depth. Figure 5 indicates there is little benefit to including channels when the cavity height (Y) is 150 µm. There is some benefit to the channels, approximately 4-5 ohms, when the cavity height is reduced to 32 µm.

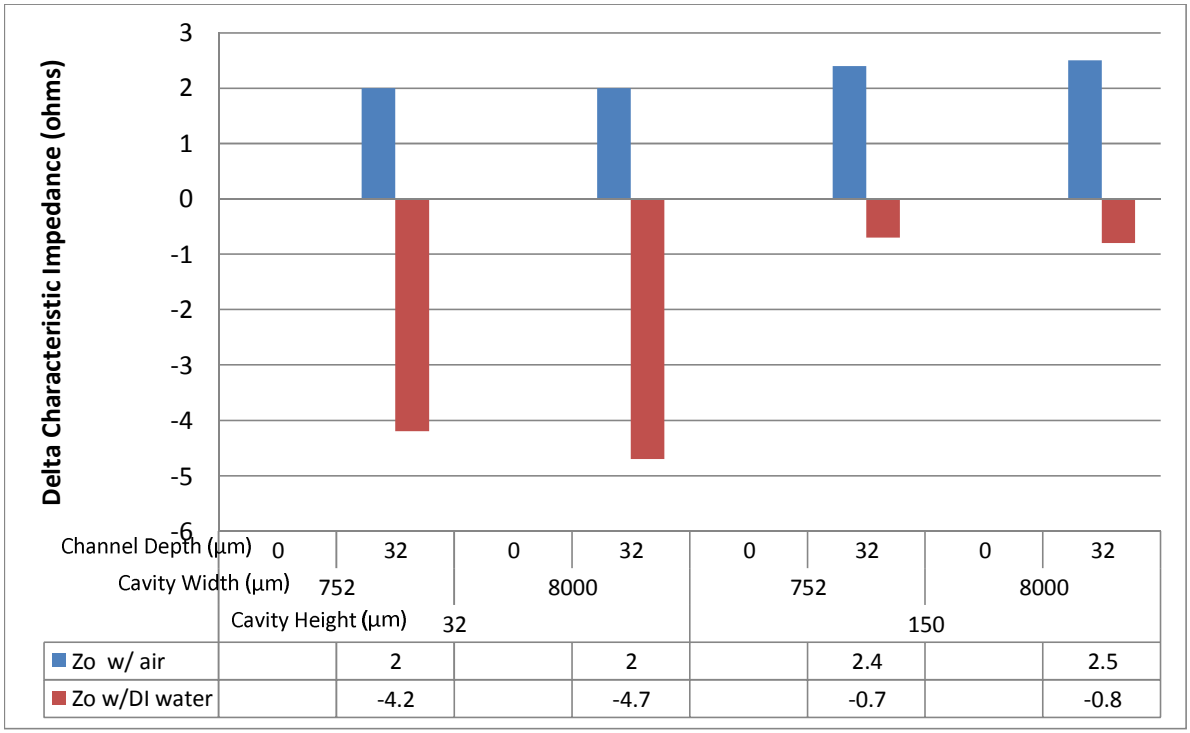

Figure 5 Change in characteristic impedance due to channels in substrate. Channels are located in ground-signal gaps of CPW.

Based on simulation, the largest difference in characteristic impedance/effective permittivity (Table 2) observed between the air and DI water filled housing is when the cavity is tallest (150 µm) and widest (8000 µm). Comparing design 7 and 8, the etched channels, under these conditions, provide little additional tuning range.

Table 2 Characteristic impedance summary of various cavity dimensions and channel depths.

Cavity Height (µm)	Cavity Width (µm)	Channel Depth (µm)	Z_o (Ω) w/air	Z_o (Ω) w/DI water	Delta (Ω)
32	752	0	80	45.5	34.5
		32	82	41.3	40.7
	8000	0	80.4	44.3	36.1
		32	82.4	39.6	42.8
150	752	0	84.7	33.4	51.3
		32	87.1	32.7	54.4
	8000	0	85.5	28	57.5
		32	88	27.2	60.8

Based on the simulation results, two circuits (design 1 and 8) are fabricated. Circuit 1, based on design 1, has a base substrate material of glass and the dimensions for the housing and CPW circuit are given in Table 3. Circuit 2, based on design 8, has a base substrate material of duroid and the dimensions are outlined in Table 3. These dimensions are a scaled version of glass design 8. SMA connectors with a distance of 400 μm between the signal and ground conductors are used to measure Circuit 2. This distance defines the gap spacing of the CPW feedline. This feedline on duroid, and the dimensional ratio of the feedline to fluidic region in glass design 8, defines the fluidic region by maintaining a similar ratio.

Table 3 Substrate parameters and design dimensions

Parameter	Glass Substrate	Duroid Substrate
ε_r	4.6	6.15
tanδ	0.0037	0.002
t	3 um	17.78 um
h	500 um	1270 um
Fluidic Region		
W	260 um	1497 um
S	246 um	1818 um
W_g	2324 um	30460 um
l	8063 um	7950 um
D	32 um	0 um
Feedlines		
W	394 um	2279 um
S	54 um	400 um
Wg	2449 um	31496 um
l	9152 um	8500 um

2.3 Fabrication

As stated in Section 2.2 two designs were fabricated, one on a glass substrate (Circuit 1) and one on Rogers duroid (Circuit 2).

2.3.1 Circuit 1 Glass Substrate

Circuit 1 is formed on a 500 μm thick Borofloat33 borosilicate glass wafer (ε_r= 4.6 and loss tangent of 37×10^{-4} at 1 MHz) [7]. Cr/Au/PR (60 nm/400 nm/10 um) [8] is used as a mask when 32 μm channels are etched into glass using 49% HF. The masking layers are removed and replaced with an e-beam evaporated metal Cr/Au/Cr (300/1500/300 Å) seed layer. The CPW circuit is patterned using SPR 220-7 positive photoresist and electroplated to a thickness of 3 μm after removing the top Cr mask layer.

The polymer housing is made of polydimethylsiloxane (PDMS) (Sylgard 182 Silicone Elastomer 10:1 ratio) and is formed using a silicon master mold. The individual PDMS die is bonded to the glass wafer in the DUT region using standard PDMS/glass bonding procedures. The PDMS die is also sealed around the edges with adhesive (Dow Corning SE 9187 L). To inject the fluids, teflon tubing with an inner diameter of 558.8 μm is inserted into the PDMS lid (Figure 6).

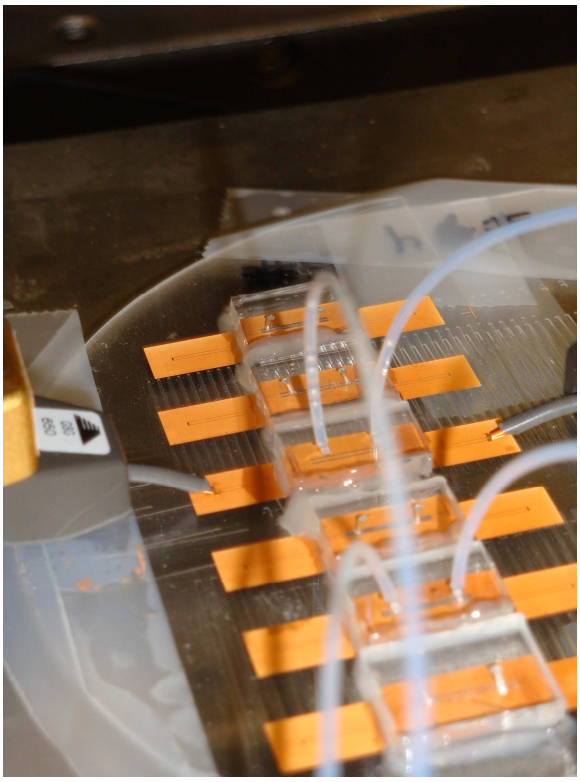

Figure 6 Fabricated test structures on glass substrate

2.3.2 Circuit 2 on Duroid Substrate

Relative to Circuit 1, Circuit 2 fabrication process is greatly simplified. Circuit 2 is fabricated on a 50 mil (1270 um) thick Rogers duroid RO3006 (ε_r= 6.15, tanδ=0.002) substrate with ½ oz. copper thickness. An LPKF milling machine is used to mill the CPW circuit. Similar to Circuit 1, a PDMS housing is attached to the surface over the fluidic region, using adhesive.

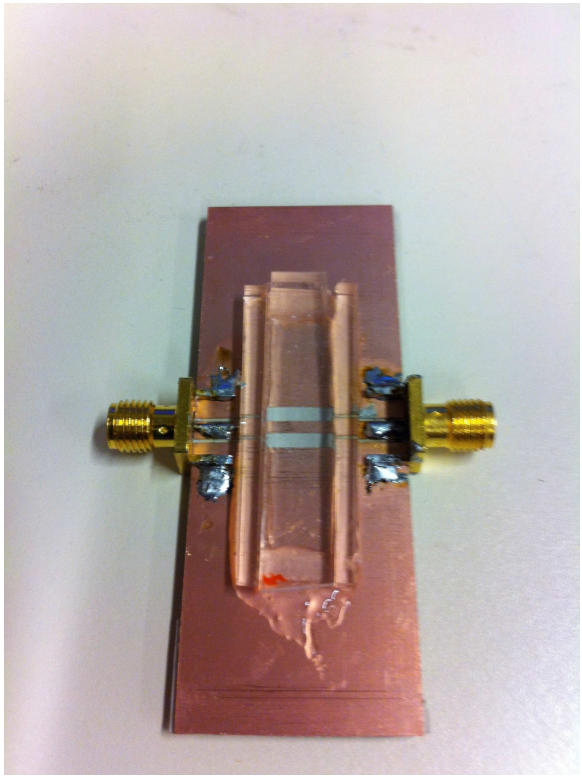

Figure 7 Fabricated structure on Duroid substrate

2.4 Calibration and Measurement

An HP810C network analyzer (45 MHz - 50 GHz), Cascade Microtech probe station, and Cascade Microtech 650 µm pitch GSG probes are used to perform measurements on Circuit 1. Line-Reflect-Match (LRM) calibration is performed with a 250-1250 µm LRM calibration chip.

Circuit 2 uses SMA connectors on the input and output ports. S-parameter measurements are performed using an Anritsu VNA.

2.5 Characterization

Simulation and measurement return loss data for air in the channels and cavity is shown in Figure 8. Simulation data was obtained using HFSS [9]. Simulation and measurement data show good agreement for both Circuit 1 and Circuit 2. Both circuits have a return loss better than 10 dB up to 2 GHz.

Circuit 1 return loss measurement and simulation data for DI water in the channel and cavity is shown in Figure 8. The maximum simulated return loss is -15.2 dB, while the maximum measured return loss is -4.5 dB. The DI water pressure was suspected to have caused the lid to lift slightly, resulting in the discrepancy between simulation and measurement. Using a cavity height estimate of 150 μm and width of 8000 μm to emulate the raised cavity, good correlation with return loss measurements is obtained in simulations (Figure 8). Circuit 2 is designed to be a scaled version of Circuit 1 with the modified dimensions of the pressurized cavity (higher and wider fluidic channel) and exhibits a similar trend with exception of the resonance at 2 GHz (Figure 8). In Circuit 1 the resonance is caused by water under the PDMS overlap region of the feedlines in Circuit 1. The water, a high permittivity fluid, decreases the characteristic impedance from its air state. Thus the 50 ohm feedlines are greatly reduced in impedance. Circuit 2 was securely adhered to the substrate to not allow fluid in the same overlap region. It does not exhibit the resonance.

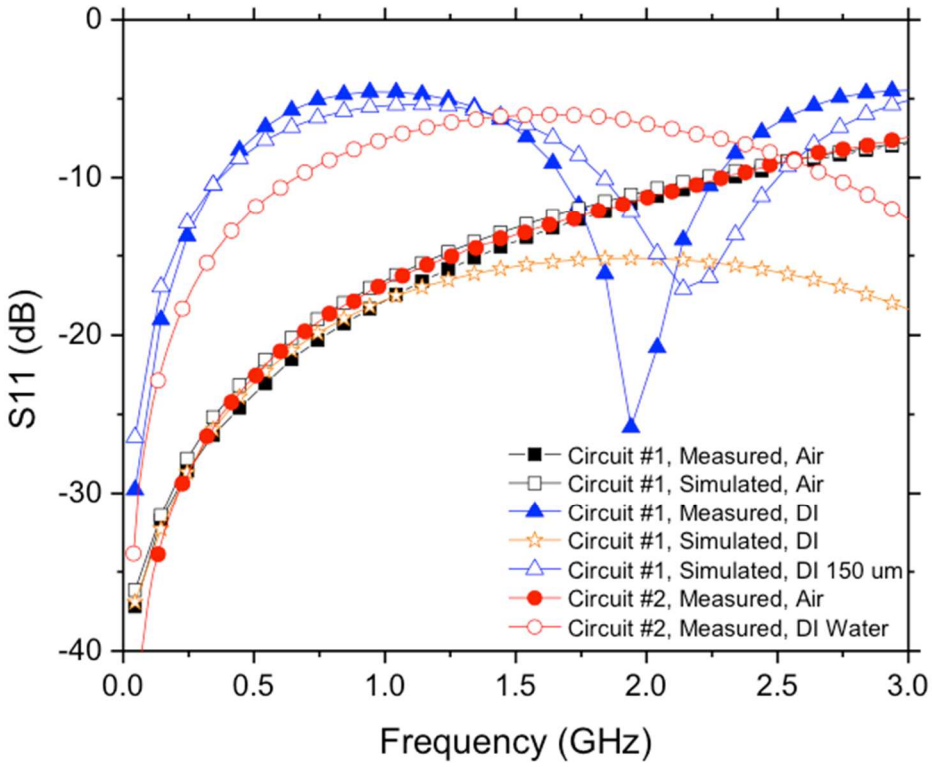

Figure 8 Return loss of circuit 1 and 2 when filled with either air or DI water

Insertion loss measurement and simulation results are shown in Figure 9. Measurement and simulation insertion loss data for air in both circuits are in good agreement. In the air case, the insertion loss is less than 1 dB over the UHF band. However, DI water, has much more loss, -1.75 dB at 1.84 GHz and -3 dB at 2.24 GHz for the entire circuit. This includes two feedlines and the fluidic region.

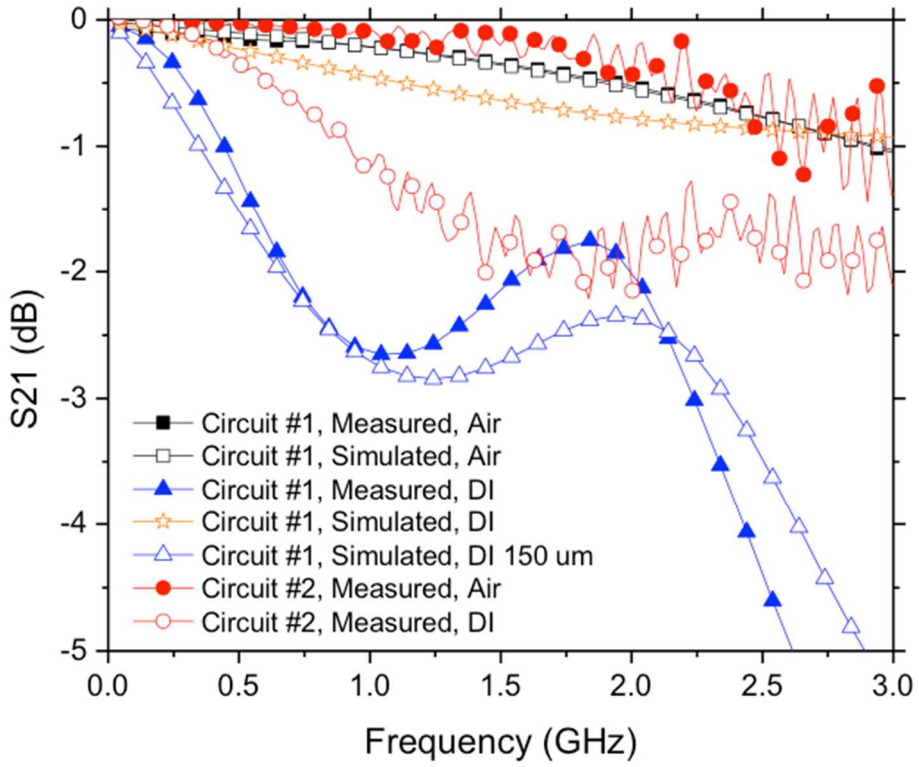

Figure 9 Insertion loss of circuit 1 and 2 with either air or DI water in housing

Since measurement is similar to simulation when the water pressure is factored into simulation, Circuit 1 feedline loss is determined using simulation [9]. Next, measured S-parameter data for the entire circuit shown in Figure 2 is used to estimate the loss of the fluidic region (including PDMS overlap regions) filled with DI water using the method outlined in [10]. The estimated result is a loss of 0.28 dB/mm at 2.24 GHz.

The insertion loss phase is shown in Figure 10. At 1.84 GHz, the phase of the entire circuit, feedlines and fluidic section, is 99 degrees with air in the housing. Inserting DI water into the housing of Circuit 1 yields an additional 94 degrees of phase shift at 1.84 GHz. The relative phase shift converted to a per unit length value for the

fluidic section (including PDMS overlap, L=10,064 μm) is approximately 9.4 degrees/mm for DI water.

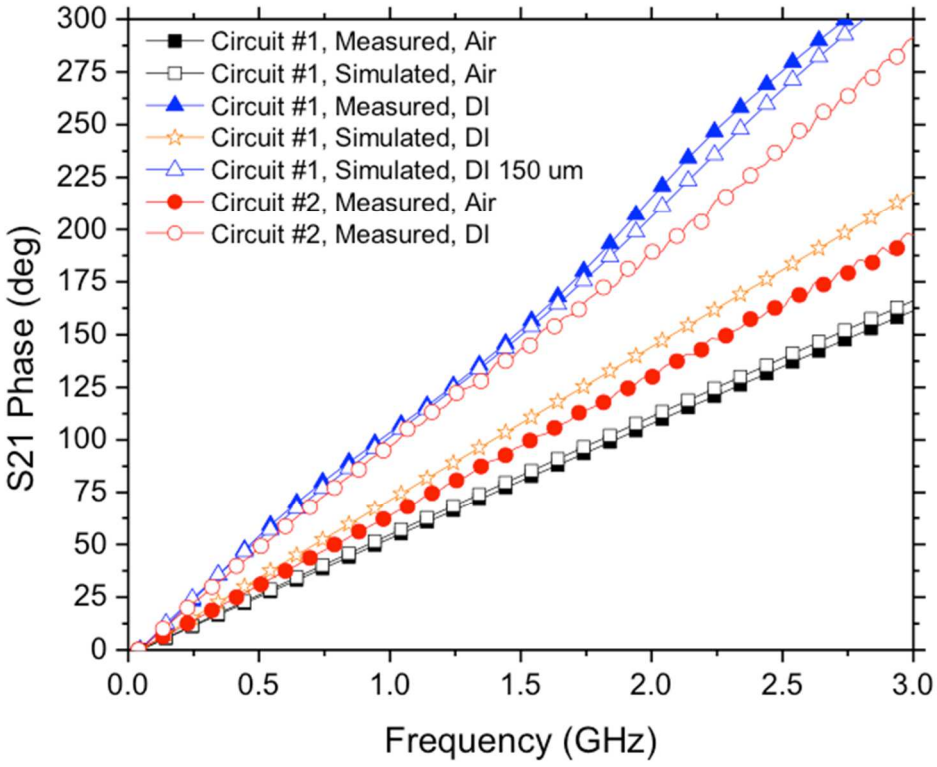

Figure 10 Phase delay of circuit 1 and 2 when the fluidic housing is filled with either DI water or air.

2.6 Conclusion

Measurement and simulation results for a coplanar waveguide architecture with fluidics integrated onto the surface is presented. A variable delay is realized by injecting DI water into the cavity and channels. The higher permittivity fluid, DI water, exhibits a large phase shift of approximately 9.4 degrees/mm. However, transmission power is

compromised due to high absorption in DI water. Using smaller fluidic housing dimensions can decrease insertion loss but reduces the tunable range of phase.

To create a phased array system (Figure 1) using fluids, either multiple fluidic channels or a single channel solution can be used. The multiple channel fixed channel dimension solution could be realized using different fluids (different permittivity) to achieve the different required phase delays. Otherwise a single fluid and increasing channel dimensions could be used to achieve the required phase delays. A single channel solution could be realized using dimensions small enough that fluids could be alternated yet remain unmixed.

3 Edge Coupled Microstrip Directional Coupler

A directional coupler is used to sample a signal (Figure 1). One application for such a device is when two systems are in close proximity and higher isolation is needed. The noise signal (nearby transmitter) is sampled and signal processing is applied to improve receive sensitivity.

Conventional edge coupled microstrip directional couplers have loose coupling and poor directivity. This quasi-TEM type of transmission line has unequal even and odd mode effective permittivities resulting in uneven propagation constants. The difference in propagation constant will cause power to couple in the forward direction, which is undesirable for a backward wave design. To the authors knowledge, the three primary ways to equalize the propagation velocities and thus improve directivity are: (1) capacitive compensation [11-13], (2) slow-wave techniques on the inner edges of the coupled section [14-16], and (3) dielectric overlay [17].

The design discussed in this chapter leverages these same equalization principles by integrating a microfluidic superstrate in the coupling gap of the directional coupler [18]. In the microfluidic channel, relative dielectric constant values ranging from ε_r=81 to ε_r=1, deionized water and air are studied, respectively.

In addition to improving directivity by using capacitive compensation, variable capacitance between the coupled conductors [19] has been shown to provide the capability to vary coupling. Thus, the tunable range of coupling was evaluated

experimentally and compared to its full-wave simulation, over a large relative dielectric constant range (1-81).

In this work deionized water is used for the high permittivity (ε_r= 81) fluid and air is used for the low permittivity. However, an undesirable aspect of DI-water is its high loss (tan $\delta \cong 0.15$ at 3 GHz [20]), associated with loss tangent values that are several orders of magnitude higher than preferred for most high frequency RF circuits. Also discussed in this chapter, is a method that minimizes the impact of loss while leveraging the benefits of the high relative dielectric constant value to the design.

3.1 Theory

A directional coupler is a four port structure as shown in Figure 11 used to couple a specified amount of power to a given port. There are two primary types of directional couplers: backward wave (Figure 11a) and forward wave (Figure 11b) couplers [17]. Both of these couplers are analyzed using even/odd mode analysis.

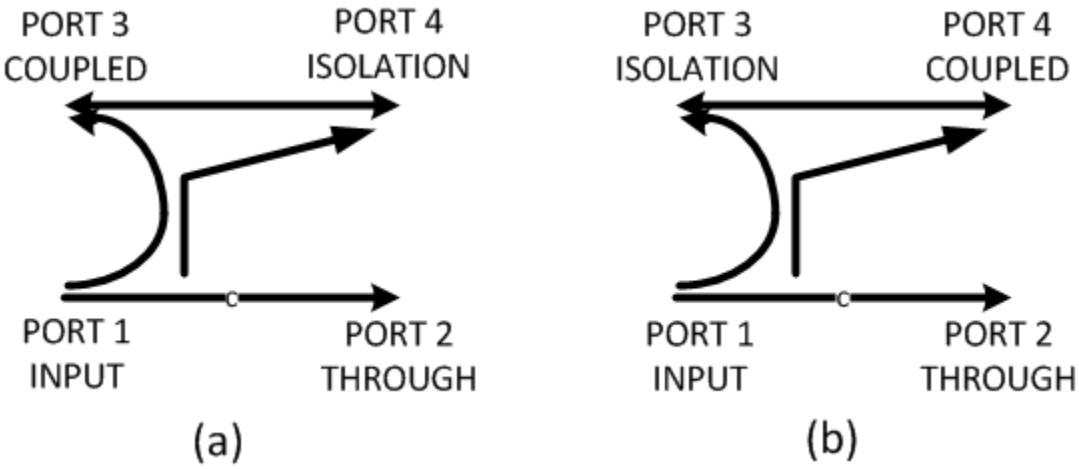

Figure 11 Port definitions for (a) backward wave directional couplers and (b) forward wave directional couplers

In terms of forward wave coupler (Figure 11b) s-parameters, coupling is S_{41} and isolation is S_{31}. The desired coupling at a given frequency is given by Eq. 3.1 and is dictated by the difference of square roots for the even and odd mode effective dielectric constants [17].

$$|S_{41}| = \left|\sin\left(\frac{\pi\left(\sqrt{\varepsilon_{ree}}-\sqrt{\varepsilon_{reo}}\right)L}{c} f\right)\right| \tag{3.1}$$

Complete power transfer to the forward port occurs when length of the coupled section is inversely proportional to the difference in even and odd mode propagation constants (Eq. 3.2).

$$l = \frac{\pi}{|\beta_e - \beta_o|} \tag{3.2}$$

Backward wave couplers couple power to port 3 as shown in Figure 11a. Maximum coupling occurs when the coupled section length of transmission line is equal to a quarter wavelength (guided). The isolation port is port 4. Design equations exist in

[17] and a subset are repeated here for reference. Eq. 3.3 relates the desired coupling (C) to voltage coupling coefficient (k).

$$k = 10^{-C/20} \tag{3.3}$$

Once the voltage coupling coefficient and desired characteristic impedance is known, then the even mode characteristic impedance (Z_{oe}) and the odd mode characteristic impedance (Z_{oo}) can be determined by Eq. 3.4 and Eq. 3.5.

$$Z_{oe} = Z_o\sqrt{\frac{1+k}{1-k}} \tag{3.4}$$

$$Z_{oo} = Z_o\sqrt{\frac{1-k}{1+k}} \tag{3.5}$$

Alternatively, the characteristic impedance of the coupled lines is related to the even and odd mode characteristic impedances by Eq. 3.6.

$$Z_o = \sqrt{Z_{oo}Z_{oe}} \tag{3.6}$$

3.2 Development

Two backward wave directional coupler circuits, designed for 2.4 GHz operation, are investigated in this work. Both of these designs have the same fundamental design with only a single slight difference, which will be discussed in more detail later in this chapter. The coupling level is design to be approximately 14 dB coupling for the baseline design. Based on the coupling (14 dB), characteristic impedance (50 ohms), frequency of operation (2.4 GHz) and electrical length (90 degrees) the trace widths, separation, and length where determined using Agilent LineCalc.

In order to incorporate the fluidic channel, which will be described later, and SMA connectors to probe the structure, microstrip lines are tapered outward from the centerline of the structure to the connectors. A top view of the coupler design is shown in Figure 12.

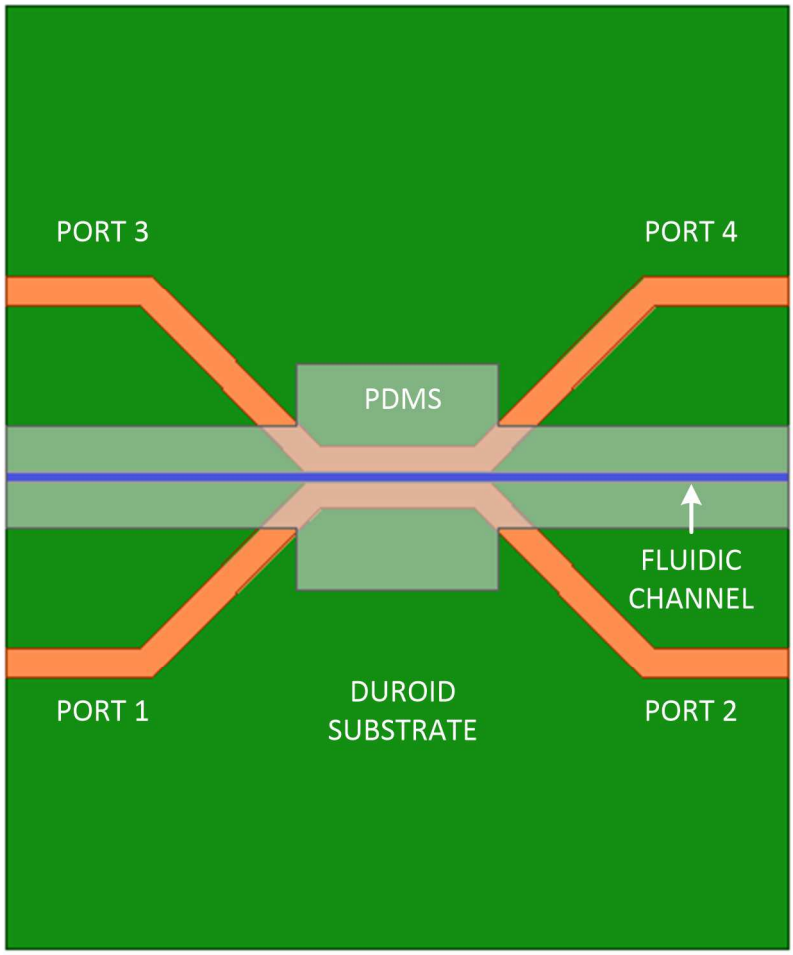

Figure 12 Top view of microstrip directional coupler with fluidic channel in gap spacing. The dashed line represents the cross-section view shown in Figure 13

As stated in the introduction of this chapter, microstrip directional couplers have degraded isolation/directivity due to unequal even and odd mode propagation velocities. Two of the techniques used to reduce the difference are capacitive compensation and dielectric loading (overlay). These principles are incorporated into these designs by integrating a cavity onto the surface of the coupler creating a fluidic channel. The channel width is equal to the gap spacing between the coupled lines, where the intent of the channel is to house the fluid that impacts odd mode propagation. In addition to impacting the odd mode, there is a slight impact on even mode characteristics due to microstrip fringing electric field. The design shown in Figure 12 is used to evaluate the effects of capacitance between and above the metal electrodes created by fluid on coupler characteristics.

Two designs are described in this chapter. The difference in the two designs is the channel interface to the surface of the substrate. In the first design the fluid can come in direct contact with substrate surface (X=0 mm) as shown in the cross-section view (Figure 13). In this channel topology, the injected fluid has maximum impact to the odd mode propagation without requiring more advanced substrate fabrication methods.

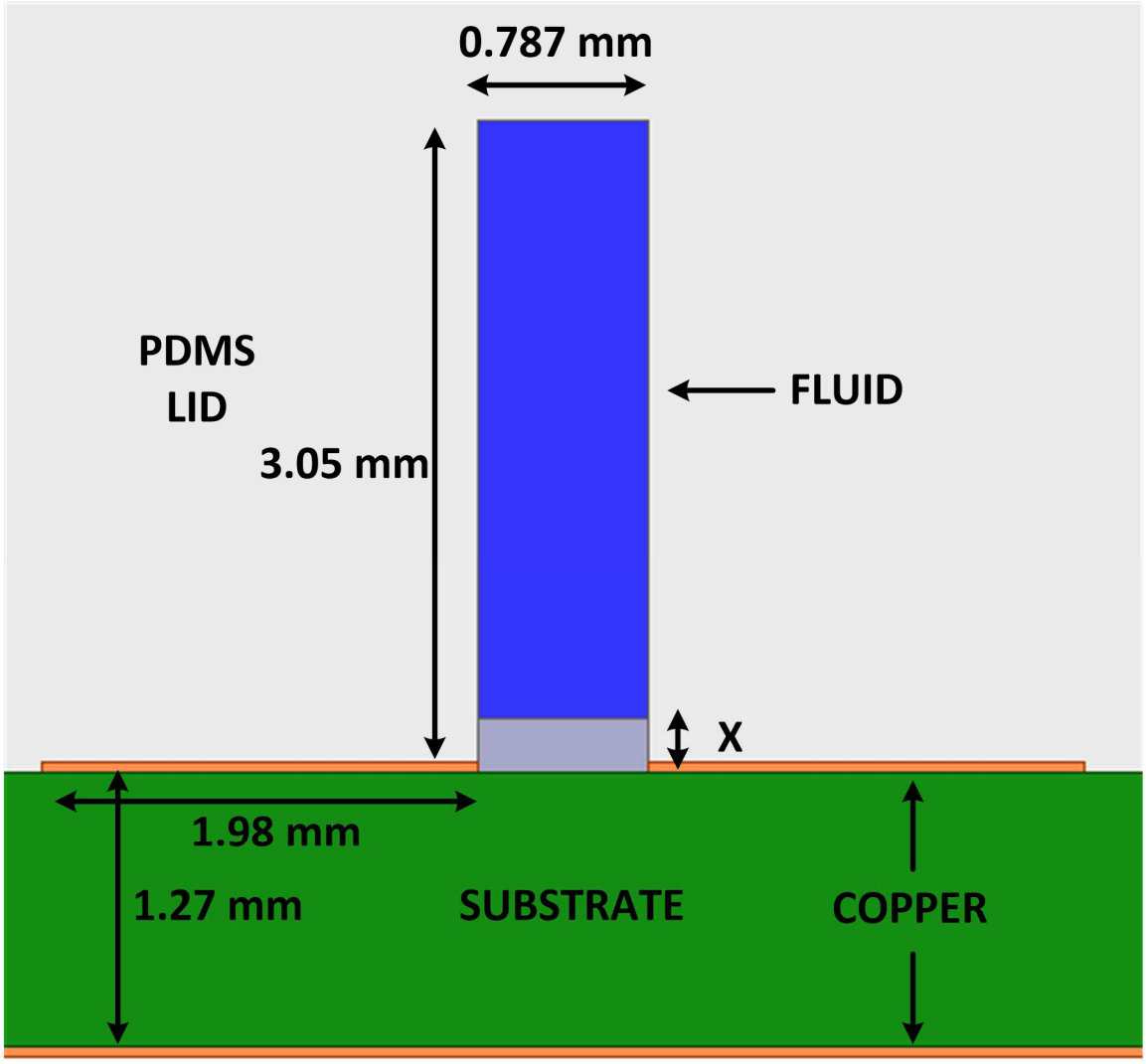

Figure 13 Cross-section of fluidic channel where X=0 mm with no PDMS in channel or X=0.254 mm of PDMS in the channel floor of the coupled region gap spacing

The second design has PDMS (X≈0.254 mm) in the channel floor (Figure 13). This small piece of PDMS in the channel floor isolates the fluid from the host substrate. The piece of PDMS helps constrain the range of odd mode effective permittivity values realizable using liquids between ε_r=1 to ε_r=81 because only a small portion of the electric

field is present in the liquid region. The various equivalent circuit capacitances for the structure are shown in Figure 14. In general capacitance can be defined by Eq. 3.7 where ε is effective permittivity, A is the area of the electrodes the electric field starts and stops, and d is the distance between those electrodes.

$$C = \frac{\varepsilon A}{d} \tag{3.7}$$

C_{FLUID}, C_{PDMS}, and C_{FLOOR} are present in both even and odd mode analysis. In the even mode analysis, a portion of the fringing fields will be represented by these quantities. C_{FLOOR} is only present when PDMS is in the channel floor.

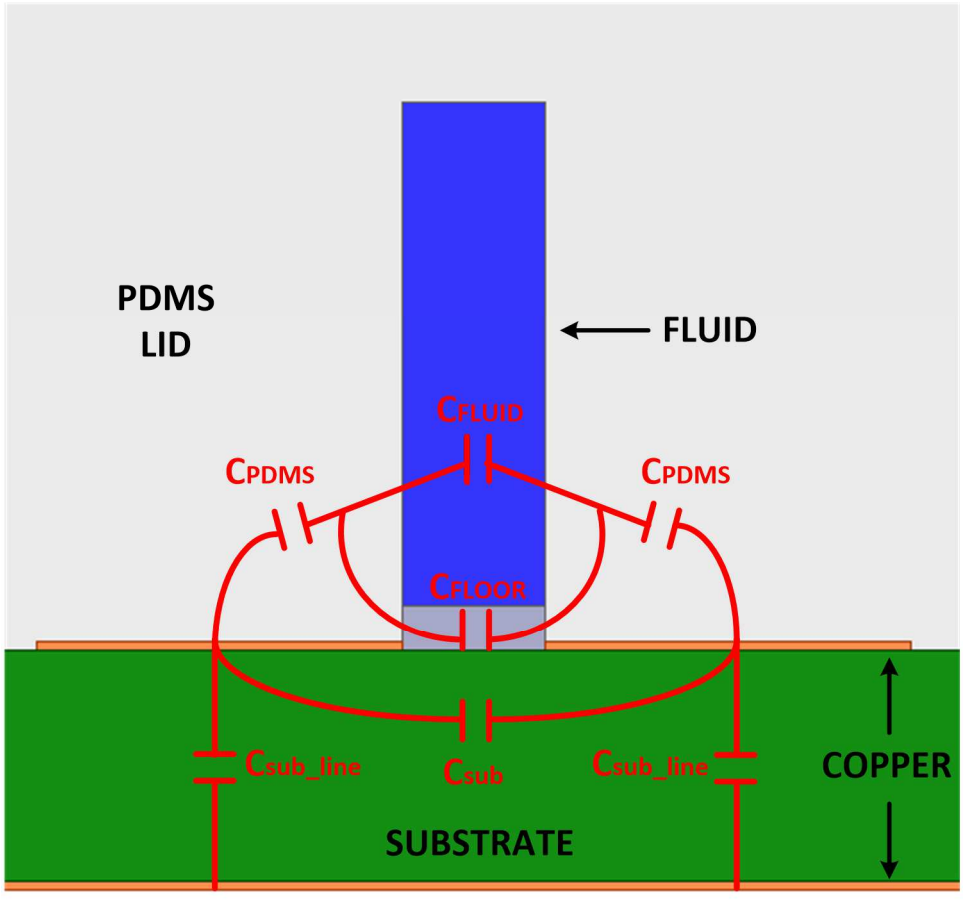

Figure 14 Capacitive equivalent circuit of cross-section microstrip directional coupler

In addition to impacting the directivity, varying the odd mode effective permittivity will vary the coupling. Eq. 3.8 is derived from rearranging Eq. 3.4 and 3.5. The fluid in the channel increases the odd mode effective permittivity and decreases the odd mode characteristic impedance.

$$k = {(Z_{oe} - Z_{oo})}\Big/{(Z_{oe} + Z_{oo})} \tag{3.8}$$

In these designs, especially the design with the PDMS in the channel floor, the even mode effective permittivity is virtually insusceptible to the change in channel fluid because only a small portion of the fringing field penetrates through the fluid. The overall characteristic impedance will stay closer to the desired system impedance based on Eq. 8 since the even mode characteristic impedance stays essentially constant and the odd mode characteristic impedance is only varying slightly.

3.3 Fabrication

The test structure shown in Figure 12 was fabricated on Rogers Duroid RO3006 substrate (ε_r=6.15 tan δ=0.002) using a LPKF milling machine. The substrate thickness is 1.27 mm with half-ounce (17.78 μm) thick copper. The coupled section has a length of 13.97 mm, a conductor width of 1.98 mm, and a gap spacing of 0.787 mm. It is fed with a microstrip feedline length of 27.94 mm and a width of 2.24 mm and is attached to each port of the coupled section.

Similar to Chapter 2, polydimethylsilone (PDMS, ε_r =2.65 tan $\delta \leq 0.001$ at 1 MHz) is the channel material that houses the fluid. The channel above the substrate surface is the same width, 0.787 mm, as the coupled line gap. The channel height is 3.05 mm. A PDMS lid containing this channel is attached to the surface of the substrate over the coupled section using Dow Corning SE 9187 L adhesive. Fluid is injected into this channel through Teflon tubing as shown in Figure 15.

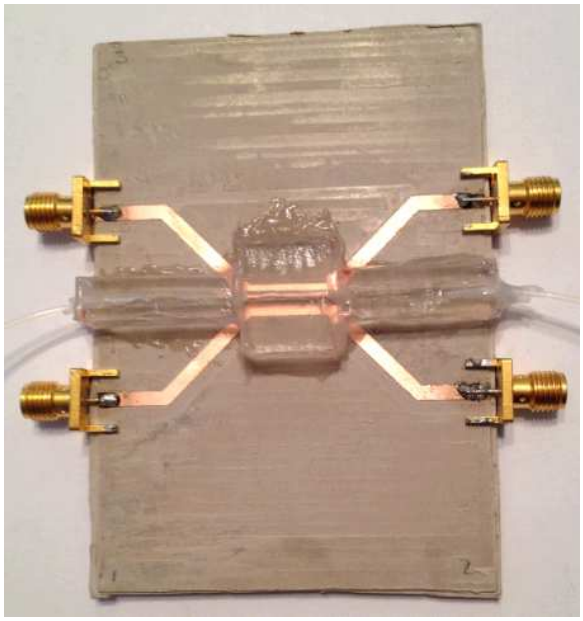

Figure 15 Fabricated directional coupler with PDMS lid

3.4 Characterization

The circuit shown in Figure 15 was tested using an Anritsu network analyzer. S-parameters were collected two ports at a time, terminating the two untested in 50 ohms loads. The objective of this work is to identify tuning range and impact on directivity. Measurement and HFSS [9] simulation results are shown in Figure 16 to Figure 19.

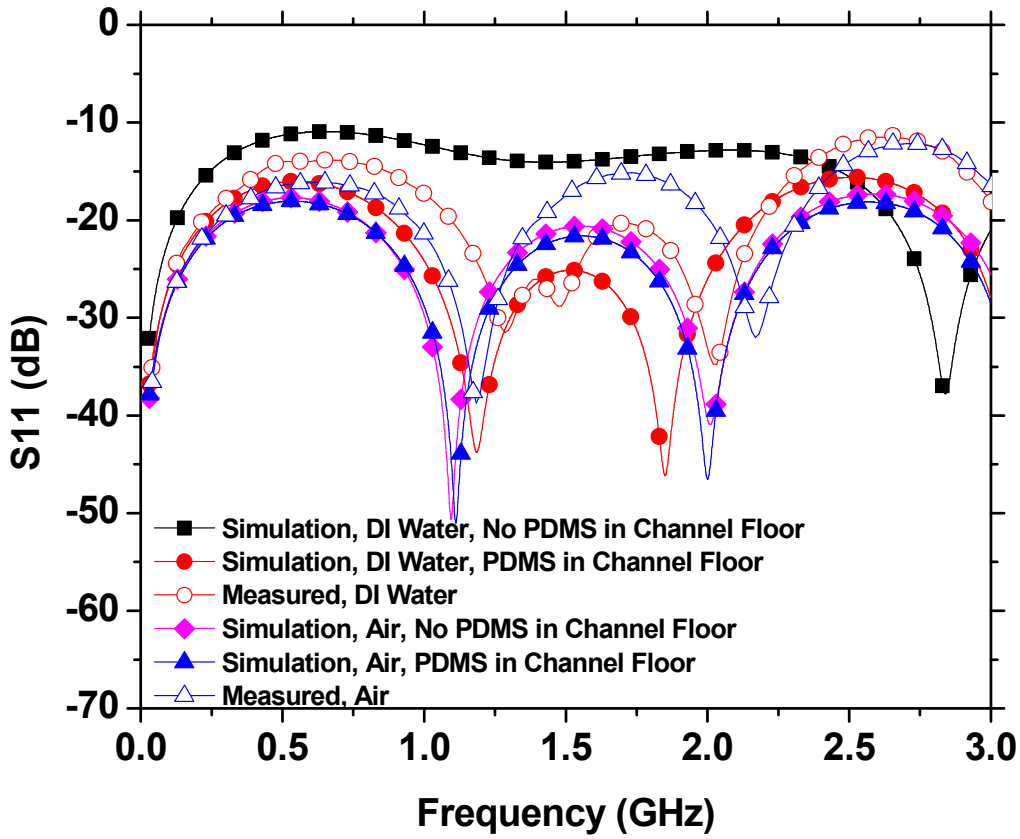

Figure 16 Simulated and measured return loss

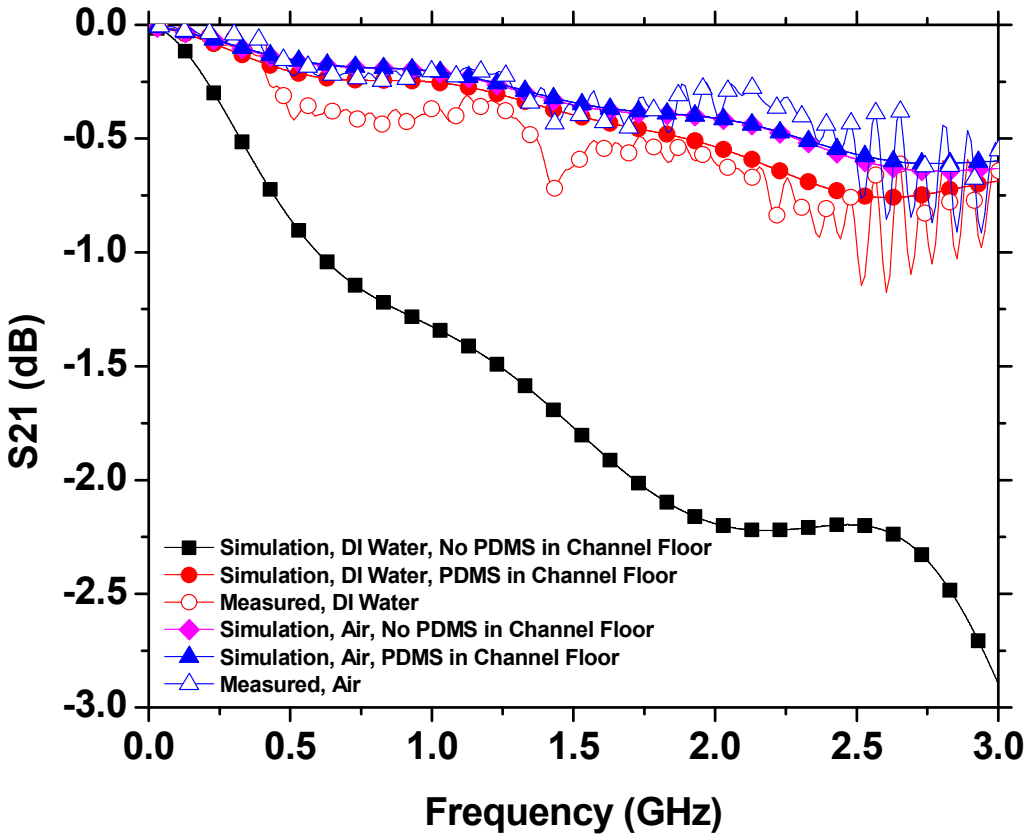

Figure 17 Simulated and measured insertion loss.

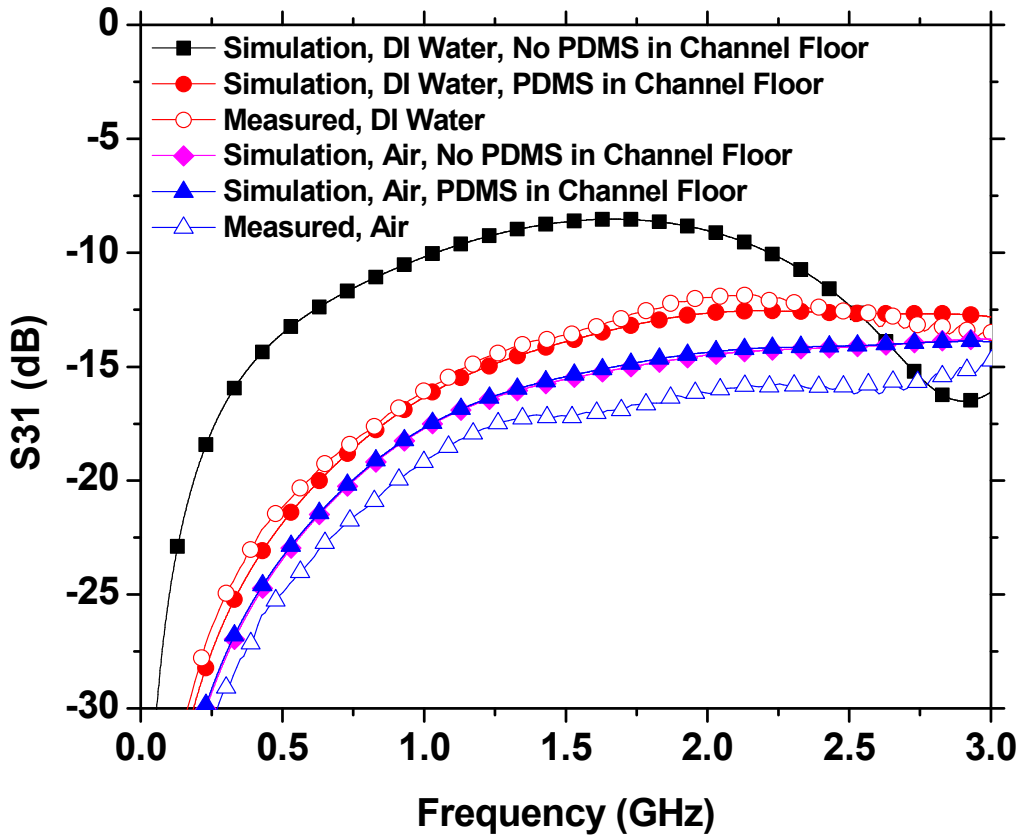

Figure 18 Simulated and measured coupling

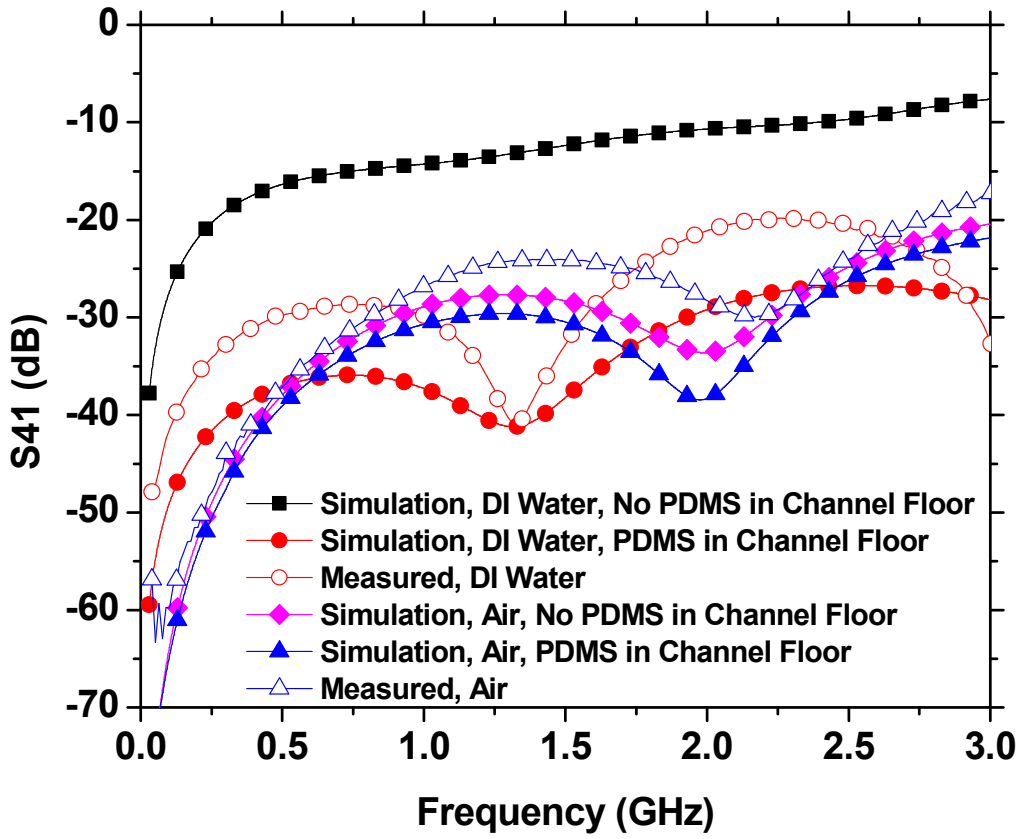

Figure 19 Simulated and measured isolation

In design 1 without the PDMS in the channel floor, the simulated coupling range (Figure 18) between DI (solid squares) and air (solid diamond) is highest (6.96 dB) at 1.5 GHz. However, this comes at the expense of degraded return loss, insertion loss, and directivity. The peak coupling occurs at much lower frequency compared to the peak coupling when the channel is filled with air. As stated in Section 3.2, the peak occurs when the physical length is equal to a guided quarter wavelength. Thus when DI water is in the channel the effective permittivity is increased relative to air causing the coupling peak to occur at a lower frequency for a fixed length of coupled line.

In design 2 by including PDMS in the channel floor, the return loss, insertion loss, and directivity are improved significantly in exchange for a reduced coupling tuning range (simulated, 1.53 dB) near the same frequency. As shown in Figure 16, the return loss is much better because the odd mode characteristic impedance is not reduced as much. By having PDMS in the channel floor, the insertion loss is also improved (Figure 17). Lastly, as shown in Figure 19, the directivity is improved when compared to air over a given frequency range.

The peak coupling frequency does not shift much between when the channel is filled with air and when it is filled with DI water. This is because the change in effective permittivity between the channel filled with air and DI water is less when PDMS is in the channel floor.

3.5 Homogenous Overlay

Simulation and measurement for design 2 (Figure 13) demonstrated good correlation and a slight improvement in directivity using DI water relative to air. DI water has a high dielectric constant when compared to the base substrate, Rogers RO3006. Without PDMS in the floor of the channel, the odd mode propagation velocity is slowed beyond equalization to the even mode when DI water is used (Table 4). Equalization would occur if the microstrip structure where surrounded by a homogenous medium. However, due to the choice the PDMS material as the housing material and the finite permittivity values of readily available fluids, this circumstance is not easily realized.

Silicone oil is a fluid version of PDMS and thus has a much lower permittivity than DI water. This fluid is used to better understand the performance when a homogenous overlay is used. Ansoft Q3D was used to determine propagation velocities and effective permittivities for the even and odd mode. Table 4 summarizes these results.

Table 4 Effective permittivity and propagation velocity for channel filled with various fluids

Fluid	**X (mm)**	ε_{odd}	ε_{even}	v_{odd}	v_{even}
Air (ε_r=1)	0	4.32	5.19	1.44e8	1.32e8
Air (ε_r=1)	0.254	4.50	5.25	1.41e8	1.31e8
DI Water (ε_r=81)	0	12.4	5.48	0.85e8	1.28e8
DI Water (ε_r=81)	0.254	5.01	5.31	1.33e8	1.30e8
Silicone Oil (ε_r=2.65)	3.05	4.65	5.25	1.39e8	1.30e8

Based on the results in Table 4 the use of silicone oil in channel does not equalize the even and odd mode propagation velocities. However, the gap between the two is reduced and the peak coupling does not occur at as low of a frequency as when DI water is used. Also as shown in Figure 20, the change in coupling is less than when DI water is used due to the reduced change in odd mode characteristic impedance (Eq. 3.8).

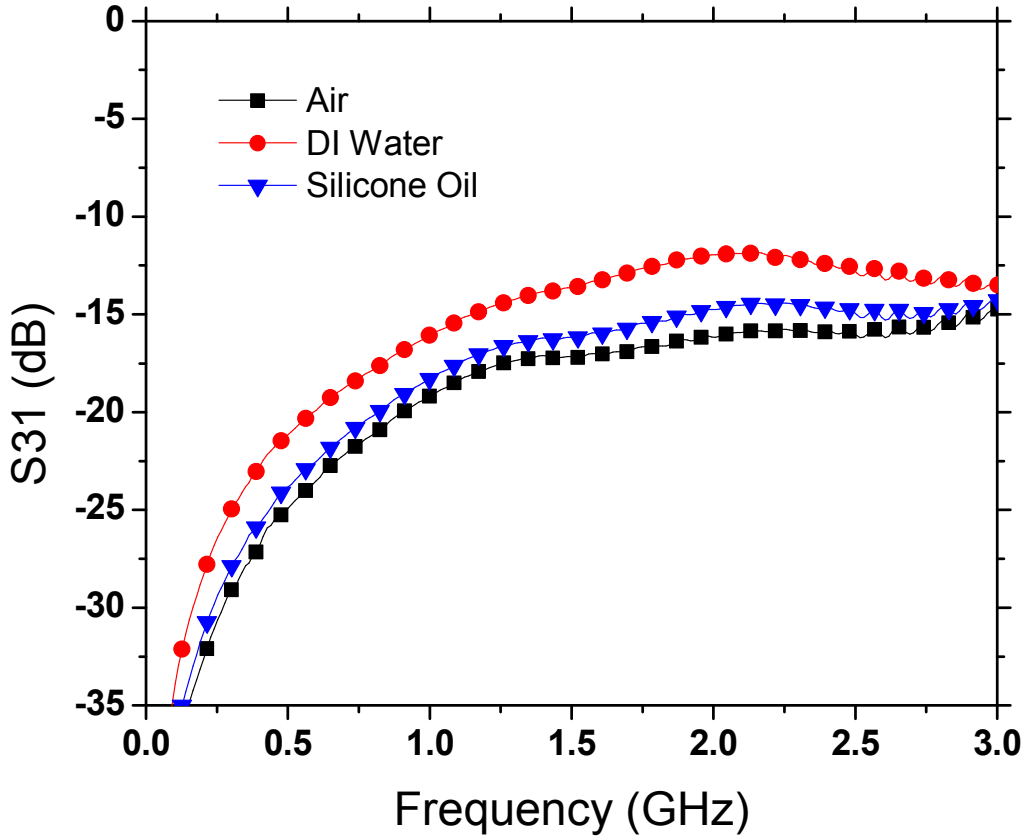

Figure 20 Coupling when channel is filled with either air, DI water, or silicone oil

Eq. 3.1 describes the coupling to port 4 when an input signal is applied to port 1. Evaluating this equation at a minimum power at port 4 reduces the equation to Eq. 3.9.

$$f = \frac{c}{\Delta\sqrt{\varepsilon_{eff}}L} \tag{3.9}$$

Applying this equation to the results in Table 4 suggests that DI water will cause a much larger shift in minimum S_{41} relative to air than silicone oil will relative to air. The measured results in Figure 21 does show a shift to this effect but not the same magnitude of shift.

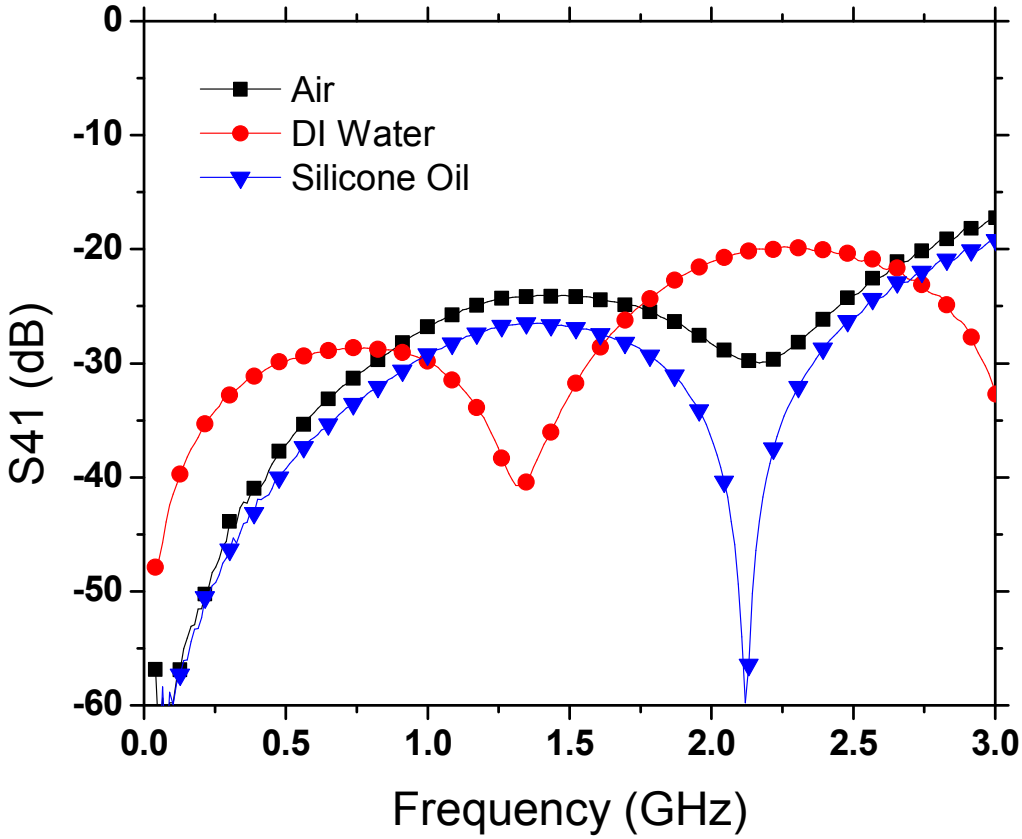

Figure 21 Measured isolation when fluidic channel is filled with either air, DI water, or silicone oil

Directivity is calculated by taking the difference between S_{31} (Figure 20) and S_{41} (Figure 21). Figure 22 shows improved directivity using either silicone oil or DI water compared to air.

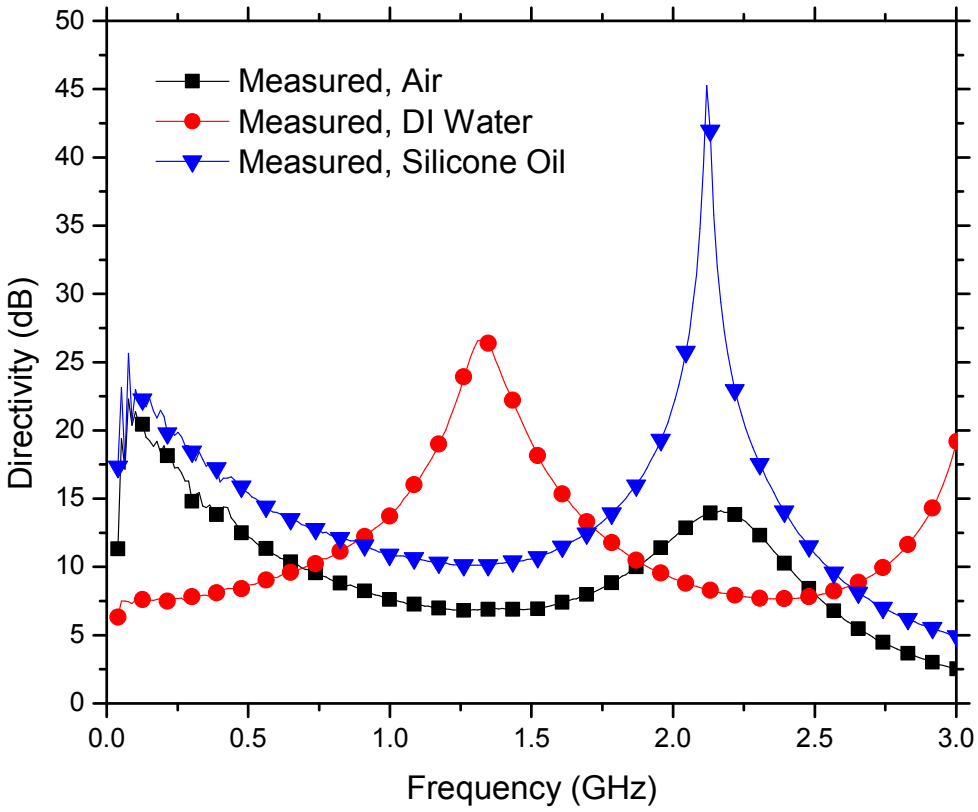

Figure 22 Directivity when fluidic channel is filled with either: air, DI water, or silicone oil

3.6 Conclusion

Two channel architectures used to house fluids in an edge coupled microstrip directional coupler were investigated. Simulation and measured results demonstrated that by inserting a thin layer of PDMS into the channel floor, some coupling range was sacrificed but greatly improved insertion loss by limiting the amount high loss fluid the odd mode interacted with. Additionally, by including PDMS in the channel floor a better matched system over a wider range of fluid permittivity values was realized. The

inclusion of the dielectric fluids did equalize the even and odd mode propagation constants some, resulting in improved directivity of the directional coupler.

4 Fluidic Controlled Annular Slot Antenna

Annular slot antennas have been studied extensively by many research groups [21-26]. Conventional annular slot antennas based off ring resonator theory are inherently high-Q antennas. The integration of this type of antenna with a transceiver is useful for aiding in filtering of radio harmonics and providing selectivity for the receiver. However, with multichannel communication being required for many different communication applications, either multiple antennas, a dynamically adjustable matching network, or a dynamically tunable antenna structure to operate over multiple frequency bands is required. The phased array example shown in Figure 1 would require either a dynamically tunable antenna or matching network to work over multiple frequency bands.

The use of conventional methods such as: capacitors, varactors, and PIN diodes in annular and rectangular slot antenna structures to control the frequency of operation has been extensively studied. Introducing these elements provides frequency tuning by controlling the electrical length of the resonator. Antenna modes are impacted by introducing perturbations into specific locations of the ring resonator structure [21]. For example, in [22] a capacitor is used in an annular slot antenna to demonstrate the potential tuning range of the first mode while varactors are used in [23] to demonstrate frequency tuning over a range for a single and dual-polarized rectangular slot antenna.

Tuning of the second mode while keeping the first mode fixed in frequency is accomplished by placing a varactor in each lateral slot of a rectangular slot antenna [24]. In [27], the ratio of the first and second resonance is varied using a varactor in the slot of a slot antenna.

Most recently, fluids have emerged as an alternative way to create tuning and reconfiguration. Leveraging and integrating fluid control methods developed by the microfluidics community, these types of RF structures offer the promise to be dual function as a sensing element in biomedical and biotechnology applications concerned with monitoring fluidic systems.

The most popular fluid systems use metal fluids. For example, liquid metal (EGaIn) is used to change the electrical length of a slot antenna in [28] by placing a fluidic channel in the substrate and creating an RF short when the liquid is present. A non-planar design, like a circular Yagi-Yuda antenna, with fluidic (mercury) director and reflector elements are pumped around the driven antenna creating a radiation pattern reconfigurable antenna [29].

The work detailed in this chapter investigates the use of fluids for their permittivity properties rather than conductivity properties. Fluidic channels are integrated onto the surface of an annular slot antenna. The fluidic channels are filled with acetone or de-ionized (DI) water and compared to an air benchmark design to demonstrate the frequency tuning range of the antenna structures. Section 4.1 describes the basic theory of modes on annular slot antennas and details the integration of fluidic channels. The first multi-channel configuration (antenna design 1) detailed consists of

parallel channels placed perpendicular to the feedline on the outer half of the annular slot antenna. Design of the structure, simulation results, measurement results, and tolerance sensitivity is detailed in Section 4.2. Through the use of air (baseline), acetone, and DI water, the structure exhibits tunablility of both first and second resonances. However, these resonances are coupled, so a refined second channel configuration and antenna was designed (antenna design 2) to demonstrate independent control of the first and second resonance. Section 4.3 details the design of the structure, simulation results, measurement results, and channel placement/width tolerance sensitivity. Once again air, acetone, and DI water are used to demonstrate the range of tunability of the resonances.

4.1 Annular Slot Electric Field Modes

An unloaded annular slot is resonant when the circumference is integer multiples of a wavelength

$$2\pi r = n\lambda \tag{4.1}$$

where r is mean radius, λ is the guided wavelength, and n is the mode [21]. This work focuses on the first and second modes (n=1 and n=2).

Incorporating a feedline into the structure will have an impact on the Q of the antenna [21]. Two common topologies for feeding an annular slot antenna are: (a) capacitively coupling using a backside microstrip line (Figure 23) or (b) using a coplanar waveguide (CPW) in the same plane as the annular slot (Figure 23). Both designs presented in this chapter use the latter.

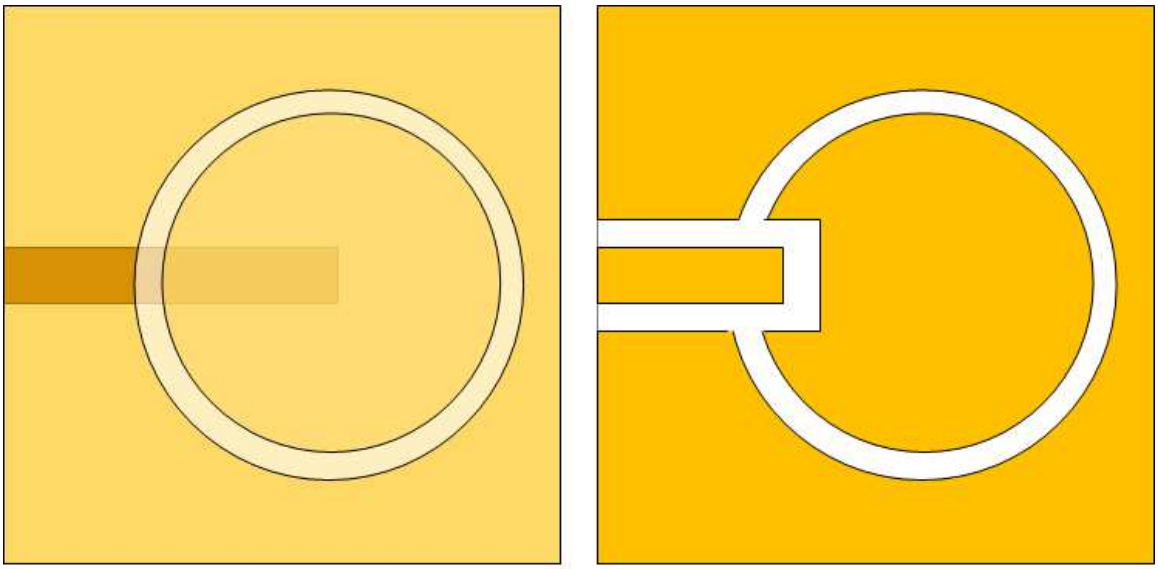

Figure 23 Annular slot common feed topologies. (a) back-side microstrip used to excite slot (b) CPW fed annular slot antenna.

The E-field distributions of the first and second resonant frequencies are shown in Figure 24 and Figure 25, respectively.

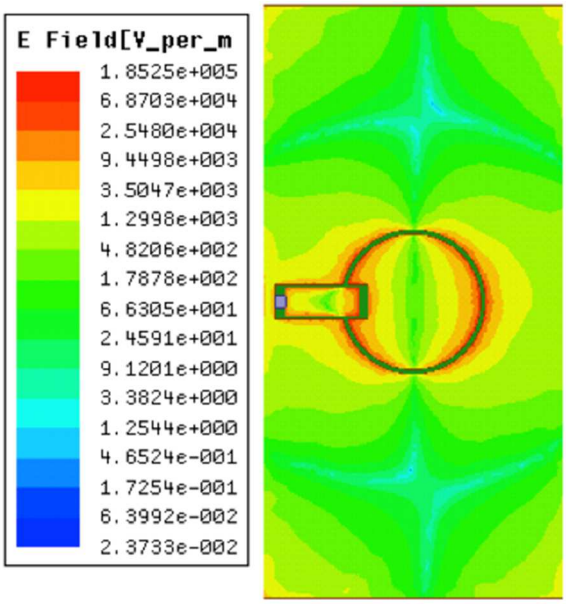

Figure 24 E-field distribution of first resonant mode

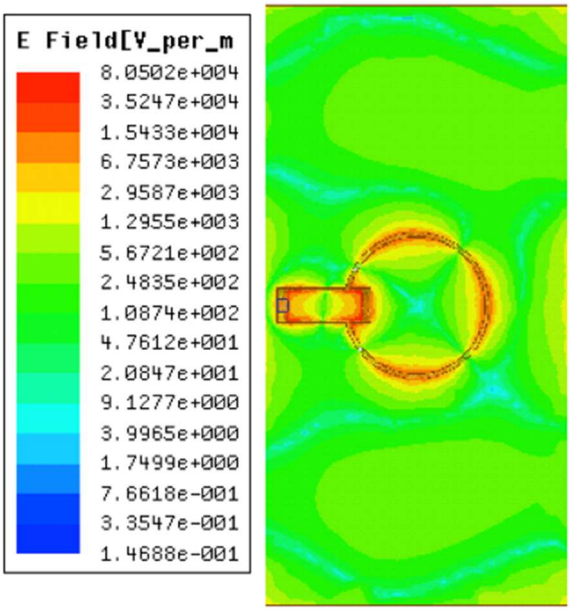

Figure 25 E-field distribution of second resonant mode

The first resonant mode (Figure 24) has E-field maximums along the axis of the field lines and E-field minimums along the axis perpendicular to the feed. The second resonant mode, has two wavelengths around the slot, thus E-field maximums are located along and perpendicular to the axis of the feedline. The nulls are located at approximately ± 45° and ± 135° from the feedline.

4.2 Dual Mode Control Annular Slot Antenna with Parallel Fluidic Channels (Design 1)

A coplanar waveguide fed annular slot antenna with fluidic housing is investigated. Two channels are fabricated perpendicular to the feedline on the half of the annular slot opposite the feed (Figure 26).

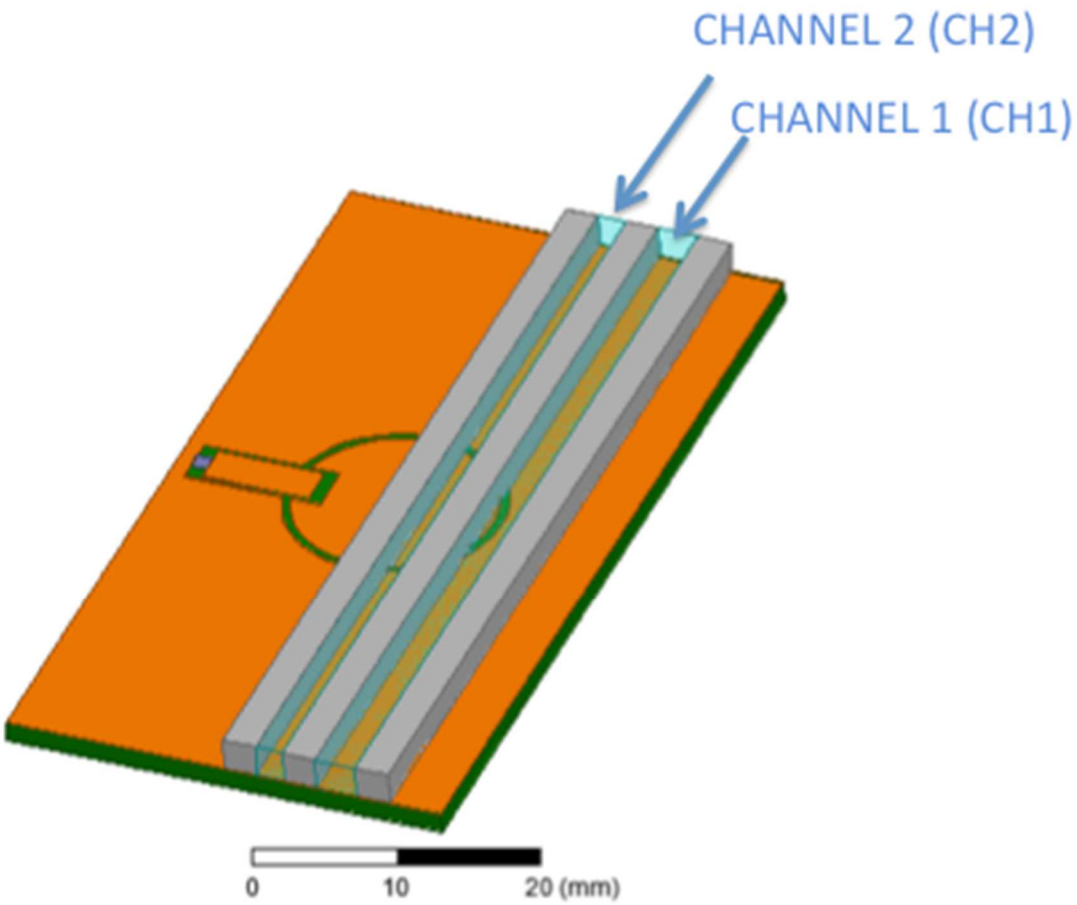

Figure 26 Annular slot antenna with fluidic channels as shown

Section 4.2.1 describes the development of this structure. Section 4.2.2 describes the fabrication and Section 4.2.3 details the simulation and measurement results. Air, acetone, and DI water are used to characterize the range of realizable frequencies due to the wide range of permittivity values they offer (air=1, acetone≈22, and DI water≈81).

4.2.1 Development

The first resonance of an annular slot antenna occurs when the circumference of the slot is equal to a guided wavelength. Operation at a lower frequency, while maintaining the same physical dimensions of the slot, can be achieved by increasing the

electrical length of the antenna through capacitive loading. To maintain the symmetry of the antenna, the first channel (W_{C1}) is run perpendicular to the feed on the portion of the antenna furthest from the feedline (Figure 27).

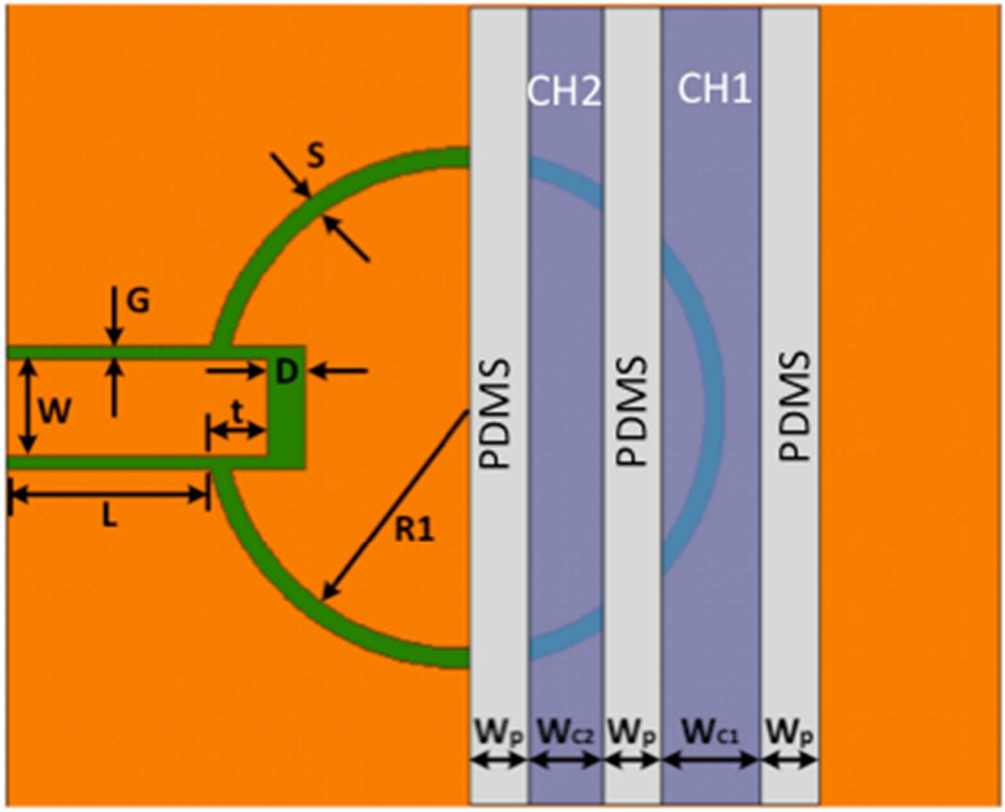

Figure 27 Reference designators of design parameters for both the annular slot antenna and the fluidic housing

This fluidic channel emulates a capacitor loading the open end of the first mode equivalent circuit (Figure 28).

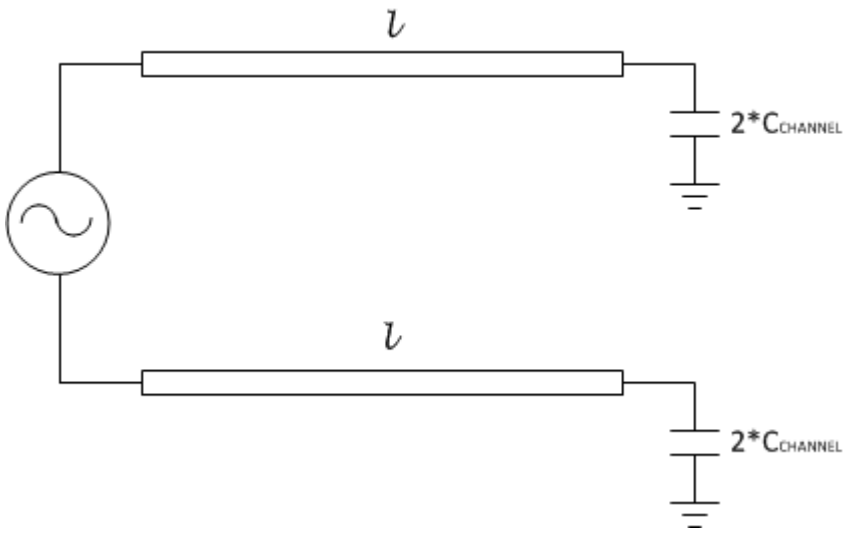

Figure 28 Equivalent circuit model of annular slot antenna when channel 1 (CH1) is filled with fluid

A second channel (CH2) is run parallel to first (CH1) but towards the center of the antenna. When both channel 1 (CH1) and channel 2 (CH2) are filled compared to just channel 1, additional capacitance is added to $C_{CHANNEL}$ and length l is decreased in the equivalent circuit model shown in Figure 28.

The fluidic channels W_{C1} and W_{C2} have widths of approximately 2.1 mm and 1.8 mm. The width (W_P) of each polydimethylsilone (PDMS) wall is 2.3 mm.

The annular slot antenna (Figure 27) was designed using Ansoft HFSS [9]. A CPW feedline impedance of 50 ohms was designed followed by a slot that would create an impedance of about 100 ohms. The antenna has an inner radius (R1) of 7.4 mm and slot width (S) of 0.6 mm. The CPW feedline width (W) is 3 mm and the gap spacing (G) is 0.4 mm. The length of the feedline from the board edge to the outer edge of the annular slot is 6.25 mm (L). The CPW inset into the annular slot and open gap spacing dimensions D and t where parameterized using HFSS to determine the values to provide an acceptable

impedance match over the frequencies of interest for a given feedline length (L). Values of t=1.75 mm and D=1.1 mm were selected.

Electric field distributions for the first and second modes on this structure are shown in Figure 29 and Figure 30. The first mode electric field distribution suggests that filling CH1 with dielectric fluid will impact the first mode frequency response. The magnitude of the electric field in this region is the highest so significant capacitance will be added. Filling CH2 in addition to CH1 will have some additional added capacitance, however should be less due to a lower electric field magnitude in that region compared to CH1. Similarly, there is a finite electric field in each of the channels for the second modes. Thus there will be additional capacitance added when fluid is in either or both of the channels.

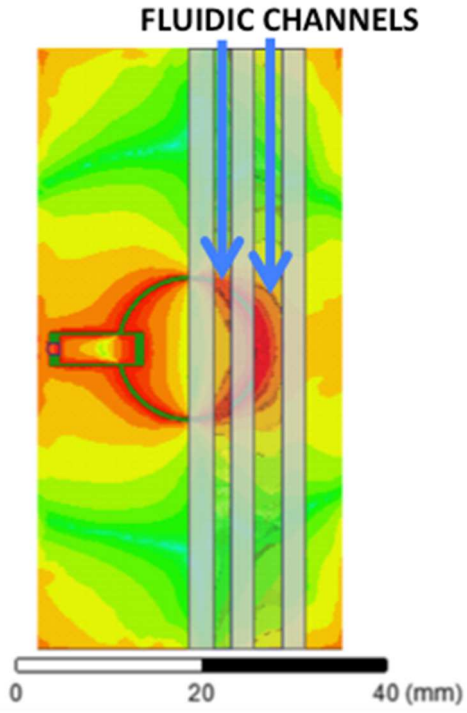

Figure 29 E-field distribution of the first mode. Fluidic channels shown to illustrate impact when either is fiiled.

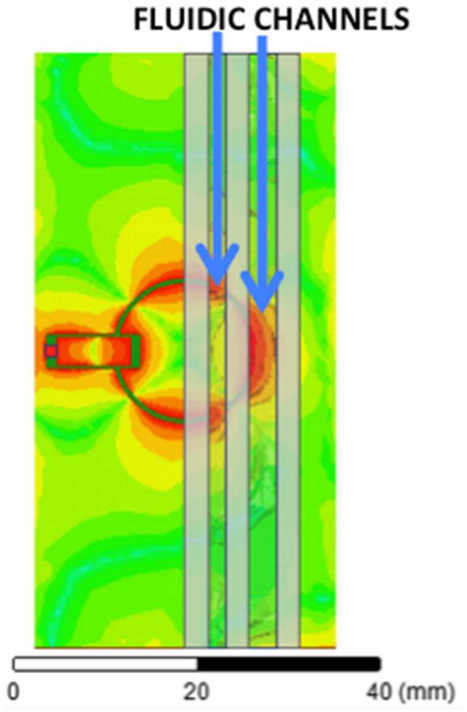

Figure 30 E-field distribution of second mode. Fluidic channels shown to illustrate impact of fluid

4.2.2 Fabrication

The antenna structure was fabricated on FR-4 board (ε_r=4.4, tanδ=0.017) using a LPKF milling machine (Figure 31). The substrate thickness is 1.52 mm and the copper thickness is 17.74 µm.

The fluidic housing was created using polydimethylsilone (PDMS, ε_r=2.65 tan$\delta \leq$0.001 at 1 MHz) and was adhered to the substrate using PDMS adhesive (Dow Corning SE 9187L). Fluid was inserted into the PDMS housing using a syringe. A PDMS lid and Teflon tubing could be used to create a housing in which fluids could be pumped through. Since this was proof-of-concept no lid was attached to the top of the housing. Section 4.3 describes a different antenna with a lid and tubing. Lastly, an SMA connector was soldered to the CPW feedline.

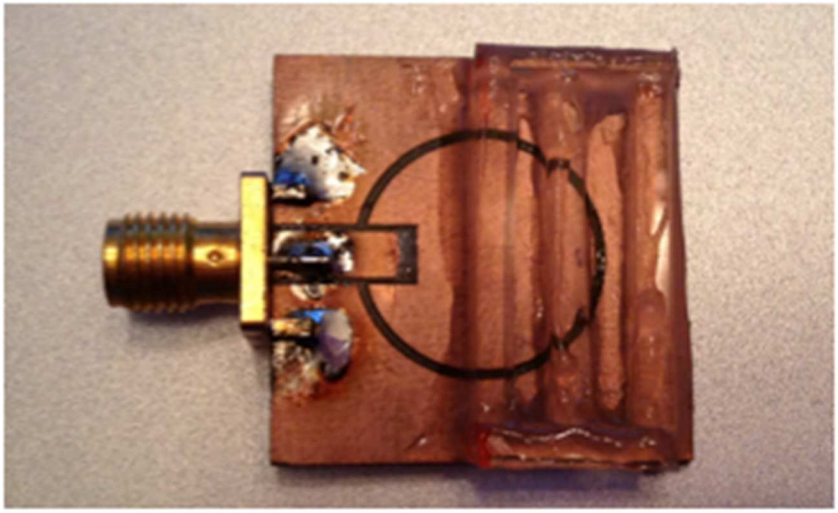

Figure 31 Fabricated annular slot antenna with parallel channel housing

4.2.3 Characterization

4.2.3.1 Return Loss

S-parameters were measured using an Anritsu network analyzer. The frequency range of characterization was 500 MHz to 10 GHz. Figure 32 shows the measured and simulated S11 results of the antenna either with air, acetone, or DI water in channel 1 (W_{C1}) and air in channel 2 (W_{C2}). The first resonance is 4.2 GHz with air, 3.52 GHz with acetone, and 3.05 GHz with DI water. The resonant frequency is decreasing because the load capacitance is increasing from the effective permittivity in the slot. The degradation in S11 with DI water is caused by the loss of the liquid.

In addition to the first resonance shifting downward in frequency, the second resonance is as well. Table 5 summarizes the change in first and second resonant frequencies when the channel is fluid relative to air.

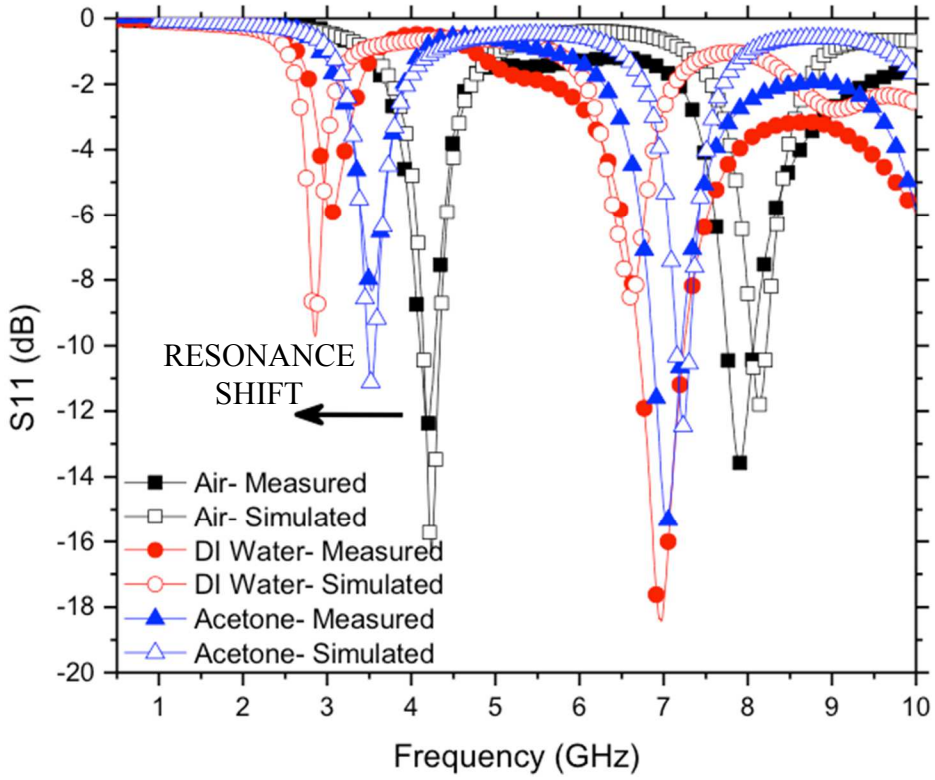

Figure 32 Measured and simulated S11 of the antenna either with air, acetone, or DI water in channel 1 (WC1) and air in channel 2 (WC2). The arrow shows the downward first resonant frequency shift caused by filling channel 1 either with acetone or DI water.

Table 5 Change in first and second resonant frequency with respect to both channels filled with air. Channel 1 filled with either air, acetone, or DI water. Channel 2 filled with air.

Channel 1	Channel 2	1st Resonance (GHz)	Delta from Air (GHz)	2nd Resonance (GHz)	Delta from Air (GHz)
Air	Air	4.20	-	7.90	-
Acetone	Air	3.52	0.68	7.03	0.87
DI Water	Air	3.05	1.15	6.96	0.94

Figure 33 is the measured and simulated S11 results of the antenna with both channel 1 (W_{C1}) and channel 2 (W_{C2}) filled either with air, acetone, or DI water. The first resonance location is not much different than when only CH1 was filled. This is because

the electric field for this mode is not very strong in the location of CH2 on the ring. However, filling CH2 with fluid has a significant impact on the second resonance. The second mode electric field is much closer to peak magnitude in the location of CH2. Once again this can be thought of as a variable capacitor in the slot. The second resonance is 7.9 GHz with air, 5.92 GHz with acetone, and 4.47 GHz with DI water. Table 6 summarizes the change in resonance relative to air for both the first and second modes when fluid is in the channel.

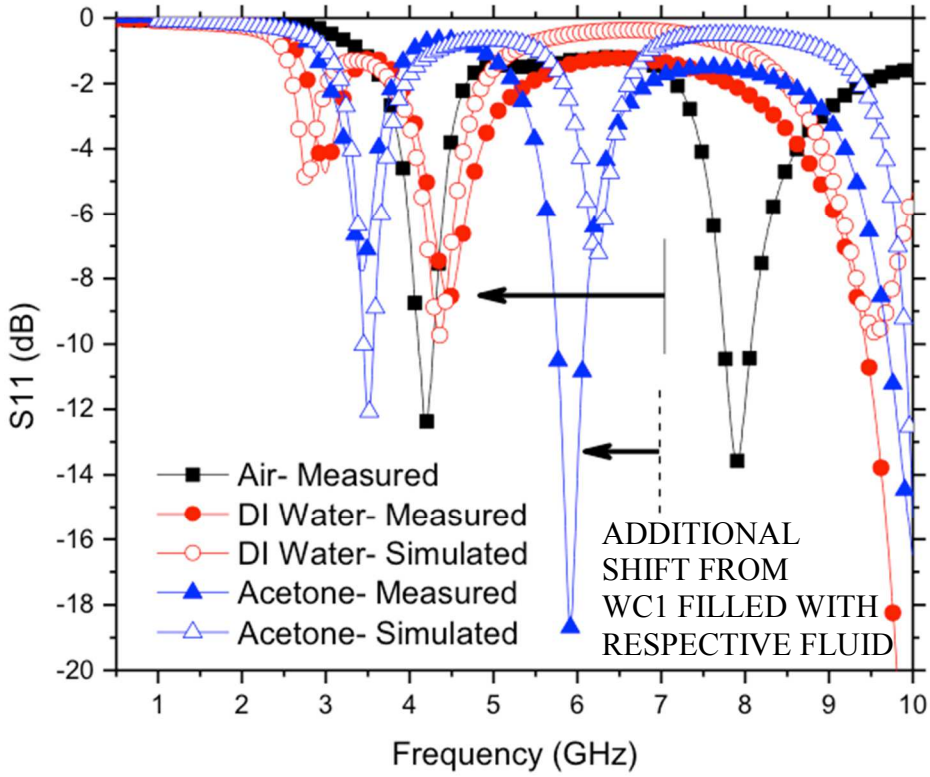

Figure 33 Measured and simulated S11 with both channel 1 (WC1) and channel 2 (WC2) filled either with air, acetone, or DI water. As a reference from Figure 32, the dashed and solid vertical lines show the second resonant frequency when only channel 1 is filled either acetone or DI water.

Table 6 Change in first and second resonant frequency with respect to both channels filled with air. Channel 1 and Channel 2 filled with either air, acetone, or DI water.

Channel 1	Channel 2	1st Resonance (GHz)	Delta from Air (GHz)	2nd Resonance (GHz)	Delta from Air (GHz)
Air	Air	4.20	-	7.90	-
Acetone	Acetone	3.41	0.79	5.92	1.98
DI Water	DI Water	2.97	1.23	4.47	3.43

Lastly, simulation results for CH2 filled with fluid and CH1 filled with air are shown in Figure 34. The first resonance does not shift much while the second resonance shifts considerably. This once again is due to electric field distributions for the respective modes (Section 4.2.1).

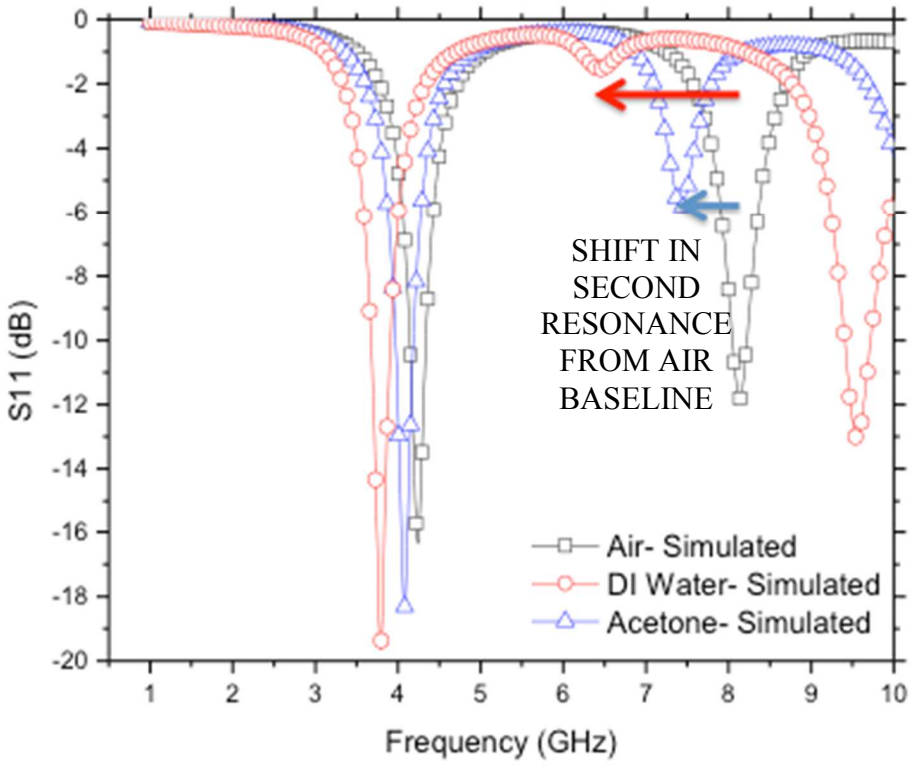

Figure 34 Simulated return loss when channel 2 (CH2) is filled with either air, acetone, or DI water. Channel 1 (CH1) filled with air.

4.2.3.2 Radiation Characteristics

Simulated peak gain and radiation efficiency are given in Table 7 and Table 8. These two quantities describe the radiation characteristics of the antenna. Note that peak gain is related to effective isotropic radiated power (EIRP) by Eq. 4.2.

$$EIRP\ (dBm) = Peak\ Gain\ (dBi) + Input\ Power\ (dBm) \tag{4.2}$$

Input power is the amount of power that is transferred to the antenna. EIRP is usually quoted as maximum value measured at a single angle and is referenced to an isotropic radiator.

Radiation efficiency is related to total radiated power (TRP) by Eq. 4.3.

$$TRP\ (dBm) = Rad.Eff.(dB) + Input\ Power\ (dBm) \tag{4.3}$$

Once again input power is the amount of power transferred to the antenna. TRP is the power calculated by integrating over an entire sphere surrounding the antenna. The difference between EIRP and TRP is directivity.

Table 7 summarizes the peak gain and radiation efficiency of the antenna with CH1 filled with fluid while CH2 is filled with air. There is significant loss in the first resonance when DI water is in CH1.

Table 7 Peak gain and radiation efficiency when channel 1 is filled with air, DI water, or acetone. Channel 2 is filled with air. Loss included in material properties.

Channel 1	Channel 2	1st Resonance (GHz)	Peak Gain (dBi)	Radiation Eff. (dB)	2nd Resonance (GHz)	Peak Gain (dBi)	Radiation Eff. (dB)
Air	Air	4.24	5.90	-0.40	8.14	9.32	-0.89
Acetone	Air	3.52	4.60	-2.11	7.23	6.19	-2.19
DI Water	Air	2.85	-0.41	-5.57	6.61	5.91	-2.65

Table 8 summarizes the peak gain and radiation efficiency of the antenna with CH1 and CH2 filled with fluid. The loss is even further increased.

Table 8 Peak gain and radiation efficiency when channel 1 and channel 2 are filled with air, DI water, or acetone. Loss included in material properties.

Channel 1	Channel 2	1st Resonance (GHz)	Peak Gain (dBi)	Radiation Eff. (dB)	2nd Resonance (GHz)	Peak Gain (dBi)	Radiation Eff. (dB)
Air	Air	4.24	5.9	-0.40	8.14	9.32	-0.89
Acetone	Acetone	3.51	4.64	-2.05	6.23	1.81	-6.13
DI Water	DI Water	2.75	-1.91	-7.53	4.35	-0.22	-6.45

In order to better understand the loss of the fluid in the channel, simulations were run with lossless and lossy fluids. This was done by changing the tanδ in the fluid material properties while leaving the permittivity constant between the two instances. Table 9 is the lossless results of CH1 filled with fluid and CH2 filled with air. The change in radiation efficiency from air to DI water (lossless) in CH1 is 1.18 dB compared to 5.17 dB when loss is included for DI water. Table 10 is the lossless results of CH1 and CH2 filled with fluid. The change in radiation efficiency from air to DI water (lossless) in both CH1 and CH2 is 1.33 dB compared to 7.13 dB when loss is included for DI water.

Table 9 Peak gain and radiation efficiency when channel 1 is filled with air, DI water, or acetone. Channel 2 is filled with air. Loss not included in material properties.

Channel 1	Channel 2	1st Resonance (GHz)	Peak Gain (dBi)	Radiation Eff. (dB)	2nd Resonance (GHz)	Peak Gain (dBi)	Radiation Eff. (dB)
Air	Air	4.24	5.90	-0.40	8.14	9.32	-0.89
Acetone	Air	3.49	6.08	-0.58	7.17	7.68	-0.96
DI Water	Air	2.81	3.64	-1.58	6.46	7.71	-0.52

Table 10 Peak gain and radiation efficiency when channel 1 and channel 2 are filled with air, DI water, or acetone. Loss not included in material properties.

Channel 1	Channel 2	1st Resonance (GHz)	Peak Gain (dBi)	Radiation Eff. (dB)	2nd Resonance (GHz)	Peak Gain (dBi)	Radiation Eff. (dB)
Air	Air	4.24	5.90	-0.40	8.14	9.32	-0.89
Acetone	Acetone	3.49	6.08	-0.58	6.05	6.67	-1.42
DI Water	DI Water	2.7	3.99	-1.73	4.24	5.86	-0.96

Figure 35 shows the circuit simulated and the reference coordinate system. This same coordinate system is used when plotting the 3D polar plots.

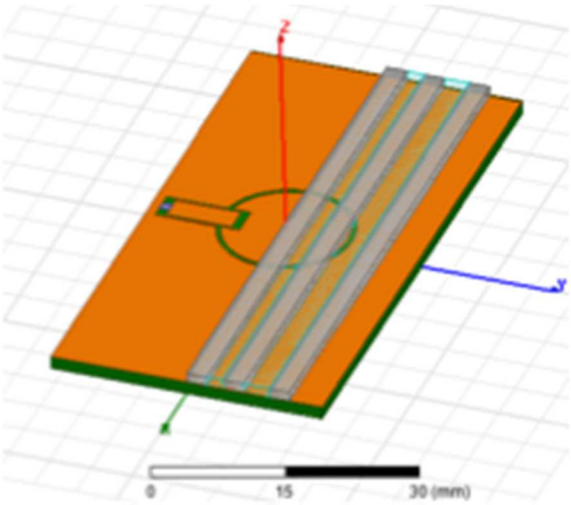

Figure 35 Circuit used for simulation of antenna. Includes fluidic channels.

Figure 36 is an example of the gain 3D polar plot at the first resonant frequency. This general pattern is representative of the first mode for all instances of CH1 and CH2 with or without fluid. The peak gain is along the axis perpendicular to the board.

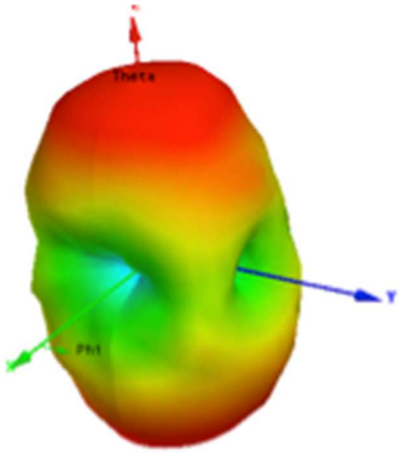

Figure 36 Radiation pattern of first resonance

Figure 37 is an example of the gain 3D polar plot at the second resonant frequency. This general pattern is representative of the second mode for all instances of CH1 and CH2 with or without fluid. The pattern is not one of classical antennas. Despite not having well defined, highly predictable peaks and nulls, this type of radiation pattern still may be useable in high multi-path environments or even body worn applications.

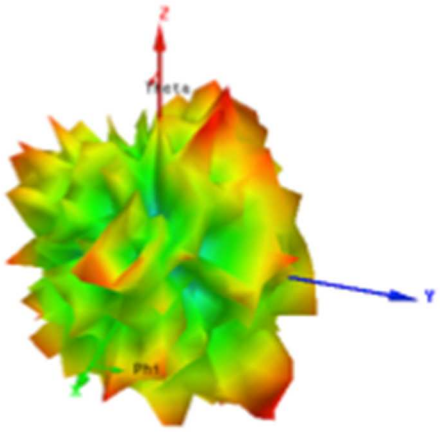

Figure 37 Radiation pattern of second resonance

4.3 Annular Slot Antenna with Fluidic Channels Realizing Independent Control (Design 2)

Section 4.2 introduced using fluids on the surface of an annular slot antenna to control resonant frequencies. One drawback to the design presented in Section 4.2 was that independent control of the resonant frequencies was not achieved. This section details a design that does indeed achieve independent control. The channel configuration and channel reference designators are shown in Figure 38.

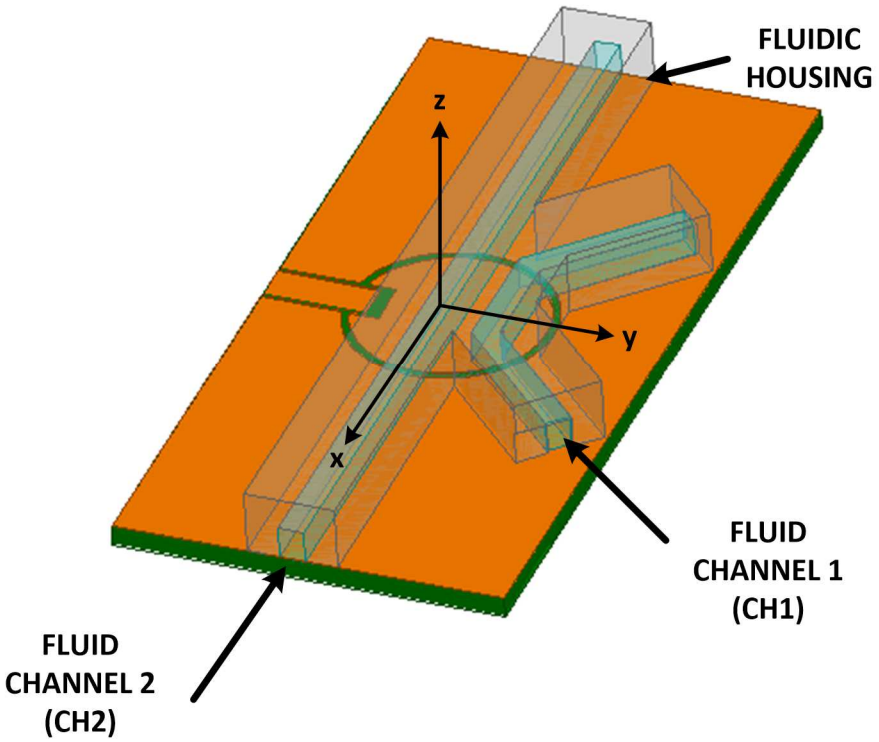

Figure 38 Annular slot antenna with fluidic channels integrated on surface. Channel 1 angled at 45 degrees from the y-axis.

4.3.1 Development

As noted in Section 4.1 an annular slot is resonant when the circumference of the ring is equal to integer multiples of a wavelength. The design in this section characterizes the first and second order modes of the ring.

Independent frequency tuning of the first and second order resonances is achieved through proper placement of fluidic channels with respect to these modes. The E-field distributions of the first and second resonant frequencies are shown in Figure 39 and Figure 40, respectively. As seen along the x-axis, the first resonance has an E-field minimum (Figure 39) while the second resonance has an E-field maximum (Figure 40) along the same direction. Placing a fluidic channel (CH2) along the x-axis and varying

the permittivity of the fluid in the channel causes the second resonance frequency to shift without displacing the first resonant frequency.

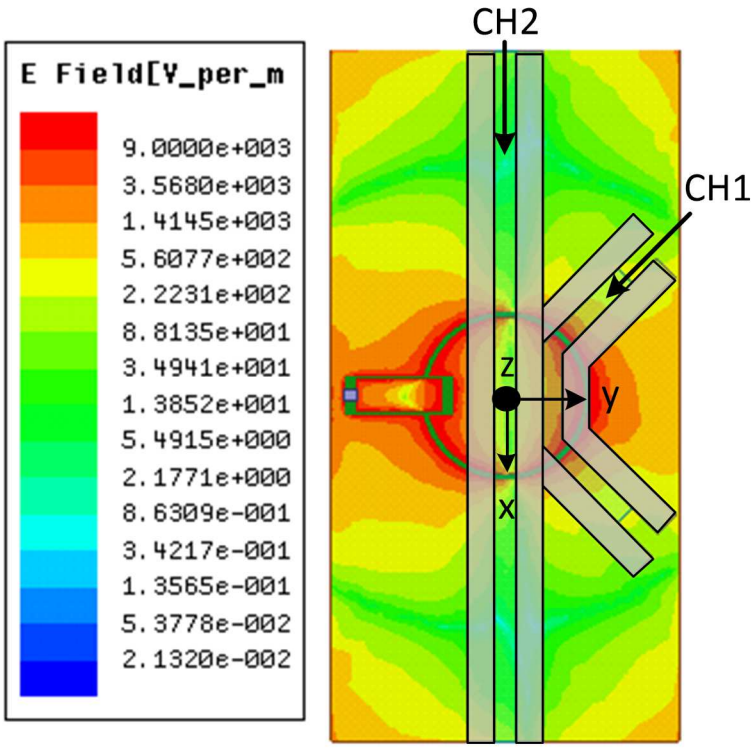

Figure 39 E-field distribution of first resonant mode (4.2 GHz)

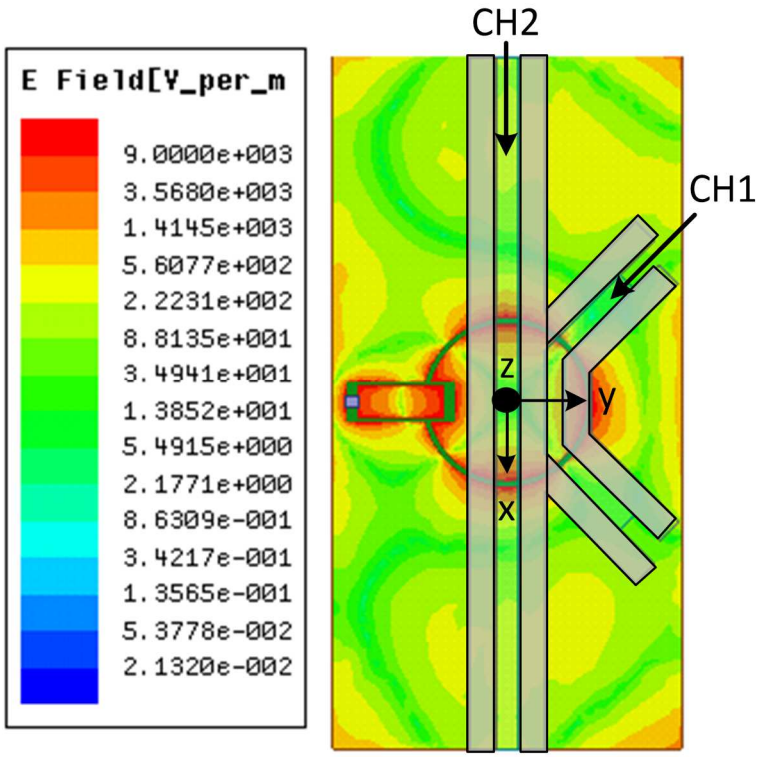

Figure 40 E-field distribution of second resonant mode (8.07 GHz)

To decouple the movement of the first and second resonant frequencies, the fluidic channel location must be placed where the E-field is a minimum for the fixed frequency resonance. For example, to make the first resonant frequency tunable and the second resonant frequency a constant, the fluidic channel (CH1) is placed where the second resonant (constant) frequency is a minimum (Figure 40) and the first resonant frequency is not at a minimum (Figure 39). This occurs at an angle of approximately +/- 45 degrees from the y-axis (CH1).

4.3.2 Fabrication

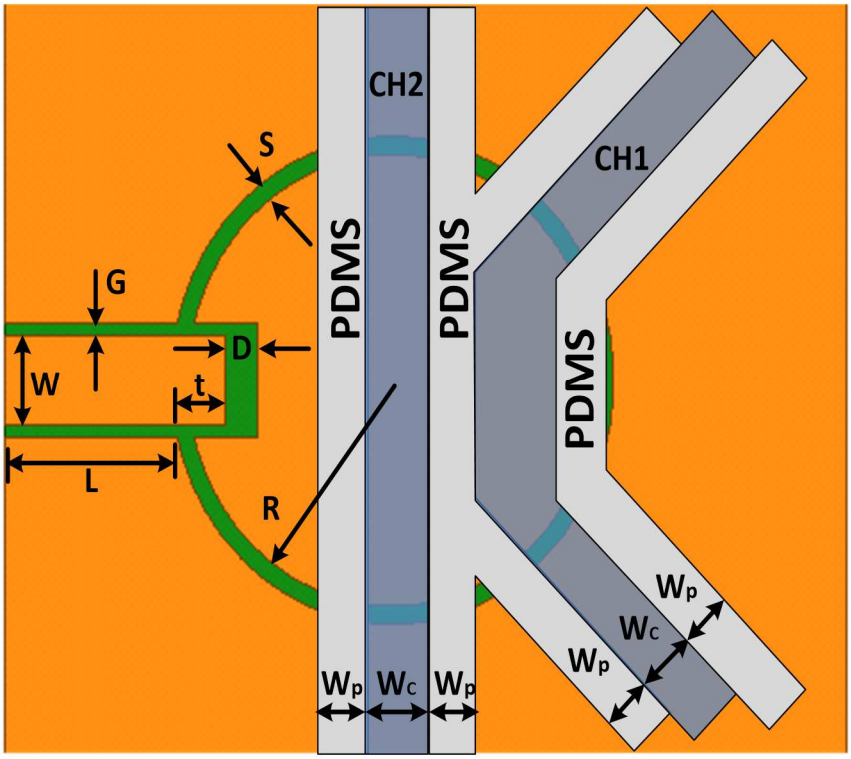

Figure 41 Parameters used to define test structure

A structure to validate this concept was fabricated using an LPKF milling machine. The substrate material used for this test structure is 1.52 mm FR-4 (ε_r=4.4, tanδ=0.001). The annular slot has an inner radius of 7.4 mm (R) and a slot width (S) of 0.6 mm (Figure 41). The coplanar waveguide (CPW) feedline dimensions are chosen to be approximately 50 ohms. The trace width (W) is 3 mm and the gap spacing (G) is 0.4 mm. The length (L) of the feedline from the board edge to the outer edge of the annular is 6.25 mm. The feedline is extended 1.75 mm (t) into the ring. The gap spacing between the feedline and inner copper plane is 1.1 mm (D). The gap spacing (D) and

stub length (t) were parameterized in simulation and determined to produce an acceptable reflection coefficient.

The fluidic channels are fabricated using polydimethylsiloxane (PDMS, $\varepsilon_r \approx 2.65$) and are attached to the substrate using PDMS adhesive. The PDMS wall widths (Wp) are 2.3 mm and the height is 2.5 mm. The channel width (Wc) is 2.1 mm. An additional layer of PDMS is attached on top of the channels using PDMS adhesive to create a housing. Teflon tubing is inserted at each channel port (Figure 42).

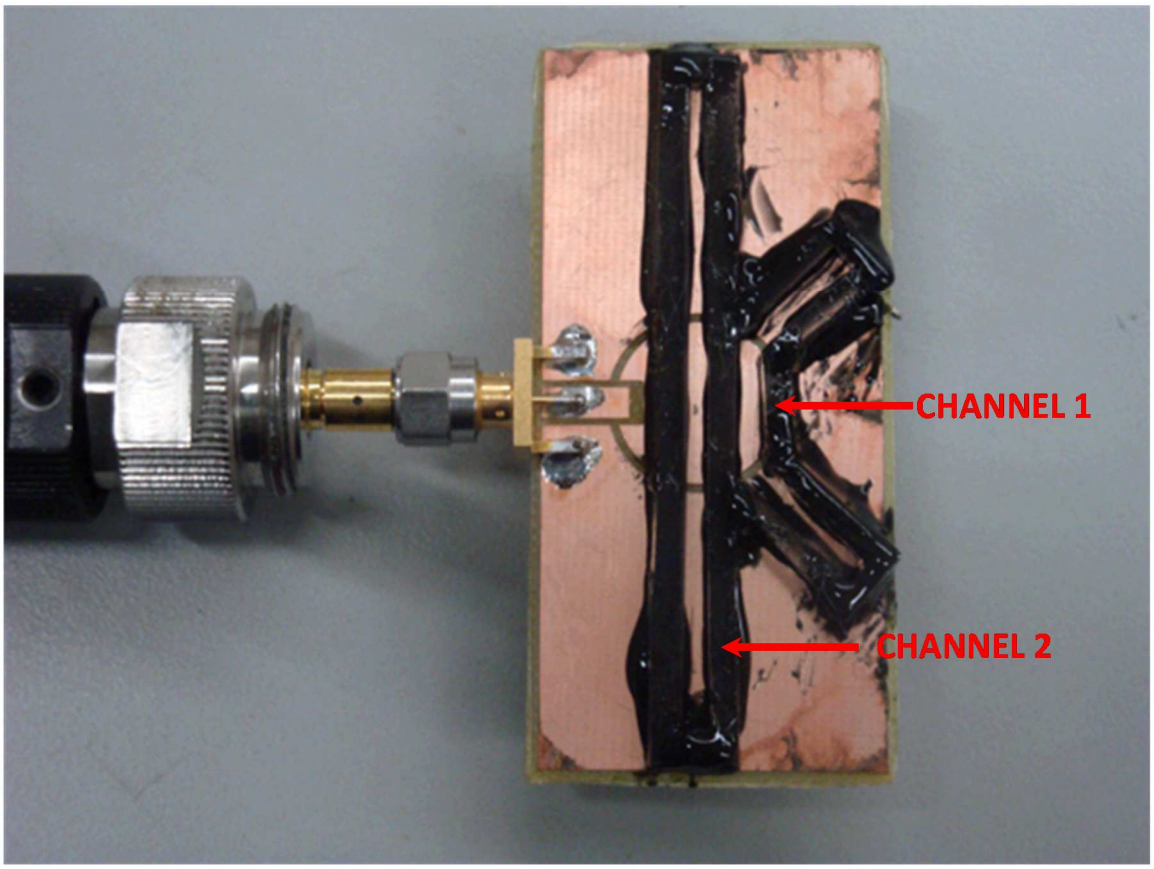

Figure 42 Fabricated antenna with fluidic channels

4.3.3 Characterization

Reflection coefficient and antenna radiation patterns were measured using an Anritsu 37369D network analyzer. Simulations were performed using Ansoft HFSS. The material properties for DI water (ε_r=74, tanδ=0.2 at 4 GHz) and acetone (ε_r=23, tanδ=0.12 at 4 GHz) are used in the simulation models [20].

Far-field radiation patterns were measured in an anechoic chamber using the gain-transfer method [32]. Measurement and calibration results are based on using horn antennas. Due to turntable capabilities only the x-z plane could be measured (Figure 38). All measurements were performed at room temperature.

4.3.3.1 Reflection Coefficient

Measured and simulated S11 results for CH1 filled with air, acetone, or DI water and CH2 filled with air are shown in Figure 43. The first resonance shifts from 4.2 GHz (air in both channels) to 3.8 GHz with acetone in CH1 or 3.3 GHz with DI water in CH1. The second resonance is 8.07 GHz when both CH1 and CH2 are filled with air. The second resonance shifts downward 0.4 GHz when acetone is in CH1. Simulated S11 for the second resonance with DI water in CH1 is 7.54 GHz, however the resonance is not as strong in measurement. This is likely due to fabrication tolerance, both placement and width of CH1, being exacerbated because of the high ε_r of DI water. Figure 40 shows that exact placement of the channel must occur otherwise the second resonance will be affected. Simulation analysis of channel width tolerance was performed and a change in channel width of 100 μm shifted the second resonance 20 MHz. More details on channel

width tolerance are given in Section 4.4.

Table 11 summarizes the change in frequency when fluid is channel 1 and channel 2 is filled with air relative to when both channels are filled with air.

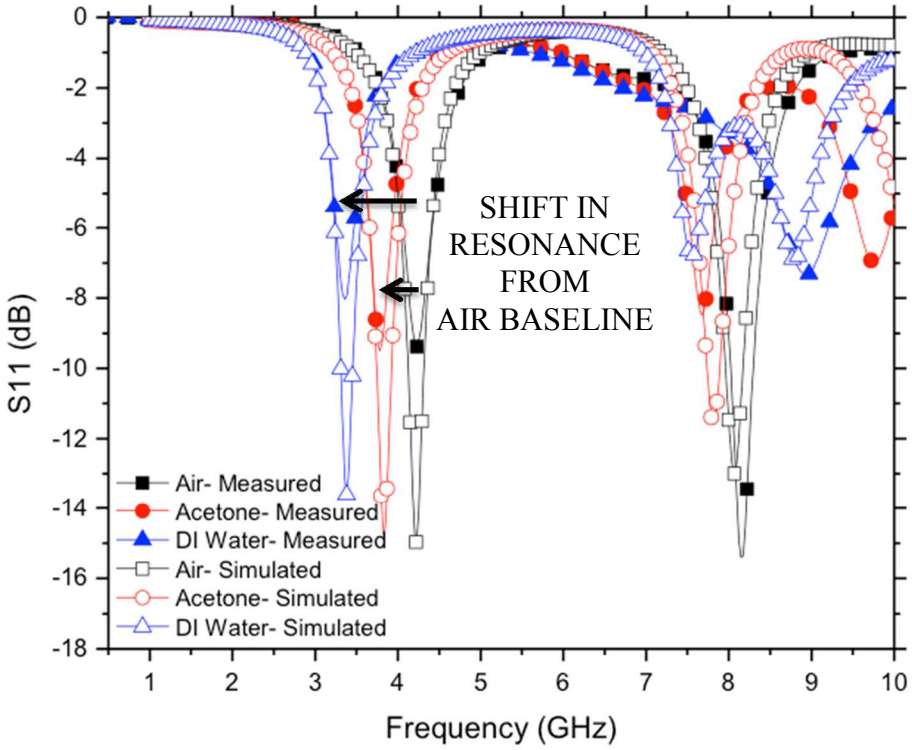

Figure 43 Channel 1 (CH1) filled with either air, acetone, or DI water and channel 2 (CH2) filled with air

Table 11 Change in first and second resonant frequency with respect to both channels filled with air. Channel 1 filled with either air, acetone, or DI water. Channel 2 filled with air.

Channel 1	Channel 2	1st Resonance (GHz)	Delta from Air (GHz)	2nd Resonance (GHz)	Delta from Air (GHz)
Air	Air	4.2	-	8.07	-
Acetone	Air	3.8	0.5	7.67	0.40
DI Water	Air	3.3	0.9	7.54	0.53

Figure 44 shows the measured and simulated reflection coefficient results for CH1 filled with air and CH2 filled with either air, acetone, or DI water as the fluid. Inserting DI water into CH2 causes a downward frequency shift of 2.8 GHz (from 8 GHz to 5.2 GHz) in the second resonant frequency while the first resonance only shifts 70 MHz. Acetone has a lower permittivity than DI water and causes a shift downward of 1.25 GHz from air when inserted in CH2. The first resonance shifts downward approximately 50 MHz. Simulation is in good agreement with measurement. Table 12 summarizes the measured change in frequency when channel 2 is filled with acetone or DI water relative to air.

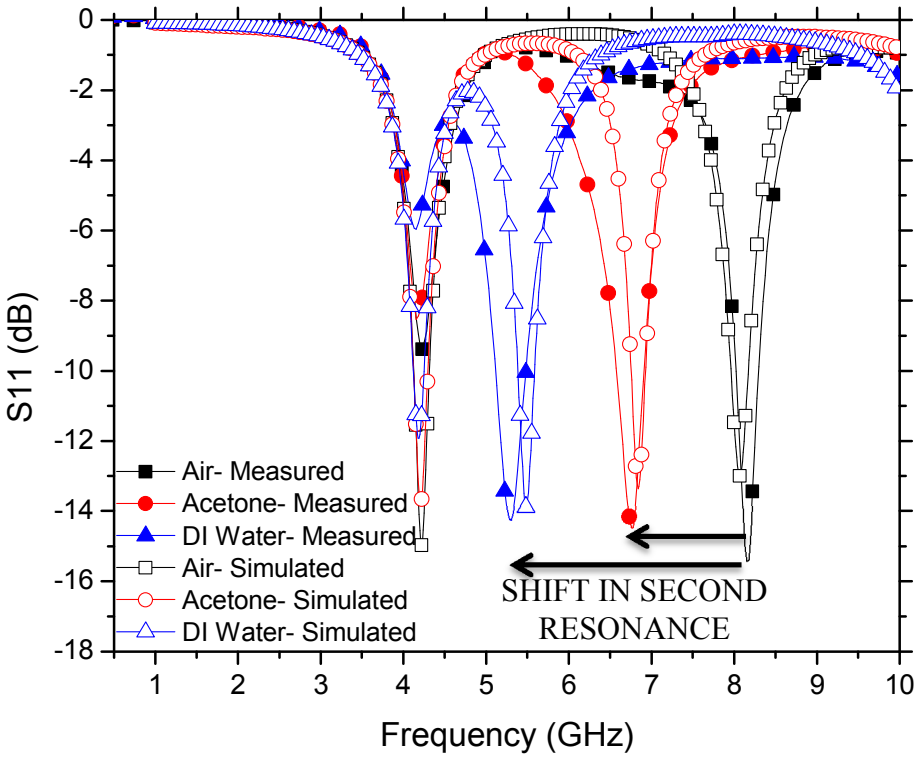

Figure 44 Channel 1 (CH1) filled with air and channel 2 (CH2) filled either with air, acetone, or DI water.

Table 12 Change in first and second resonant frequency with respect to both channels filled with air. Channel 1 filled with air. Channel 2 filled with either air, acetone, or DI water.

Channel 1	Channel 2	1st Resonance (GHz)	Delta from Air (GHz)	2nd Resonance (GHz)	Delta from Air (GHz)
Air	Air	4.22	-	8.00	-
Air	Acetone	3.17	0.05	6.75	1.25
Air	DI Water	4.15	0.07	5.20	2.80

"Fluid" will be used to describe one of the three (air, acetone, or DI water) for simplification. The smallest frequency shift of 0.9 GHz is observed when fluid is placed in CH1 and air is placed in CH2. A shift of 2.8 GHz is achieved when fluid placement in the channel is reversed and air placed in CH1 and fluid in CH2. The larger resonance shift occurs when fluid is placed in CH2 compared to CH1 because the fluidic channel is located at a stronger E-field magnitude. CH1 could not be located at the E-field maximum (Figure 39) of the first mode because it also needed to be located at an E-field minimum of the second mode (Figure 40).

4.3.3.2 Radiation Pattern

Figure 45 shows the measured and simulated radiation patterns in the x-z plane for the first and second resonances when CH1 and CH2 are either filled with air or DI water.

Figure 45(a) shows the radiation pattern when CH1 and CH2 are filled with air. At the first resonance (4.2 GHz) the measured E-phi gain is 2.01 dBi and the E-theta gain is -5.10 dBi. The second resonance has a maximum E-phi gain of 3.51 dBi and E-theta gain of -5.46 dBi.

Figure 43 shows when fluid is inserted in CH1 while air is in CH2, the first resonance will shift downward in frequency while the second resonance is held essentially constant. Thus, inserting DI water into CH1 shifts the first resonance from 4.2 GHz to 3.3 GHz. The x-z radiation pattern at 3.3 GHz is shown in Figure 45(b). The measured E-phi gain is 5.18 dB lower than when both channels were filled with air (Figure 45(a)). A portion of this difference is due to the difference in reflection coefficient (Figure 43). Additionally, some of this loss is attributed to the high loss tangent of DI water. Simulated results, using acetone, with its lower loss tangent, in CH2 suggest only a 0.04 dB reduction in E-phi gain from air while the reduction with DI water is 1.84 dB. The second resonance remains at 8 GHz, essentially the same frequency observed when both channels are filled with air. The E-phi gain is -0.43 dBi and the E-theta gain is 1.23 dBi.

Next, the second resonance is shifted to 5.2 GHz when DI water is inserted into CH2 and air in CH1. The radiation pattern for the x-z plane is shown in Figure 45(c). The E-phi gain is -3.99 dBi and the E-theta gain is -11.73 dBi. The first resonance at 4.2 GHz has an E-phi gain of -0.06 dBi, degraded 2.07 dB from when CH1 and CH2 are filled with air. A portion of this is also due to the difference in reflection coefficient (Figure 44).

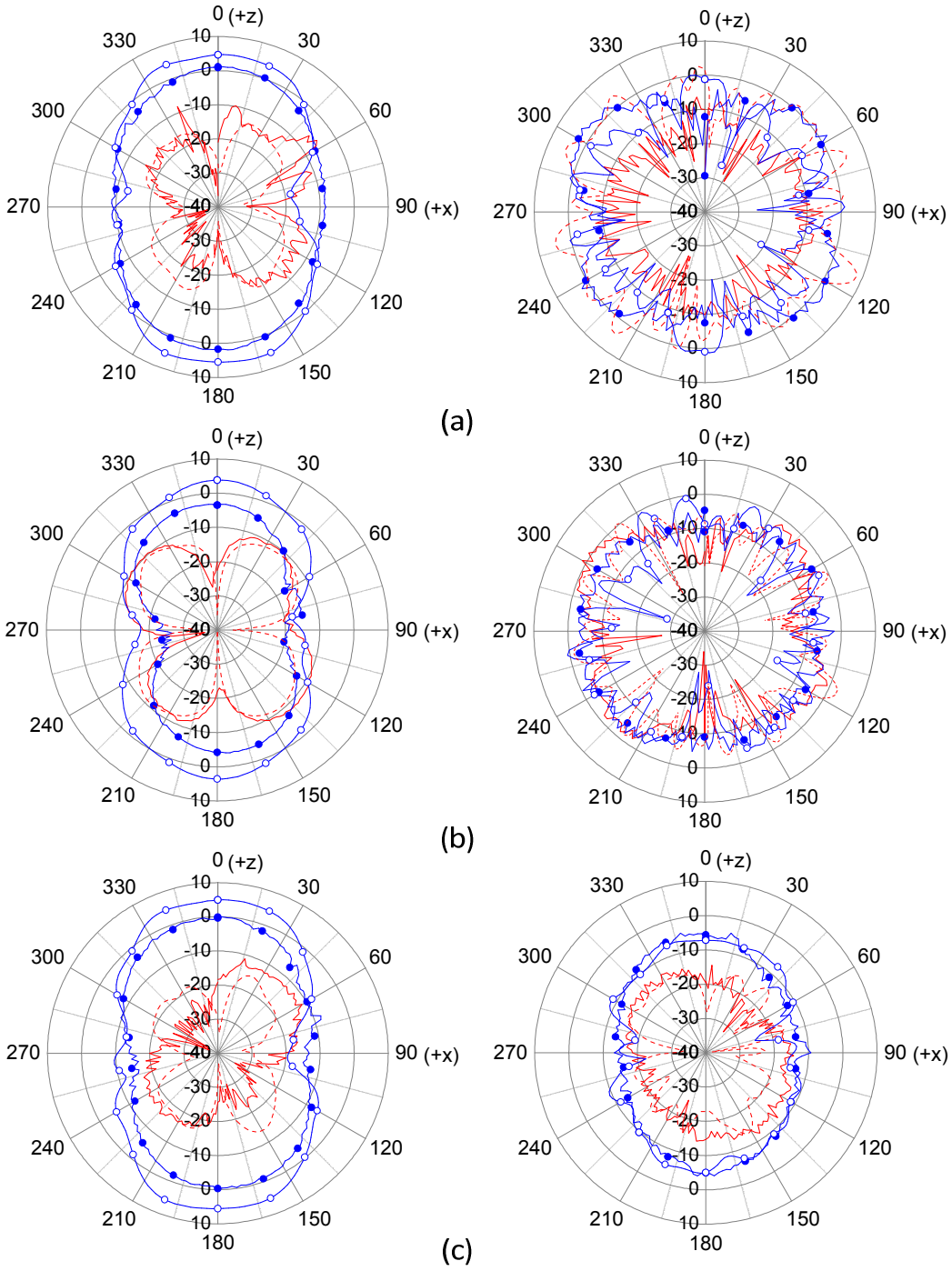

Figure 45 X-Z plane radiation patterns where: E-phi measured (—●—) and simulated (—○—). E-theta measured (——) and simulated (------). (a) CH1 and CH2 are filled with air (left figure 4.2 GHz, right figure 8 GHz) (b) CH1 filled with DI water and CH2 filled with air (left figure 3.3 GHz, right figure 8 GHz) (c) CH1 filled with air and CH2 filled with DI water (left figure 4.2 GHz, right figure 5.2 GHz)

Only the x-z plane was measured due to turn-table limitations. As a result, radiation efficiency could not be measured since data from the other planes is required. Table 13 summarizes the simulated radiation efficiency with lossy fluids whereas Table 14 summarizes the simulated radiation efficiency of lossless fluids. Although losses are relatively high, the acetone and DI water fluids were used to demonstrate the capability of shift in resonance. Table 14 shows that if a higher permittivity (relative to air) fluid is utilized and loss can be managed, the simulated radiation efficiency is reduced only slightly. The reduction in simulated radiation efficiency can likely be attributed to the physical antenna being smaller relative to the larger wavelength when fluid is present.

Table 13 Simulated radiation efficiency using fluids with finite loss in material property definition

Channel 1	Channel 2	First Resonance (GHz)	Radiation Efficiency (dB)	Second Resonance (GHz)	Radiation Efficiency (dB)
Air	Air	4.15	-0.40	7.88	-1.00
Air	Acetone	4.14	-0.44	6.77	-4.65
Air	DI Water	4.11	-0.74	5.44	-8.05
Acetone	Air	3.83	-1.18	7.83	0.78
DI Water	Air	3.41	-2.69	7.54	-2.53

Table 14 Simulated radiation efficiency using fluids without loss in material property definition

Channel 1	Channel 2	First Resonance (GHz)	Radiation Efficiency (dB)	Second Resonance (GHz)	Radiation Efficiency (dB)
Air	Air	4.15	-0.40	7.88	-1.00
Air	Acetone	4.14	-0.40	6.77	-1.79
Air	DI Water	4.11	-0.46	5.44	-2.27
Acetone	Air	3.83	-0.46	7.83	-0.92
DI Water	Air	3.41	-0.76	7.54	-1.22

Figure 46 shows the circuit simulated and the reference coordinate system. This same coordinate system is used when plotting the 3D polar plots.

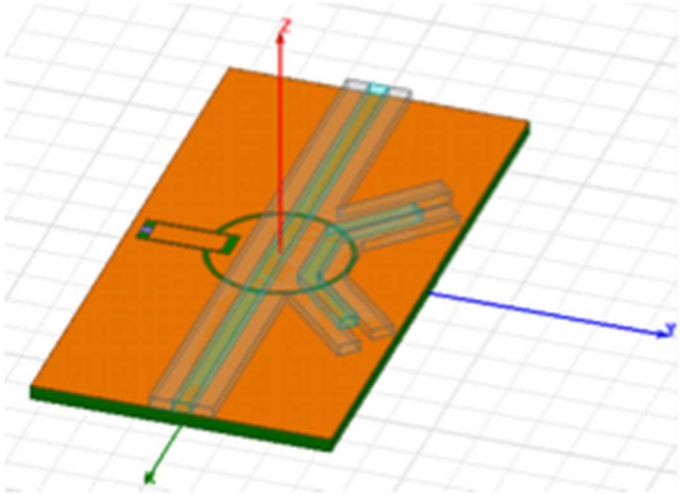

Figure 46 Simulated annular slot antenna with channel 1 +/- 45 degrees, channel 2 along y axis

Figure 47 is an example of the gain 3D polar plot at the first resonant frequency. The x- y- and z-axis are the same as shown in Figure 46. This general pattern is representative of the first mode for all instances of CH1 and CH2 with or without fluid. The peak gain is along the axis perpendicular to the board.

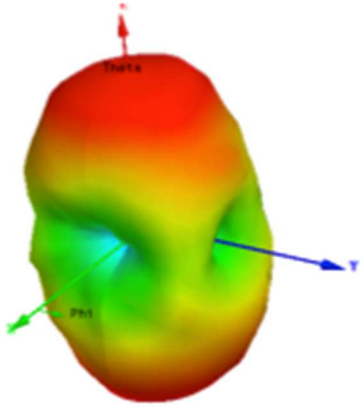

Figure 47 First resonance radiation pattern of annular slot. The x- y- and z-axis are the same as shown in Figure 46.

Figure 48 is an example of the gain 3D polar plot at the second resonant frequency when air is in CH1 and CH2.

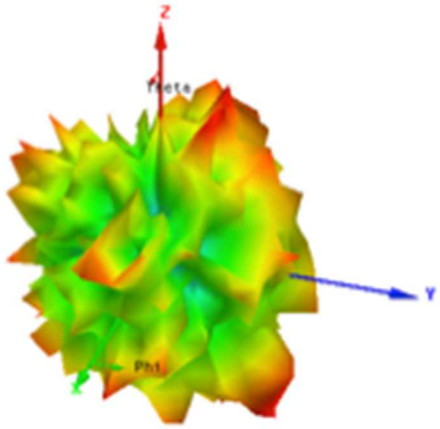

Figure 48 Second resonance radiation pattern of annular slot. The x- y- and z-axis are the same as shown in Figure 46.

The pattern changes when fluid is inserted into CH2 (Figure 49). The pattern starts to look more like the first resonance pattern (Figure 47) with peak gains approximately along the z-axis.

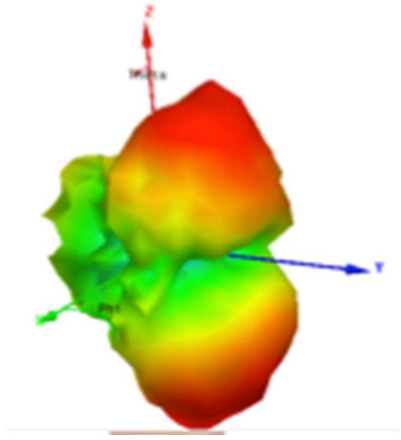

Figure 49 Second resonance radiation pattern of annular slot when CH2 filled with fluid. The x- y- and z-axis are the same as shown in Figure 46.

4.4 Fabrication Tolerances

Previous sections focused on circuit response based on the placement of fluidic channels in specific locations. This section details frequency shift sensitivity due to channel placement tolerance for both designs.

4.4.1 Design 1 Channel Placement Tolerance

Electric field distributions for the first and second modes are shown in Figure 24 and Figure 25, respectively. In design 1 (parallel channel configuration) tuning of the first and second mode is not decoupled. Dimensions W_{C1} and W_{C2} are varied independently through simulation to better understand their individual contributions to frequency shift. The left edge of channel W_{C1} is swept inward (0.05, 0.1, 0.5, and 1 mm) while the right edge is fixed in location (Figure 50). The right edge is fixed because it is far enough onto the ground plane to not impact the frequency response when varied. A summary of the frequency shift for the various channel widths (W_{C1}) are given in Table 15. Note that W_{C2} is fixed in width and is filled with air in this scenario.

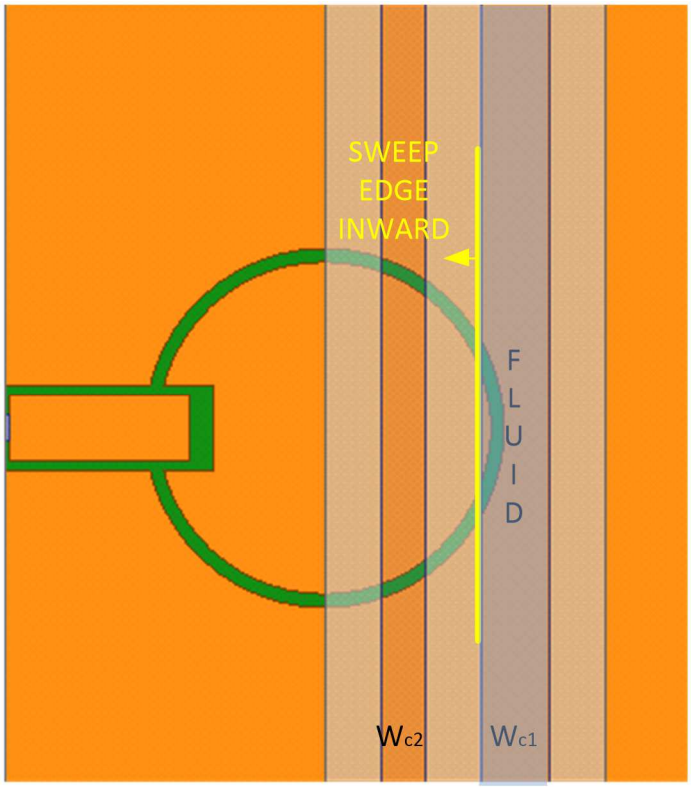

Figure 50 Sweep channel 1 (W_{c1}) inner edge toward feedline

Table 15 Frequency change from baseline design due to channel 1 (CH1) width increase. Acetone or DI water in channel 1 and air in channel 2.

	FIRST RESONANCE CHANGE (GHz)		SECOND RESONANCE CHANGE (GHz)	
W_C Increase (mm)	CH1 DI	CH1 ACETONE	CH1 DI	CH1 ACETONE
0.05	-0.03	-0.03	-0.03	-0.03
0.1	-0.04	-0.05	-0.09	-0.03
0.5	-0.12	-0.17	-0.6	-0.07
1	-0.14	-0.24	-1.32	-0.14

The frequency response sensitivity to channel 2 (W_{C2}) width was also investigated. The left and right edges of channel W_{C2} are swept by half the total channel width increase (0.05, 0.1, 0.5, and 1 mm). Channel 1 (W_{C1}) is fixed in width and filled with air. Channel 2 is filled with fluid (Figure 51). A summary of the frequency shift for the various channel widths (W_{C2}) are given in Table 16.

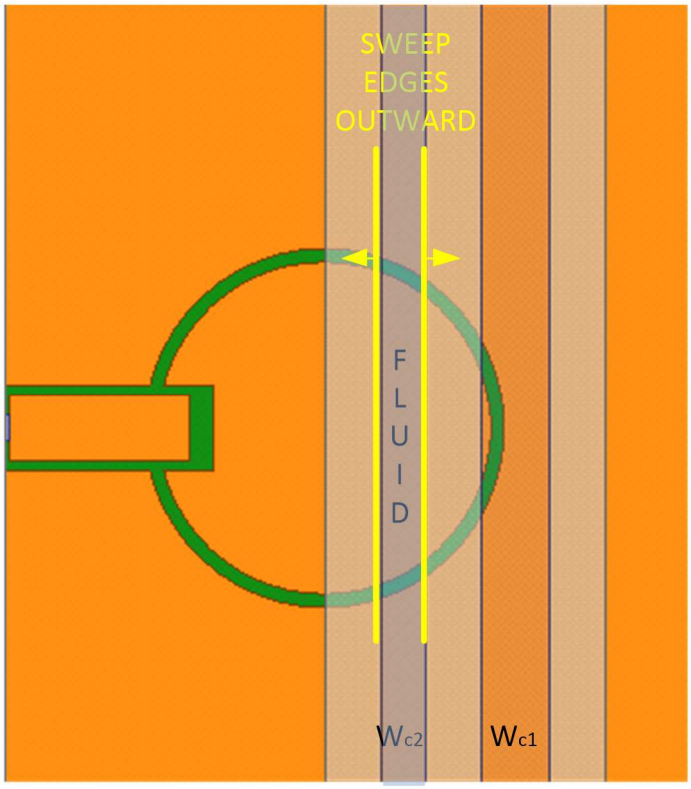

Figure 51 Sweep channel 2 (W_{c2}) wall edges outward

Table 16 Frequency change with respect to baseline design due to channel 2 width increase

	FIRST RESONANCE CHANGE (GHz)		SECOND RESONANCE CHANGE (GHz)	
W_C Increase (mm)	CH1 DI	CH1 ACETONE	CH1 DI	CH1 ACETONE
0.05	-0.03	-0.03	-0.03	-0.03
0.1	-0.04	-0.05	-0.09	-0.03
0.5	-0.12	-0.17	-0.6	-0.07
1	-0.14	-0.24	-1.32	-0.14

4.4.2 Design 2 Channel Placement Tolerance

Design 2 was discussed in Section 4.3. It has one channel along the center axis (x-axis) of the annular ring and one channel that routes +45 and -45 degrees from the y-axis (Figure 52). The electric field distributions for the first and second mode are shown

in Figure 39 and Figure 40, respectively. This section investigates channel tolerance impact on the frequency response of the structure. The channel widths of the two channels are varied independently to better understand their individual contribution.

The first channel width investigated is channel 1 (CH1). The channel width is increased symmetrically about its centerline by 0.05, 0.1, 0.5 and 1 mm. Thus the channel is expanded outward on each side by half that distance (Figure 52). The frequency shift with respect to the baseline design (Section 4.3) is summarized in Table 17. Note that channel 2 (CH2) is filled with air while channel 1 (CH1) is filled with fluid.

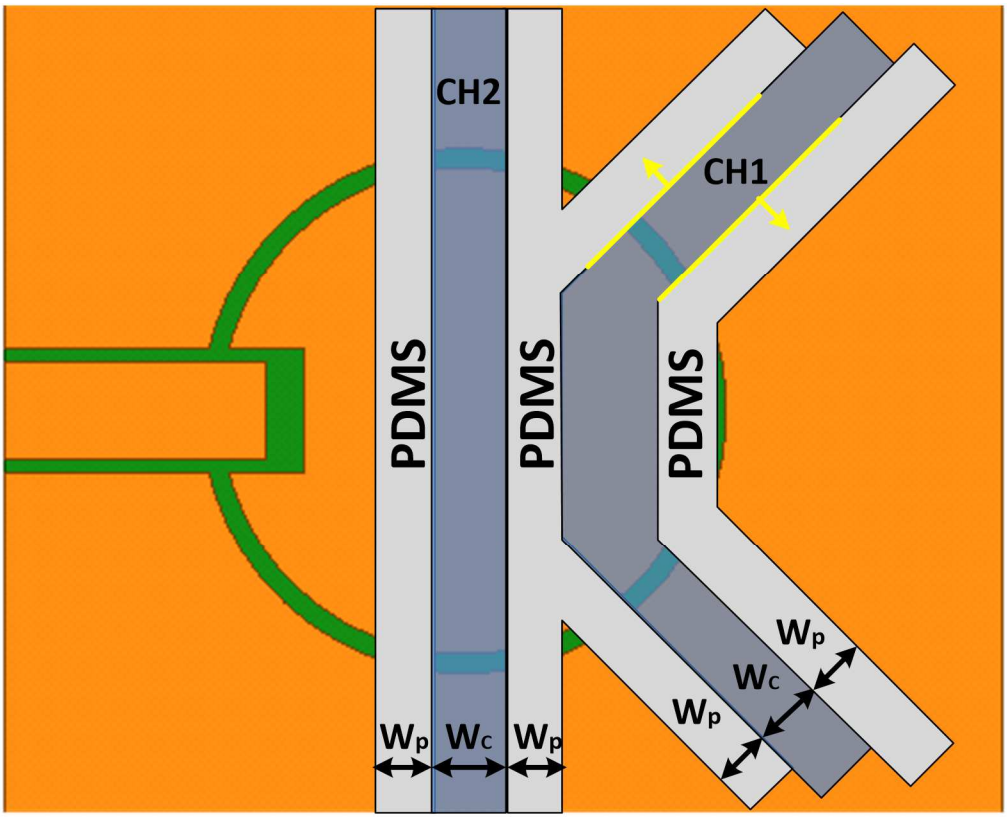

Figure 52 Annular slot antenna, channel 1 width tolerance

Table 17 Frequency change from baseline design due to channel 1 (CH1) width increase. Acetone or DI water in channel 1 and air in channel 2.

	FIRST RESONANCE CHANGE (GHz)		SECOND RESONANCE CHANGE (GHz)	
W_C Increase (mm)	CH1 DI	CH1 ACETONE	CH1 DI	CH1 ACETONE
0.05	0.00	0.00	-0.01	0
0.1	-0.01	0.00	-0.01	0
0.5	-0.05	-0.04	-0.13	-0.03
1	-0.10	-0.07	-0.27	-0.07

Next, channel 1 (CH1) is a fixed width (baseline width) and channel 2's width is varied. The width of channel 2 (CH2) is increased symmetrically about its centerline by 0.05, 0.1, 0.5 and 1 mm. Thus the channel is expanded outward on each side by half that distance (Figure 53). The frequency shift with respect to the baseline design (Section 4.3) is summarized in Table 18. Note that channel 1 (CH1) is filled with air and channel 2 (CH2) is filled with fluid.

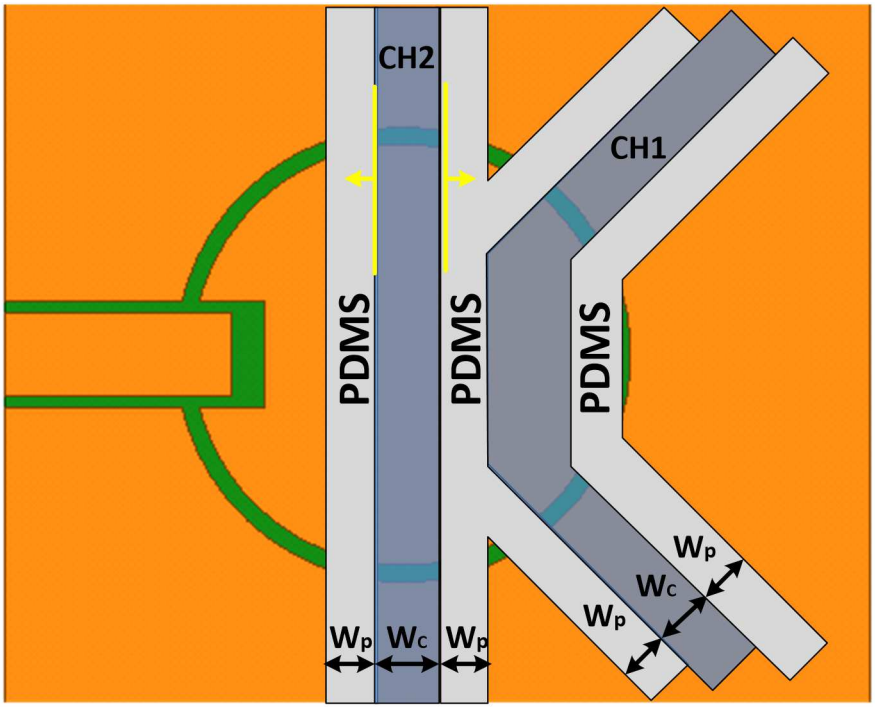

Figure 53 Annular slot antenna, channel 2 width tolerance

Table 18 Frequency change from baseline design due to channel 2 (CH2) width increase. Air in channel 1 and acetone or DI water in channel 2.

	FIRST RESONANCE CHANGE (GHz)		SECOND RESONANCE CHANGE (GHz)	
W_C Increase (mm)	CH2 DI	CH2 ACETONE	CH2 DI	CH2 ACETONE
0.05	0.01	0.00	-0.01	-0.01
0.1	0.01	-0.01	-0.03	-0.02
0.5	0.02	0.00	-0.1	-0.12
1	-0.01	-0.01	-0.17	-0.21

4.5 Conclusion

Integrating fluidic channels onto the surface of the antenna creates an annular slot antenna with variable capacitive load. Air, acetone, and DI water were used to show the frequency shift capabilities of the structure over a permittivity range (1, ~22, and ~81). Inserting fluid into channel 1 (W_{C1}) is shown to provide a tunable frequency range from 3.05 GHz to 4.2 GHz for the first resonance. Inserting fluid into both channel 1 (W_{C1}) and channel 2 (W_{C2}) is shown to provide a tunable frequency range from 4.47 GHz to 7.9 GHz for the second resonance. Frequencies in between these ranges can be realized using liquids in the range of ε_r=1 to ε_r=81.

Independent control of the first and second resonant frequencies using surface integrated fluidic channels on the annular slot antenna has been demonstrated. Careful investigation of the electric field distribution on the antenna is used to determine channel placement locations. A designer should compare the absolute field distributions for the modes of interest. If the desired modes each have some finite magnitude at that location being investigated then the modes will be coupled. However if one mode is at a null and

the other has some finite magnitude then the only the mode with the finite magnitude will be impacted. The greater the field magnitude the more the frequency will shift in the presence of fluid.

A tunable range of 0.9 GHz for the first resonance and 2.8 GHz for the second resonance was achieved. Measured and simulated radiation patterns are in close agreement. DI water loss causes degradation in the peak gain values. It was also shown that using a lower loss fluid will reduce this degradation. Thus, care must be taken to determine if the minimum achievable gain is acceptable based on the fluid performance when using fluids for tuning.

5 Fluid Controlled Degenerate Mode Microstrip Filter

Today wireless systems often require the use of narrowband high roll-off filters to improve receiver blocking and intermodulation distortion performance. Ring resonators can potentially be used in such an application because of their high Q response. However, wireless systems are also requiring frequency versatility to support multiple channel operation within a band and in some instances multiple band operation. Thus either banks of filters or a tunable filter is required to support these demands (Figure 1). Introducing a stub or perturbation along the plane of symmetry is known to excite a degenerate mode response changing the passband characteristics of a bandpass filter [33-44]. In [35, 36] it was shown that changing the length of this stub controls the separation of the even and odd modes. The odd mode is not impacted by the stub and the even mode shifts downward in frequency with increasing stub length [35].

Another critical design consideration is the method of coupling to the resonator. In [21], it is shown that gap coupling (without edge coupled elements) has the least impact on the ring response but also has the highest insertion loss. This insertion loss can be drastically reduced by adding edge coupled elements [40, 42].

Frequency tunability can also be accomplished with a ring resonator circuit by integrating varactors or PIN diodes at specific locations [21, 41, 43]. In [21, 43], the bandpass resonant frequency is adjusted by varying capacitance in the axis perpendicular to the feedlines. In [41], the capacitance is used to vary two stopbands.

The microstrip ring resonator detailed in this chapter has a stub whose electrical length is varied through the use of fluids. This design (Figure 54) uses a fluidic channel at the end of the stub to adjust the open-end capacitance. Simulation and measurement results for the channel filled either with air, acetone (ε_r=24, tanδ=0.05 @ 2GHz), or DI water (ε_r=77, tanδ=0.1 @ 2 GHz) are presented. A gap coupled feed architecture is used. A microstrip ring filter leveraging the degenerate mode created by a stub on the ring is presented. This work uses a fluidic channel filled either with air, acetone, or de-ionized (DI) water at the end of the stub to vary the operating frequency. A frequency shift from 2.21 GHz to 1.79 GHz is observed.

5.1 Development

The ring radius in the design is based on the guided wavelength. From [21], the unloaded ring modes are defined by Eq. 5.1.

$$2\pi r = n\lambda \tag{5.1}$$

where r is the mean radius, λ is the guided wavelength, and n (1, 2, 3..) is the mode order. The radius (R) in this design is chosen to be 10.04 mm (Figure 54). The trace width (W_R) of the ring is 2.96 mm.

The current distribution for the first mode of an unloaded ring has nulls located along the X-axis while the second mode has nulls located at +/-45 degrees from the +X-axis and –X-axis. By using a perpendicular feed configuration, the first resonance of the ring will be a stopband and the second resonance will be a passband [21].

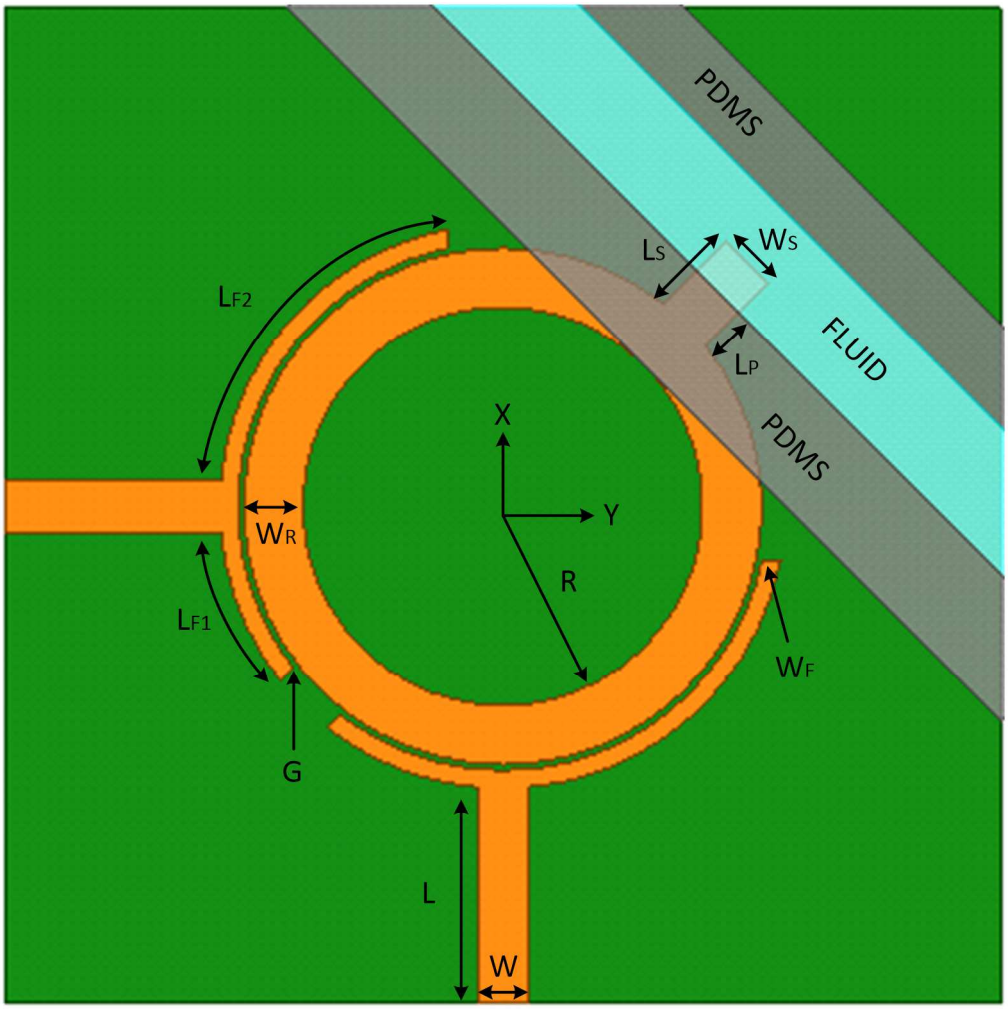

Figure 54 Microstrip ring filter with stub. Fluidic channel on stub.

The microstrip feed is designed to be 50 ohms on FR-4. The width (W) is 2.96 mm and the length (L) is 10.87 mm. As stated earlier, two important quantities controlling the insertion loss are (a) the length of the feedline section coupled to the ring (L_{F1} and L_{F2}) and (b) the gap (G) between the feedline and ring. These parameters are investigated using Ansoft HFSS. Figure 55 shows simulated results when L_{F1} and L_{F2}=0, L_{F1}=L_{F2}=7.7 mm, and L_{F1}=7.7 mm and L_{F2}=17.3 mm. Based on these results, L_{F1}=7.7 mm and L_{F2}=17.3 mm are chosen for the design due to the lower insertion loss.

Additionally, L_{F2} is stopped prior to the fluidic channel so that it will not be impacted directly by the fluid. The width (W_F) of L_{F1} and L_{F2} are 0.3 mm.

Gap (G) distances of 0.2 mm and 0.5 mm where simulated to understand fabrication tolerances. The dimension is kept small to improve insertion loss. The simulated insertion loss for G=0.2 mm is -2.21 dB and -2.85 dB for G=0.5 mm. A spacing of 0.2 mm was chosen for this design. The length of the stub (L_S) on the ring is 4.5 mm and width (W_S) is 2.96 mm.

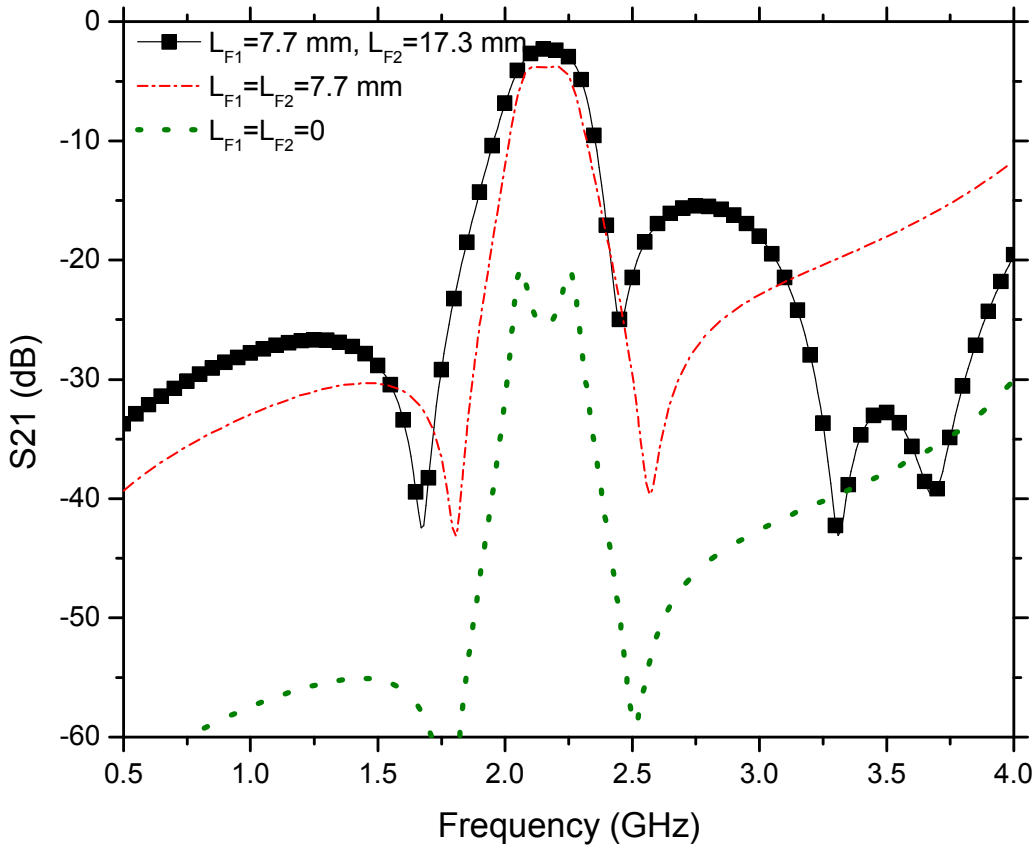

Figure 55 Feedline coupling impact on insertion loss

An optimetric simulation using Ansoft HFSS was run sweeping permittivity in the channel from 1 to 81 in increments of 10 (lossless materials). The simulated s-parameter results are shown in Figure 56-58. The bandwidth of the passband is increased with the higher dielectric fluid (Figure 56). However, this extra bandwidth is traded off for increased passband ripple (Figure 57). Additionally, as the two passband peaks separate further apart, so do the regions of acceptable return loss (Figure 58). Acetone (ε_r=24, tanδ=0.05 at 2 GHz) and DI water (ε_r=77, tanδ=0.1 at 2 GHz) will be used for proof-of-concept since they will provide mid- and high permittivity values.

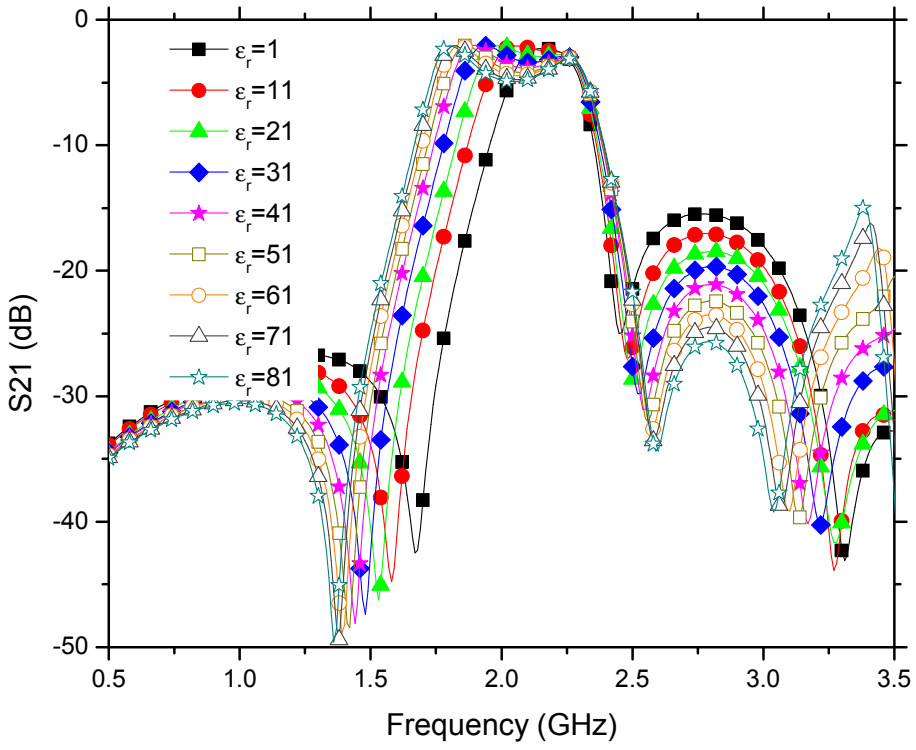

Figure 56 Wide-band insertion loss of filter, varying fluid in channel from ε_r=1 to ε_r=81 in increments of 10

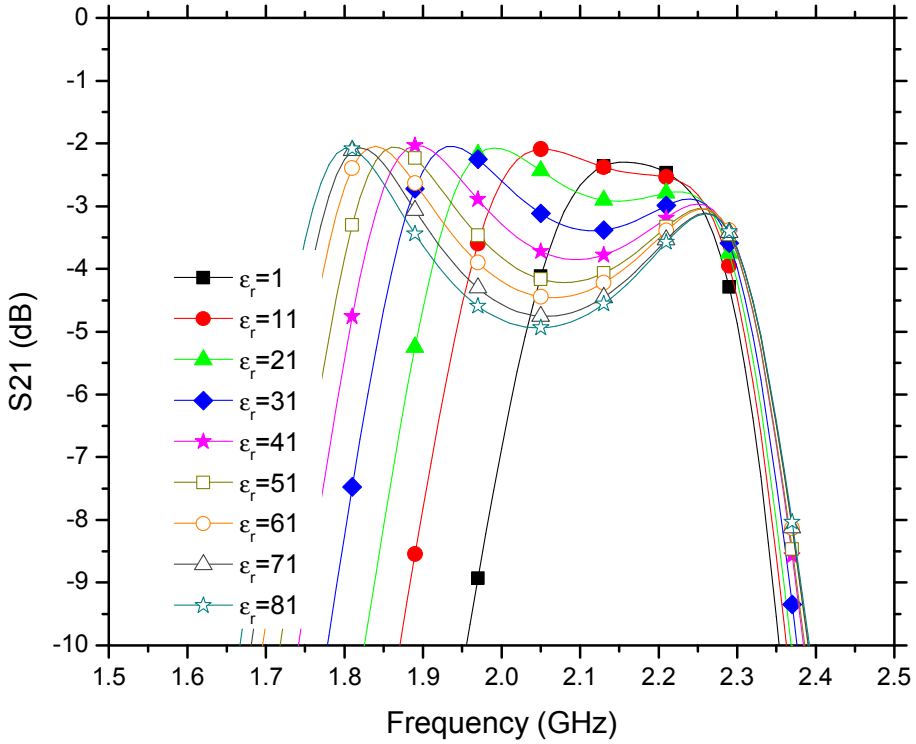

Figure 57 Narrow-band view of insertion loss of filter, varying fluid in channel from ε_r=1 to ε_r=81 in increments of 10

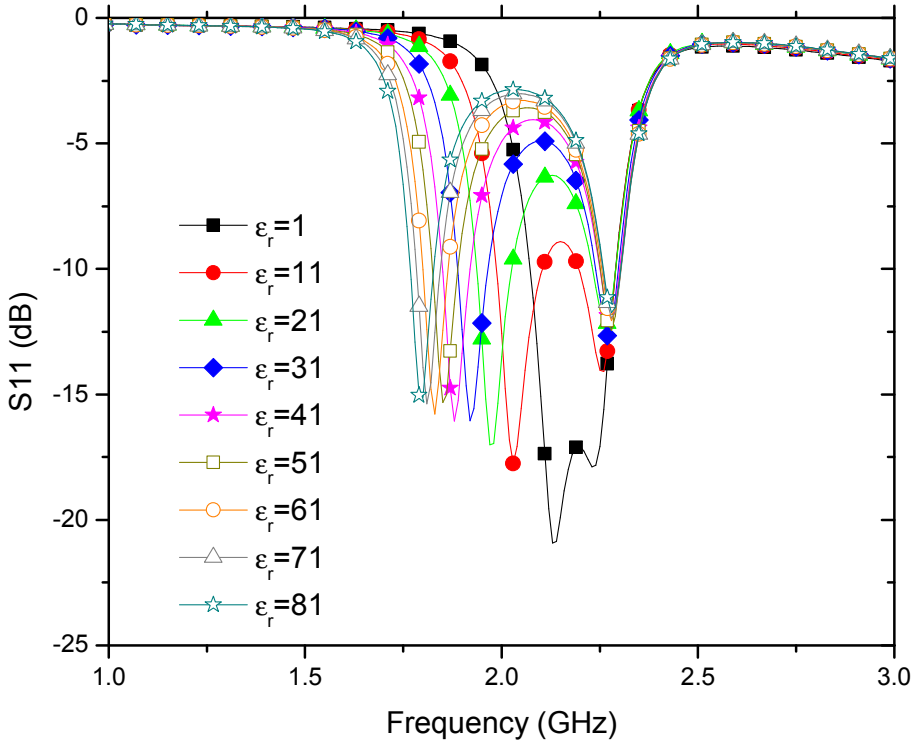

Figure 58 Return loss of filter, varying fluid in channel from εr=1 to εr=81 in increments of 10

5.2 Fabrication

The test structure was fabricated on 1.52 mm FR-4 (ε_r=4.4, tanδ=0.02) substrate using an LPKF milling machine (Figure 59). The dimensions of the fabricated structure are outlined in Section 5.1. The overall board dimensions are 50 mm by 50 mm. A polydimethylsiloxane (PDMS) housing is attached to the substrate surface using PDMS adhesive creating a fluidic housing. The fluidic channel is parallel to the width of the stub as shown in Figure 59. The PDMS is attached starting at the inner edge of the ring and extends onto the stub 2.4 mm (L_P). The remainder of the stub is exposed to fluid.

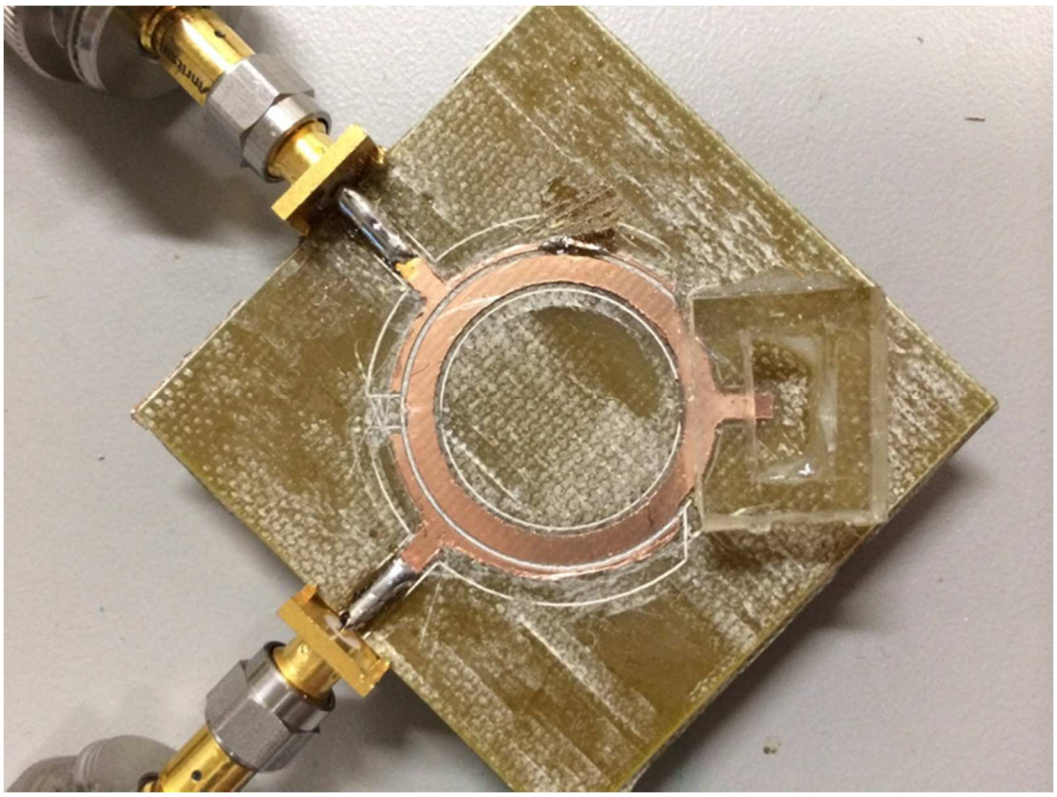

Figure 59 Fabricated ring filter with PDMS housing

5.3 Characterization

S-parameters were measured using an Anritsu network analyzer. Figure 60 shows measured and simulated insertion loss when the fluidic housing is filled either with air, acetone, or DI water. The minimum insertion loss with the various fluids are (a) -2.28 dB for air, (b) -2.96 dB for acetone, and (c) –4.44 dB DI water. The insertion loss increases from air to DI water due to the increased loss tangent of DI water. Figure 61 shows simulated insertion loss results with lossless fluids with the same permittivity values as acetone and DI water. The insertion loss varies less than 0.2 dB between the curves. The frequency shift observed is similar to the measured results. The measured center

frequency when the channel is filled with air is 2.21 GHz. When the fluid is introduced into the channel the modes split. The odd mode does not shift much while the even modes shift to 1.98 GHz when acetone is in the housing and 1.79 GHz when DI water is in the housing.

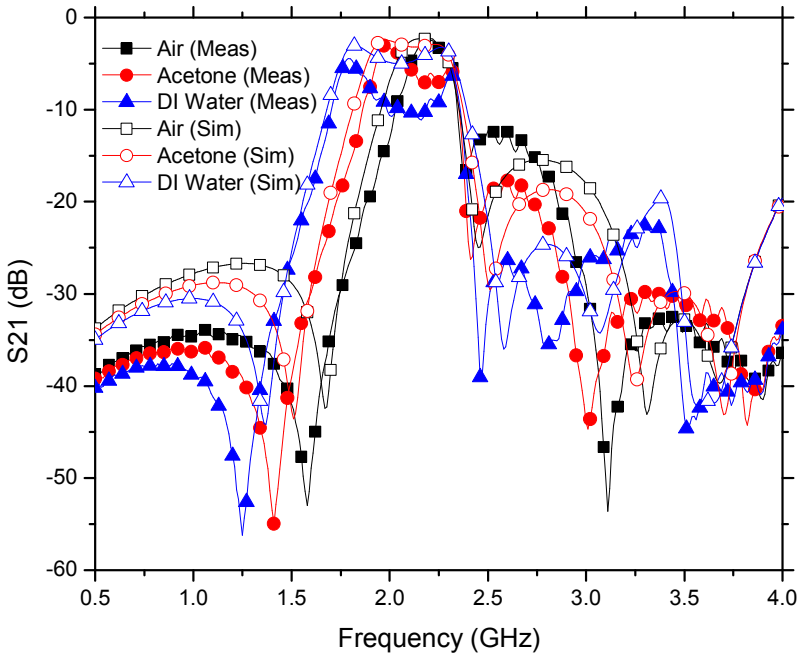

Figure 60 Insertion loss simulation and measurement results for the fluidic housing filled either with air, acetone, or DI water.

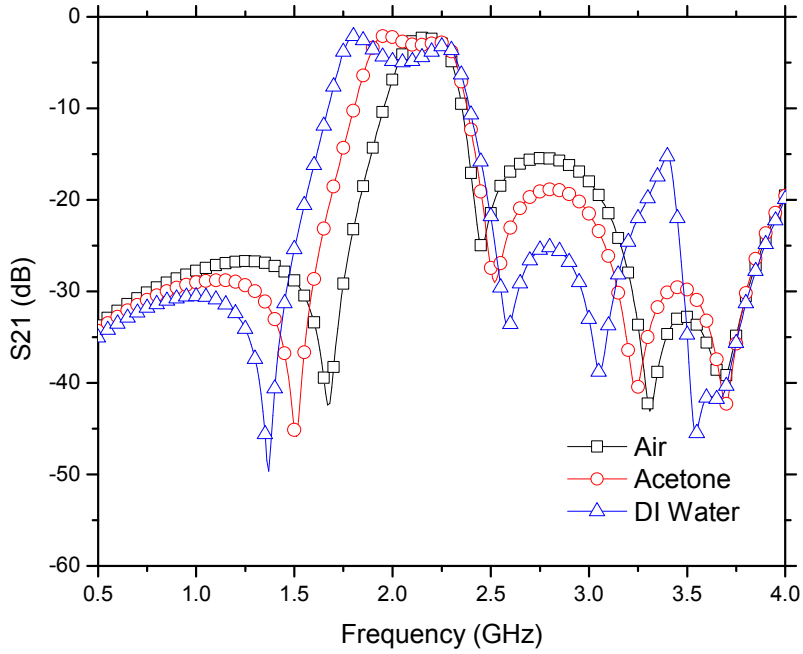

Figure 61 Simulated insertion loss results of lossless fluids. Only permittivity of fluid is used.

Figure 62 shows the return loss when the fluidic housing is filled either with air, acetone, or DI water. The instance when air is in the channel the 10 dB bandwidth is 70 MHz over the single frequency band. Introducing acetone or DI water into the channel causes the even and odd modes to split more than in the air instance. The first frequency band is the same as the air instance and second band is lower in frequency due to the extra capacitance. The measured return loss is degraded from the lossless scenario (Figure 63) and the air instance.

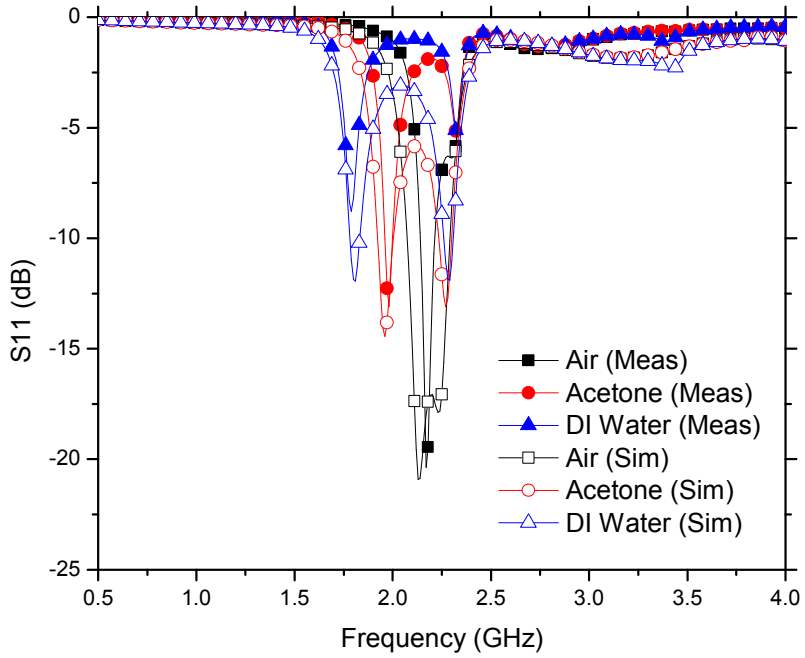

Figure 62 Return loss simulation and measurement results for the fluidic housing filled either with air, acetone, or DI water.

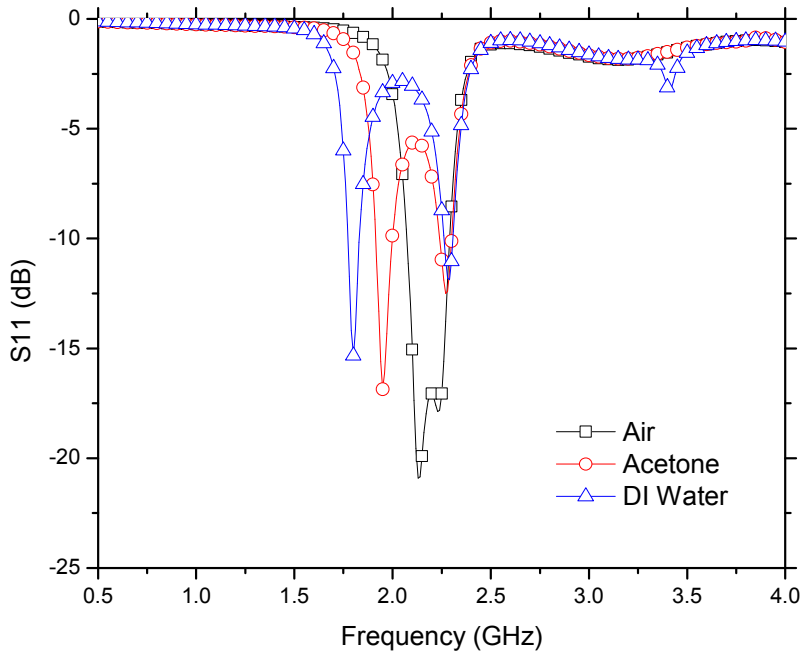

Figure 63 **Simulated return loss results for lossless fluids. Only permittivity of fluid is used.**

5.4 Fabrication Tolerances

Standard fabrication facilities can easily achieve a 0.1524 mm line width with up to 0.0305 mm tolerance (20%). As stated in Section 5.1, a gap spacing of 0.2 mm and 0.5 mm were simulated resulting in 0.64 dB of change in insertion loss. This is a delta of 0.3 mm (11.8 mil) in line width, well within the capabilities of fabrication houses.

In addition to the feed, the other critical area of design for this structure is the stub. The stub is 4.5 mm long (177 mils), thus etch tolerances could only change the stub length by 0.6%. Obviously if the concepts of this structure were applied to a higher frequency design then these tolerances would become more critical.

The next design element a designer would need to understand is the sensitivity of fluidic channel placement on the S-parameter response. The fluidic channel width impact on S-parameter was simulated (vary L_P).

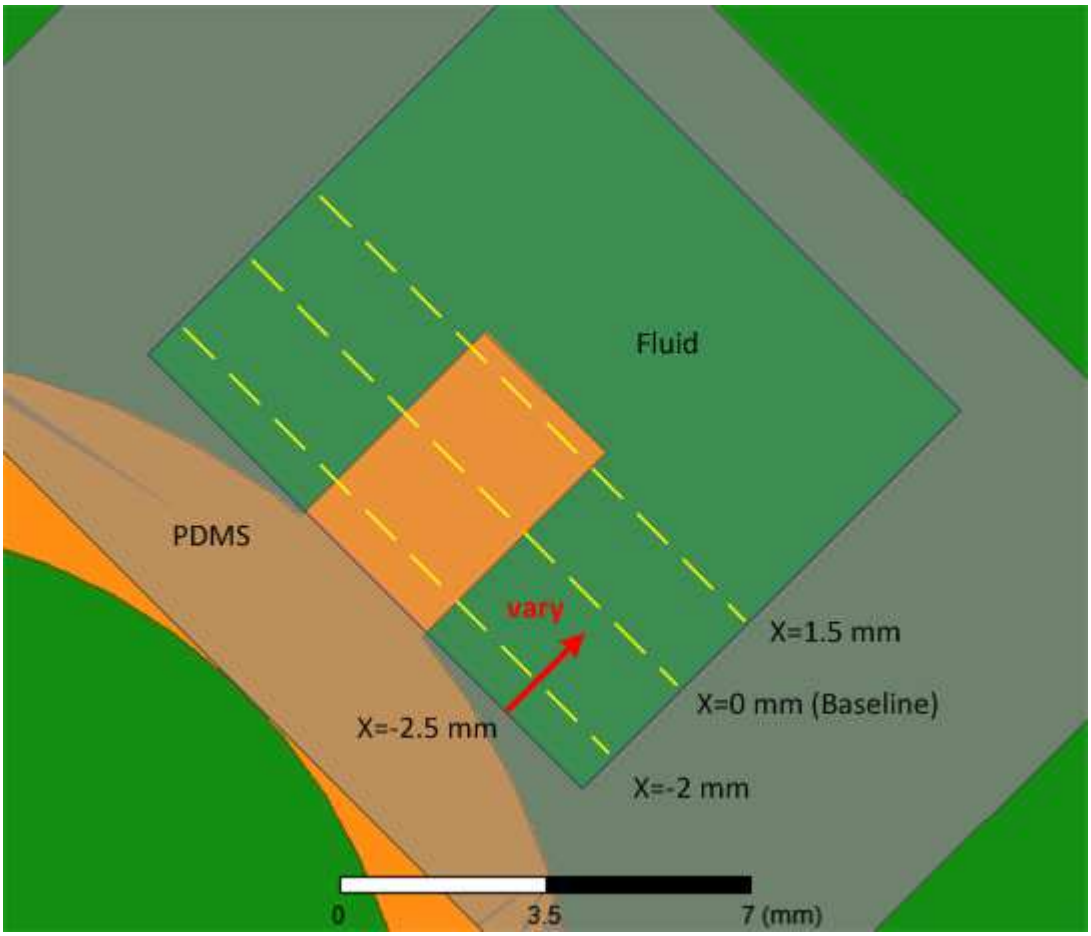

Figure 64 Fluidic channel placement on stub tolerance

Results are shown in Figure 65 for fluids DI water and acetone.

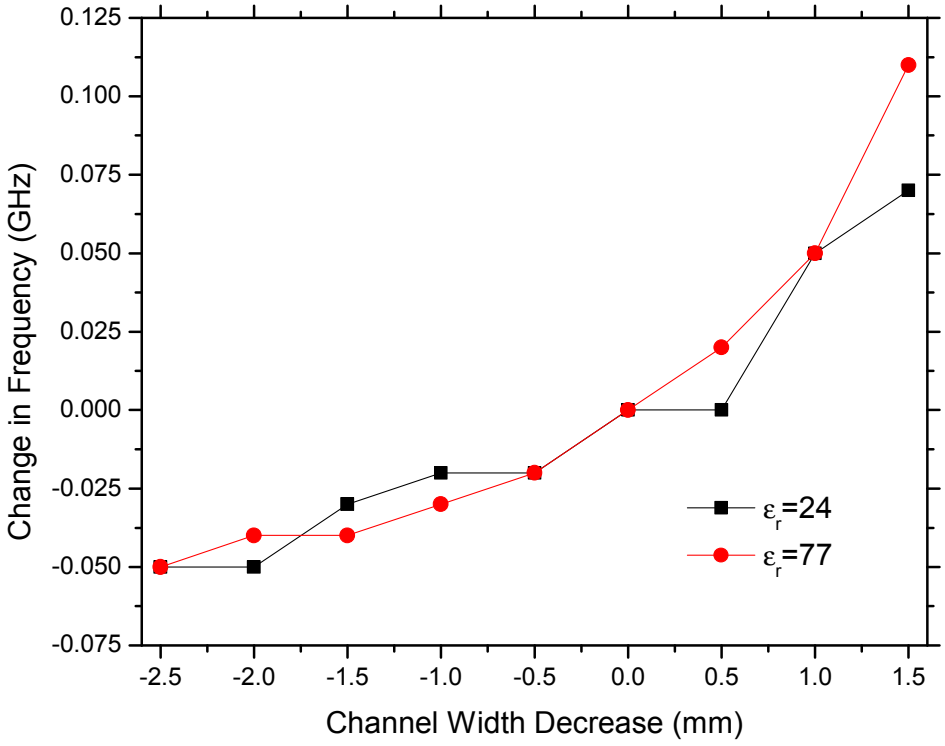

Figure 65 Channel width impact on fundamental frequency. Channel is filled with acetone or DI water.

5.5 Conclusion

A gap coupled microstrip ring filter with -2.28 dB of insertion loss is presented. Introducing acetone caused the even and odd modes to split more than when air was in the channel creating a second passband 0.23 GHz below the air instance. An additional 0.68 dB of insertion loss was measured when acetone was used.

When DI water is placed in the channel the second passband is 0.42 GHz below the air instance. However, DI water is a lossy fluid and degraded insertion loss (2.16 dB) is traded for the frequency shift.

Simulation results in Section 5.4 show that if a lower loss high permittivity fluid is used, the tradeoff of insertion loss for frequency shift can be minimized.

6 Conclusion and Future Work

In this work many of the RF front-end components shown in Figure 66 (repeat of Figure 1 from the introduction) were designed with fluid channels integrated. The integration of fluids provides frequency versatility and the potential to reduce component count. Integration of fluids into the system does increase fabrication complexity; however knowledge surrounding the physics and reducing fabrication cost/complexity has been greatly increased over recent years by the many research groups in the microfluidics community.

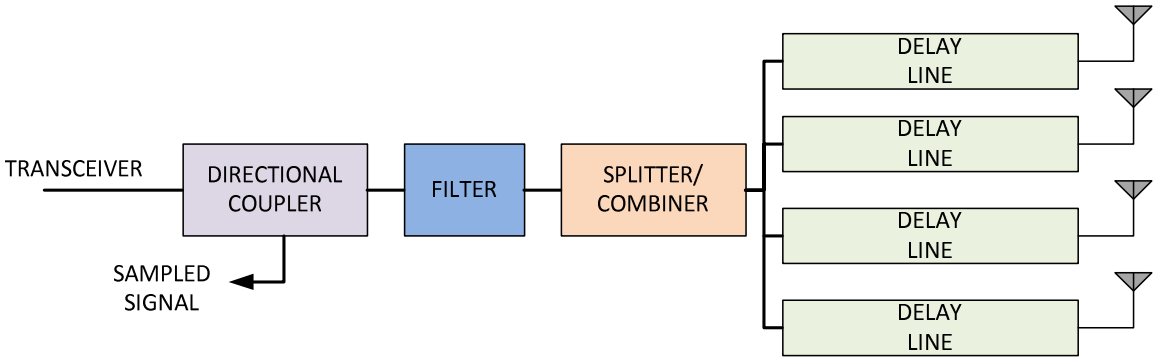

Figure 66 Example RF front-end. A directional coupler, filter, delay line, and antenna design are covered in this dissertation.

A multi-section CPW line with a fluidic channel integrated in the middle section creating a delay line is demonstrated in Section 2. The structure is used to investigate the realizable phase shift using fluids with different fluidic housing dimensions. The high permittivity fluid, DI water, exhibits a large phase shift of approximately 9.4 degrees/mm. However, transmission power is compromised due to high loss tangent of DI water. Using smaller fluidic housing dimensions can decrease insertion loss but reduces the tunable range of phase.

Next, a microstrip forward wave directional coupler with a fluidic channel is demonstrated in Section 3. The fluidic channel is attached onto the surface of the substrate in the gap between the coupled lines. Two channel architectures used to house fluids were described: 1) with a thin layer of PDMS in the channel floor and 2) a structure without the layer of PDMS in the channel floor. Simulation and measured results showed that by inserting a thin layer of PDMS into the channel floor, some coupling range was sacrificed but greatly improved insertion loss by limiting the amount high loss fluid the odd mode interacted with. Additionally, by including PDMS in the channel floor a better matched system over a wider range of fluid permittivity values was realized. The inclusion of the dielectric fluids did equalize the even and odd mode propagation constants some, resulting in improved directivity of the directional coupler.

Section 4 described the use of fluids in tuning annular slot antennas. Two different fluidic channel structures were described. The first structure had two parallel channels perpendicular to the feedline on the opposite half of the ring. It was shown that tuning of the first and second modes were coupled with this fluidic channel configuration. The second channel configuration took into account the electric field distributions of an annular slot and placed the channels to decouple the tuning of the modes. Both designs radiation characteristics were impacted by the high loss tangent of DI water. A lower loss fluid would be required to provide significant value to this type of design.

Lastly, in Section 5 a degenerate mode bandpass microstrip ring filter is described. The electrical length of a stub on the annular ring along the axis of the symmetry is varied using fluids. With air in the fluidic channel the filter has -2.28 dB of

insertion loss. Introducing acetone caused the even and odd modes to split more than when air was in the channel creating a second passband 0.23 GHz below the air instance. An additional 0.68 dB of insertion loss was measured when acetone was used. When DI water is placed in the channel the second passband is 0.42 GHz below the air instance. However, DI water is a lossy fluid and degraded insertion loss (2.16 dB) is traded for the frequency shift.

In all of these sections there was discussion regarding impact of the fluidic channel size tolerance on performance.

6.1 Future Work

As stated throughout this dissertation these design would benefit from a lower loss high permittivity fluid. Some research groups are starting to use high permittivity dielectric particles in a host fluid [45]. In addition to fluids with dielectric particles, fluids using magnetic particles could be analyzed to determine how circuit characteristics change.

Section 2 demonstrated the amount of phase delay realizable in a CPW structure when integrating fluids with permittivity values in the range between air and DI water. Next steps for this work would include creating a feeding network for a phased array antenna system which incorporates fluidic channels in this manner. Beam steering could then be characterized with respect to the fluid (specific ε_r values using particles) and compared to conventional methods.

Section 3 demonstrated a microstrip directional coupler with the ability to change the amount of coupling depending on the dielectric permittivity in the gap between the

coupled traces. Future work could focus on creating low loss fluids with known permittivity followed by characterization of the structure using these fluids. For example, time it takes to switch between fluids and measured coupling.

Section 4 demonstrated the ability to tune the operating frequency of an annular slot antenna. Future work for this architecture would be to compare the power handling capability of this structure to the power handling capability of other tuning mechanisms such as varactor diodes. Additionally, improvements to measured radiation efficiency through the use of lower loss fluids (e.g. realized through dielectric particles) could be investigated.

Section 5 focused on a degenerate mode microstrip ring filter demonstrating the capability to split the passband into two frequency bands using fluidic loading. Future work would be to apply this to specific bands such as 900 MHz and 2.4 GHz and characterize the switching time.

This worked focused on understanding the range of change realizable in critical characteristics for each structure. This work could be taken be looked at for sensor applications to better understand what the fluid properties are for the fluid present in the structure. In addition to sensor applications, high power applications could be investigated to determine if there is benefit to using fluids in RF circuits.

7 References

[1] Dau-Chyrh Chang; Bing-Hao Zeng; Ji-Chyun Liu, "Mechanical adjustable phase shifters for WiMAX BTS antenna," Microwave Conference, 2008. APMC 2008. Asia-Pacific , vol., no., pp.1,4, 16-20 Dec. 2008. doi: 10.1109/APMC.2008.4958099

[2] L. Le Cloirec, A. Benlarbi-Delai B. Bocquet, " New concept of RF functions by microfluidic coupling," Microwave and Optical Technology Letters, vol. 48, n 10, pp. 1912-16, Oct. 2006.

[3] H. Tang, R. Donnan, C. Parini, "Phase shifting with coplanar transmission line integrated electrostatic peristaltic micropumps," Radar Conference, 2005. EURAD 2005. European, pp. 315-318, 6-7 Oct. 2005.

[4] Tang, Hongyan; Donnan, R.; Parini, C., "Analogue Phase Shifter based on Stacked CBCPW," Microwave Conference, 2006. 36th European , vol., no., pp.761,763, 10-15 Sept. 2006. doi: 10.1109/EUMC.2006.281013

[5] C. Murray, R.R. Franklin, "Design and characterization of microfluidic housing effects on coplanar waveguide microfluidic delay line performance," Microwave and Optical Technology Letters, vol. 55, no. 4, pp. 789-793, Feb. 2013. Doi: 10.1002/mop.27434

[6] Ansoft Q3D Extractor V10.0.2, Canonsburg, PA

[7] Borofloat33 – Full specification (Borofloat33 datasheet, received via personal communication, Francis Zhang- Rep. for Plan Optik, April 27, 2009)

[8] F. Tay, C. Iliescu, J. Jing, J. Miao, "Defect-free wet etching through Pyrex glass using Cr/Au mask," Microsystem Technologies, vol. 12, n 10-11, pp. 935-9, 2006.

[9] Ansoft HFSS V13.0.2, Canonsburg, PA

[10] S. Seo, T. Stintzing, I. Block, D. Pavlidis, M. Rieke, P.G. Layer, "High frequency wideband permittivity measurements of biological substances using coplanar waveguides and application to cell suspensions," Microwave Symposium Digest, 2008 IEEE MTT-S International, pp. 915-918, 15-20 June 2008.

[11] S.L. March, "Phase Velocity Compensation in Parallel-Coupled Microstrip," Microwave Symposium Digest, 1982 IEEE MTT-S International, pp. 410-412, June 1982. doi: 10.1109/MWSYM.1982.1130739

[12] M. Dydyk, "Microstrip directional couplers with ideal performance via single-element compensation," IEEE Transactions on Microwave Theory and Techniques, vol. 47, no. 6, pp. 956-964, June 1999. doi: 10.1109/22.769332

[13] C. Kim, Y. Kim, S. Song, W. Jung, K. Kang, J. Park, and D. Ahn, "A design of microstrip directional coupler for high directivity and tight coupling", Proceedings of 31st European Microwave Conference, (2001), 201-204.

[14] A. Podell, "A High Directivity Microstrip Coupler Technique," Microwave Symposium, G-MTT 1970 International, pp. 33-36, May 1970. doi: 10.1109/GMTT.1970.1122761

[15] Z. Wang, M. Zheng, Y. Fu, F. Xiao, "A Design of 3-dB Wiggly Line Coupler Using Micromachining Technology and Compared with 3-dB Lange Coupler," 2007 IEEE International Workshop on Anti-counterfeiting Security Identification, pp. 48-51, April 2007. doi: 10.1109/IWASID.2007.373693

[16] J. Chen, S. Chang, Y. Jeng, C. Lin, "Wiggly technique for broadband non-uniform line couplers," Electronics Letters, vol. 39, no. 20, pp. 1451-1453, 2003. doi: 10.1049/el:20030957

[17] R.K. Mongia, I.J. Bahl, P. Bhartia, J. Hong, *RF and Microwave Coupled-Line Circuits*, Norwood, MA: Artech House Inc., 2007.

[18] C. Murray, R.R. Franklin, "EDGE coupled variable microfluidic directional coupler," Microwave and Optical Technology Letters, vol. 55, no. 4, pp. 756-758, Feb. 2013, doi: 10.1002/mop.27436

[19] S. Niyogi, J. Scott, K. Ghorbani, "Variable directional coupler employing microfluidics", 2008 38th European Microwave Conference, (2008), 207-210.

[20] U. Schwarz, M. Helbig, J. Sachs, F. Seifert, R. Stephan, F. Thiel, and M.A. Hein, "Physically small and adjustable double-ridged horn antenna for biomedical UWB radar applications", 2008 IEEE International Conference on Ultra-Wideband, Hannover, Germany, (2008), 5-8.

[21] K. Chang and L. Hsieh, Microwave Ring Circuits and Related Structures. Hoboken, NJ: John Wiley & Sons, 2004

[22] C.S. Hong, “Small annular slot antenna with capacitor loading,” in Electronic Letters, vol. 36, no. 2, pp. 110–111, January 2000.

[23] C. White and G. Rebiez, “Single- and Dual-Polarized Tunable Slot-Ring Antennas,” IEEE Trans. Antennas and Propagat., vol. 57, no. 1, pp. 19-26, January 2009.

[24] I. Carrasquillo-Rivera, R.A.R Solis, J.G. Colom-Ustariz, "Tunable and dual-band rectangular slot-ring antenna," *Antennas and Propagation Society International Symposium, 2004. IEEE* , vol.4, no., pp. 4308- 4311 Vol.4, 20-25 June 2004

[25] S. Nikolaou, R. Bairavasubramanian, C. Lugo Jr., I. Carrasquillo, D.C. Thompson, G.E. Ponchak, J. Papapolymerou, M.M. Tentzeris, "Pattern and frequency reconfigurable annular slot antenna using PIN diodes," *Antennas and Propagation, IEEE Transactions on* , vol.54, no.2, pp. 439- 448, Feb. 2006

[26] C.R. White, G.M. Rebeiz, "A slot-ring antenna with an octave of tunability," *Antennas and Propagation Society International Symposium, 2007 IEEE* , vol., no., pp.5841-5844, 9-15 June 2007

[27] N. Behdad and K. Sarabandi, "A varactor-tuned dual-band slot antenna," IEEE Trans. Antenna and Propagat, vol.54, no.2, pp. 401-408, February 2006.

[28] A. King, J. Patrick, N. Sottos, S. White, G. Huff, and J. Bernhard, “ Microfluidically Switched Frequency-Reconfigurable Slot Antennas,” IEEE Antennas and Wireless Propagation Letters, vol. 12, pp. 828-831, 2013.

[29] D. Rodrigo, L. Jofre, and B. Cetiner, “Circular Beam-Steering Reconfigurable Antenna with Liquid Metal Parasitics,” IEEE Trans. Antennas and Propagat., vol. 60, no. 4, pp. 1796-1802, April 2012.

[30] D. Peroulis, K. Sarabandi, L. Katehi, "Design of reconfigurable slot antennas," Antennas and Propagation, IEEE Transactions on , vol.53, no.2, pp.645-654, Feb. 2005

[31] C. Murray and R.R. Franklin, “Frequency Tunable Annular Slot Antenna,” in IEEE Int. Symp. on Antennas and Propag., Orlando, FL, July 2013. pp. 386-387

[32] C. Balanis, “Antenna Measurements,” in Antenna Theory, 3rd ed., New Jersey: Wiley, 2005, pp.1033-1034

[33] I. Wolff, "Microstrip bandpass filter using degenerate modes of a microstrip ring resonator," Electronics Letters, vol. 8, no. 12, June 1972, pp. 302-303, doi: 10.1049/el:19720223.

[34] K. Chang and L. Hsieh, Microwave Ring Circuits and Related Structures. Hoboken, NJ: John Wiley & Sons, Inc., 2004.

[35] B. Lacroix, J. Papapolymerou, "A triple-mode X-band microstrip ring resonator filter," Microwave Symposium Digest (MTT), 2011 IEEE MTT-S International, June 2011, pp. 1-4, doi: 10.1109/MWSYM.2011.5972892.

[36] M. Matsuo, H. Yabuki, M. Sagawa, M. Makimoto, "Analysis of resonant characteristics for a one-wavelength ring resonator coupled with two orthogonal resonant modes," Electronics & communications in Japan, vol. 82, issue 9, 1999, pp. 19-28.

[37] M. Matsuo, H. Yabuki, M. Makimoto, "Dual-mode stepped-impedance ring resonator for bandpass filter applications," IEEE Transactions on Microwave Theory and Techniques, vol. 49, no. 7, July 2001, pp. 1235-1240, doi: 10.1109/22.932241.

[38] L.H. Hsieh and K. Chang, "Simple analysis of the frequency modes for microstrip ring resonators of any general shape and correction of an error in the literature." Microwave and optical technology letters, vol. 38, 2003, pp. 209-213.

[39] A.C. Kundu and I. Awai, "Control of attenuation pole frequency of a dual-mode microstrip ring resonator bandpass filter," IEEE Transactions on Microwave Theory and Techniques, vol. 49, no. 6, June 2001, pp. 1113-1117, doi: 10.1109/22.925499.

[40] P. Gardner, D.K. Paul, K.P. Tan, "Planar microstrip ring resonator filters," IEE Colloquium on Microwave Filters and Antennas for Personal Communication Systems, Feb. 1994, pp. 6/1-6/6.

[41] S. Luo and L. Zhu, "A Novel Dual-Mode Dual-Band Bandpass Filter Based on a Single Ring Resonator," IEEE Microwave and Wireless Components Letters, vol. 19, no. 8, Aug. 2009, pp. 497-499, doi: 10.1109/LMWC.2009.2024826

[42] H. Ishida, K. Araki, "A design of tunable UWB filters," International Workshop on Ultra Wideband Systems. Joint with Conference on Ultrawideband Systems and Technologies. pp. 424-428, May 2004.

[43] L.H. Hsieh and K. Chang, "Dual-mode quasi-elliptic-function bandpass filters using ring resonators with enhanced-coupling tuning stubs," IEEE Transactions

on Microwave Theory and Techniques, vol. 50, no. 5, May 2002, pp. 1340-1345, doi: 10.1109/22.999148.

[44] P. Gardner, D.K. Paul, K.P. Tan, "Planar microstrip ring resonator filters," IEE Colloquium on Microwave Filters and Antennas for Personal Communication Systems, Feb. 1994, pp. 6/1-6/6.

[45] G.H. Huff, S. Goldberger,"A Coaxial Stub Microfluidic Impedance Transformer (COSMIX)," IEEE Microwave and Wireless Components Letters, vol. 20, no. 3, pp. 154-156, March 2010. doi: 10.1109/LMWC.2010.2040217